# THE UNIVERSITY
## *of* ADELAIDE

# Synthesis of Advanced Electrocatalysts via the Ampoule Method for Water Electrolysis

## By Yongqiang Zhao

School of Chemical Engineering and Advanced Materials

Faculty of Engineering, Computer and Mathematical Science

A thesis submitted for the degree of Doctor of Philosophy

The University of Adelaide

July 2019

# Table of Contents

# Abstract

The commercial development of highly-efficient and low-cost bifunctional electrocatalysts for overall water electrolysis devices requires a simple synthesis method for controllable electrocatalyst preparation. However, common synthesis methods suffer from tedious process requirements and uncontrolled synthesis. Consequently, the development of efficient bifunctional electrocatalysts using simple and controlled techniques is particularly desirable for this field. To this end, the objectives of this thesis are to develop a simple strategy for the controllable synthesis of highly-efficient and low-cost bifunctional electrocatalysts and to investigate their electrocatalytic mechanisms.

The first aspect of this thesis focuses on charge state manipulation in cobalt selenide catalysts for overall water electrolysis coupled with a synchrotron-based study of the electrocatalytic mechanism. Three-dimensional cobalt selenide electrodes with CoSe and $Co_9Se_8$ phases are synthesized by a one-step calcination of Co foil with Se powder in a vacuum-sealed ampoule. The charge state of Co species and the electrocatalytic performance of the prepared catalysts are manipulated by controlling the Co to Se mass ratio. The mechanism study shows that for the as-prepared cobalt selenide electrocatalysts, a high Co charge state favors oxygen evolution reaction (OER) activity while a low Co charge state promotes hydrogen evolution reaction (HER) activity. The resultant materials can act as free-standing bifunctional electrocatalytic electrodes for the OER and HER in alkaline media. Moreover, a $10.3 \ \mathrm{mA \ cm^{-2}}$ current density at 1.8 V is achieved for overall seawater electrolysis by exploiting the as-synthesized cobalt selenide electrodes as both anode and cathode. This performance is three times higher than that for a noble-metal-based seawater electrolyzer benchmark at the same voltage ($2.9 \ \mathrm{mA \ cm^{-2}}$).

The second part of this thesis is to develop interfacial nickel nitride/sulfide as a bifunctional electrode to promote dissociative adsorption of water molecules for highly efficient overall water electrolysis. A nickel nitride/sulfide electrode (NiNS), whereby $Ni_3N$ and $Ni_3S_2$ species are interfaced, is synthesized via a one-step calcination process

of Ni foam with thiourea in a vacuum-sealed ampoule. The resultant NiNS can be employed directly as a bifunctional electrocatalyst for water splitting with excellent activity toward the HER and OER. The significant electrocatalytic performance of NiNS is attributed to the interface between $Ni_3N$ and $Ni_3S_2$, which functions as the electrochemical active sites and is beneficial for dissociative adsorption of water molecules. Current densities of 12.4 mA cm$^{-2}$ and 48.3 mA cm$^{-2}$ at 1.8 V are achieved for overall water electrolysis under neutral pH conditions and in seawater, respectively, when NiNS is applied as both the anode and cathode. This performance is significantly better than that of the benchmark Ir-C and Pt-C electrode system.

The third section of this thesis is to establish non-metal single iodine atom electrocatalysts for the HER. The single atom nickel iodide (SANi-I) electrocatalyst with atomically dispersed non-metal iodine atoms is prepared via a simple calcination step in a vacuum-sealed ampoule and subsequent cyclic voltammetry activation. Various advanced characterizations, including aberration-corrected high-angle annular dark-field scanning transmission electron microscopy and synchrotron-based X-ray absorption spectroscopy are applied to confirm the atomic-level dispersion of iodine atoms and detailed structure of SANi-I. Single iodine atoms are found to be isolated by oxygen atoms. The SANi-I exhibits robust structural stability and exceptional electrocatalytic activity for the HER. *In-situ* Raman spectroscopy reveals that the hydrogen adatom ($H_{ads}$) is adsorbed by a single iodine atom, forming the I-$H_{ads}$ intermediate, which promotes the HER process.

The fourth part of this thesis focuses on contemporaneous oxidation state manipulation of cobalt nitride and sulfide (CoNS) bifunctional electrocatalysts to accelerate intermediates desorption for both OER and HER. The contemporaneous manipulation of Co, N, and S oxidation states was realized via the simple synthesis of CoNS, in which cobalt foil was activated by hydrochloric acid to prepare activated cobalt (ACo) and afterwards ACo was sealed with thiourea in an evacuated ampoule to synthesize CoNS. The oxidation state analyses via X-ray photoelectron spectroscopy reveal that low Co oxidation state favors the OER while high N and S oxidation state promotes the HER. This indicates that the water splitting process for this electrocatalyst

is kinetically governed by intermediates desorption. A 100 mA cm$^{-2}$ OER current density is achieved for CoNS at an overpotential of 275 mV, which is lower than that for the Ir/C benchmark (374 mV) in 1.0 M KOH. A 4.5 mA cm$^{-2}$ current density at a voltage of 1.8 V is achieved for CoNS when employed for overall electrolysis in neutral buffer solution, which is higher than that for the noble-metal based system at the same voltage (3.4 mA cm$^{-2}$).

# Declaration

I certify that this work contains no material which has been accepted for the award of any other degree or diploma in my name, in any university or other tertiary institution and, to the best of my knowledge and belief, contains no material previously published or written by another person, except where due reference has been made in the text. In addition, I certify that no part of this work will, in the future, be used in a submission in my name, for any other degree or diploma in any university or other tertiary institution without the prior approval of the University of Adelaide and where applicable, any partner institution responsible for the joint-award of this degree.

I acknowledge that copyright of published works contained within this thesis resides with the copyright holder(s) of those works.

I also give permission for the digital version of my thesis to be made available on the web, via the University's digital research repository, the Library Search and also through web search engines, unless permission has been granted by the University to restrict access for a period of time.

Name of Candidate: Yongqiang Zhao

Signature:

Date: 28/06/2019

# Acknowledgement

This thesis would not have come to fruition without the tender support and knowledgeable enlightenment from my supervisors, colleagues, families and friends. I would like to express my gratitude to them all.

First and foremost, my heartfelt appreciation goes to my principal supervisor, Professor Shizhang Qiao, who has been enlightening me throughout my PhD research with his enthusiasm, fortitude, mastery, foresight and sagacity. I sincerely appreciate my co-supervisor Professor Bo Jin, who has been inspiring me with his optimism, amiability and profundity. I also want to thank my co-supervisor, Dr. Yan Jiao, for her insightful suggestions and passionate help.

I would like to express my appreciation and respect to those colleagues who assisted me in sample characterizations and data analysis: Dr Ashley Slattery, Dr Lisa O'Donovan and Dr Benjamin Wade at the University of Adelaide, Professor Tao Ling at Tianjin University and Professor Jun Luo at Tianjin University of Technology for transmission electron microscopy; Professor Li Song and Associate Professor Shuangming Chen at the University of Science and Technology of China for synchrotron-based X-ray absorption spectroscopy; Dr. Qiuhong Hu at the University of Adelaide for X-ray powder diffraction; Professor Lei Zhang at South China University of Technology for X-ray photoelectron spectroscopy; Mr. Ken Neubauer and Dr. Animesh Basak at the University of Adelaide for scanning electron microscopy.

It is also my great pleasure and honor to work with energetic and intelligent colleagues at the University of Adelaide, including Dr. Yao Zheng, Dr. Jingjing Duan, Dr. Sheng Chen, Dr. Chunxian Guo, Dr. Bo You, Dr. Cheng Tang, Dr. Dongliang Chao, Dr. Jingrun Ran, Dr. Lin Xiong, Dr. Bita Bayatsarmadi, Dr. Jinlong Liu, Dr. Lei Liu, Dr. Dongdong Zhu, Dr. MaiLin M JOhnes, Dr. Yusak Hartanto, Dr. Huzairy Hassan, Fangxi Xie, Xuesi Wang, Chao Ye, Anthony Vasileff, Huanyu Jin, Chaochen Xu, Xing Zhi, Jieqiong Shan, Xin Liu, Laiquan Li, Huan Li, Bingquan Xia, Xianlong Zhou, Dazhi Yao, Xin Xu, Yanzhao Zhang, Yang Shi, Cornelius Ngau, Khaled Abdalla, Zhining Shi, Sunjin Nam and Afshin Karami.

# Chapter 1 Introduction

## 1.1 Significance of the Project

Electrochemical water splitting into hydrogen and oxygen is one of the most attractive technologies for the production of hydrogen fuel because it can efficiently and sustainably convert electrical energy into chemical energy.[1, 2] Water electrolysis is the decomposition of water into oxygen gas through the oxygen evolution reaction (OER) at the anode and hydrogen gas via the hydrogen evolution reaction (HER) at the cathode.[3, 4] Both the OER and HER are generally limited to electrocatalysts that consist of scarce and expensive noble-metal materials (such as Ir-based for the OER and Pt-based for the HER). Thefefore, the development of non-precious metal electrocatalysts with high activity, low overpotential, and long-term stability for electrocatalytic water splitting is a crucial factor.[5-7] OER electrocatalysts perform well in alkaline media while HER electrocatalysts exhibit excellent activity in acidic media. However, the incompatible combination of OER and HER electrocatalysts in the same electrolyte leads to inferior electrocatalytic performance for overall water splitting.[8] As a result, highly efficient bifunctional electrocatalysts that simultaneously catalyze the OER and HER need to be developed to improve the efficiency for overall water electrolysis and reduce operational costs. However, common synthesis methods are generally tedious and uncontrollable.[9-12] Consequently, the development of highly-efficient and low-cost bifunctional electrocatalysts using simple and controllable techniques is particularly desirable for this field.

## 1.2 Research Objectives

The principal goals of this thesis are to develop a simple strategy, i.e. the ampoule method, for the controlled synthesis of highly-efficient and low-cost bifunctional electrocatalysts and to investigate their electrocatalytic mechanism. In particular, the objectives are:

- To develop novel cobalt selenide electrocatalyst for overall water electrolysis and conduct a synchrotron-based electrocatalytic mechanism study;
- To design interfacial regions for nickel nitride/sulfide electrocatalysts to improve

dissociative adsorption of water molecules and consequent electrocatalytic water splitting;

- To improve the number of electrochemically active sites by innovating non-metal single iodine atom electrocatalysts for the HER and investigate the key HER intermediate;

- To contemporaneously manipulate the oxidation state of activated cobalt nitride and sulfide bifunctional electrocatalysts to accelerate intermediates desorption for overall water electrolysis;

- To design and controllably fabricate highly-efficient and low-cost bifunctional electrocatalysts via the ampoule method and provide percipient insight into the electrocatalytic mechanism of resultant materials.

## 1.3 Thesis Outline

This thesis is the partial outcomes of my PhD research presented in the form of journal publications. The chapters in this thesis are presented in the following sequence:

- *Chapter 1* introduces the significance of the project and outlines the research objectives and key contributions to the ampoule method and electrocatalysts for water electrolysis;

- *Chapter 2* reviews literature regarding controllable material synthesis via the ampoule method and the applications of the as-prepared materials;

- *Chapter 3* focuses on charge state manipulation of cobalt selenide catalysts for overall water electrolysis and the synchrotron-based electrocatalytic mechanism study;

- *Chapter 4* develops interfacial nickel nitride/sulfide as a bifunctional electrode to promote dissociative adsorption of water molecules for highly efficient overall water electrolysis;

- *Chapter 5* increases the number of electrochemically active sites by innovating non-metal single iodine atom electrocatalysts for the HER and investigates the HER intermediate involved in the process;

- *Chapter 6* simultaneously manipulates the oxidation state of activated cobalt

nitride and sulfide bifunctional electrocatalysts to accelerate intermediates desorption for overall water electrolysis;

- **Chapter 7** presents the conclusions and perspectives for future work on electrocatalyst design and electrocatalytic mechanism studies.

## 1.4 References

1. F. Song, L. Bai, A. Moysiadou, S. Lee, C. Hu, L. Liardet and X. Hu, *J. Am. Chem. Soc.*, 2018, **140**, 7748-7759.

2. B. You and Y. Sun, *Acc. Chem. Res.*, 2018, **51**, 1571-1580.

3. N.-T. Suen, S.-F. Hung, Q. Quan, N. Zhang, Y.-J. Xu and H. M. Chen, *Chem. Soc. Rev.*, 2017, **46**, 337-365.

4. J. Wang, F. Xu, H. Jin, Y. Chen and Y. Wang, *Adv. Mater.*, 2017, **29**, 1605838.

5. S. Anantharaj, S. R. Ede, K. Sakthikumar, K. Karthick, S. Mishra and S. Kundu, *ACS Catal.*, 2016, **6**, 8069-8097.

6. J. Wang, W. Cui, Q. Liu, Z. Xing, A. M. Asiri and X. Sun, *Adv. Mater.*, 2016, **28**, 215-230.

7. V. Vij, S. Sultan, A. M. Harzandi, A. Meena, J. N. Tiwari, W.-G. Lee, T. Yoon and K. S. Kim, *ACS Catal.*, 2017, **7**, 7196-7225.

8. I. Roger, M. A. Shipman and M. D. Symes, *Nat. Rev. Chem.*, 2017, **1**, 0003.

9. X. Li, X. Hao, A. Abudula and G. Guan, *J. Mater. Chem. A*, 2016, **4**, 11973-12000.

10. B. Y. Guan, X. Y. Yu, H. B. Wu and X. W. Lou, *Adv. Mater.*, 2017, **29**, 1703614.

11. Y. Guo, T. Park, J. W. Yi, J. Henzie, J. Kim, Z. Wang, B. Jiang, Y. Bando, Y. Sugahara, J. Tang and Y. Yamauchi, *Adv. Mater.*, 2019, **31**, 1807134.

12. B. You, M. T. Tang, C. Tsai, F. Abild-Pedersen, X. Zheng and H. Li, *Adv. Mater.*, 2019, **31**, 1807001.

# Chapter 2 Literature Review

## 2.1 Introduction

The ampoule method provides a promising pathway towards controllable synthesis of novel electrocatalysts for water electrolysis due to its straightforward manipulation of reaction conditions, accessible experimental design, and controlled environment. This chapter reviews the development of the ampoule method and anticipates its application in electrocatalyst synthesis for water electrolysis. We first briefly introduce the history, device configuration, and merits of the ampoule method. Afterwards, we discuss typical materials that are synthesized by the ampoule method. Then, we highlight recent process in applying the ampoule method to synthesize electrocatalysts for water electrolysis. Finally, we discuss the opportunities and potentials of this method in facilitating electrocatalyst synthesis for water electrolysis.

## 2.2 The Ampoule Method: A Pathway towards Controllable Synthesis of Electrocatalysts for Water Electrolysis

This section is included as it appears as a journal paper by Yongqiang Zhao, Bo Jin, Anthony Vasileff, Bingyang Shi, Yan Jiao and Shi-Zhang Qiao, *Chemistry - A European Journal* 2019, submitted.

# Statement of Authorship

| Title of Paper | The Ampoule Method: A Pathway towards Controllable Synthesis of Electrocatalysts for Water Electrolysis |
|---|---|
| Publication Status | ☐ Published  ☐ Accepted for Publication  ☑ Submitted for Publication  ☐ Unpublished and Unsubmitted work written in manuscript style |
| Publication Details | Yongqiang Zhao, Bo Jin, Anthony Vasileff, Bingyang Shi, Yan Jiao and Shi-Zhang Qiao, Chemistry – A European Journal 2019, submitted. |

## Principal Author

| Name of Principal Author (Candidate) | Yongqiang Zhao | | |
|---|---|---|---|
| Contribution to the Paper | Manuscript drafting. | | |
| Overall percentage (%) | 70 | | |
| Certification: | This paper reports on original research I conducted during the period of my Higher Degree by Research candidature and is not subject to any obligations or contractual agreements with a third party that would constrain its inclusion in this thesis. I am the primary author of this paper. | | |
| Signature | | Date | 21/05/2019 |

## Co-Author Contributions

By signing the Statement of Authorship, each author certifies that:

  i.    the candidate's stated contribution to the publication is accurate (as detailed above);

  ii.   permission is granted for the candidate in include the publication in the thesis; and

  iii.  the sum of all co-author contributions is equal to 100% less the candidate's stated contribution.

| Name of Co-Author | Bo Jin | | |
|---|---|---|---|
| Contribution to the Paper | 8%. Discussion and manuscript revision. | | |
| Signature | | Date | 21.05.2019 |

| Name of Co-Author | Anthony Vasileff | | |
|---|---|---|---|
| Contribution to the Paper | 6%. Discussion and assistance with manuscript edit and polish. | | |
| Signature | | Date | 21.05.2019. |

| Name of Co-Author | Bingyang Shi | | |
|---|---|---|---|
| Contribution to the Paper | 3%. Discussion and manuscript revision. | | |
| Signature | BINGYANG SHI | Date | 15/06/2019 |

| Name of Co-Author | Yan Jiao | | |
|---|---|---|---|
| Contribution to the Paper | 3%. Discussion and manuscript revision. | | |
| Signature | | Date | 21 May 2019 |

| Name of Co-Author | Shi-Zhang Qiao | | |
|---|---|---|---|
| Contribution to the Paper | 10%. Supervision of the work and manuscript evaluation. | | |
| Signature | | Date | 21.05.2019 |

# The Ampoule Method: A Pathway towards Controllable Synthesis of Electrocatalysts for Water Electrolysis

Yongqiang Zhao,[a] Bo Jin,[a] Anthony Vasileff,[a] Bingyang Shi,[b] Yan Jiao,[a] and Shi-Zhang Qiao*[a]
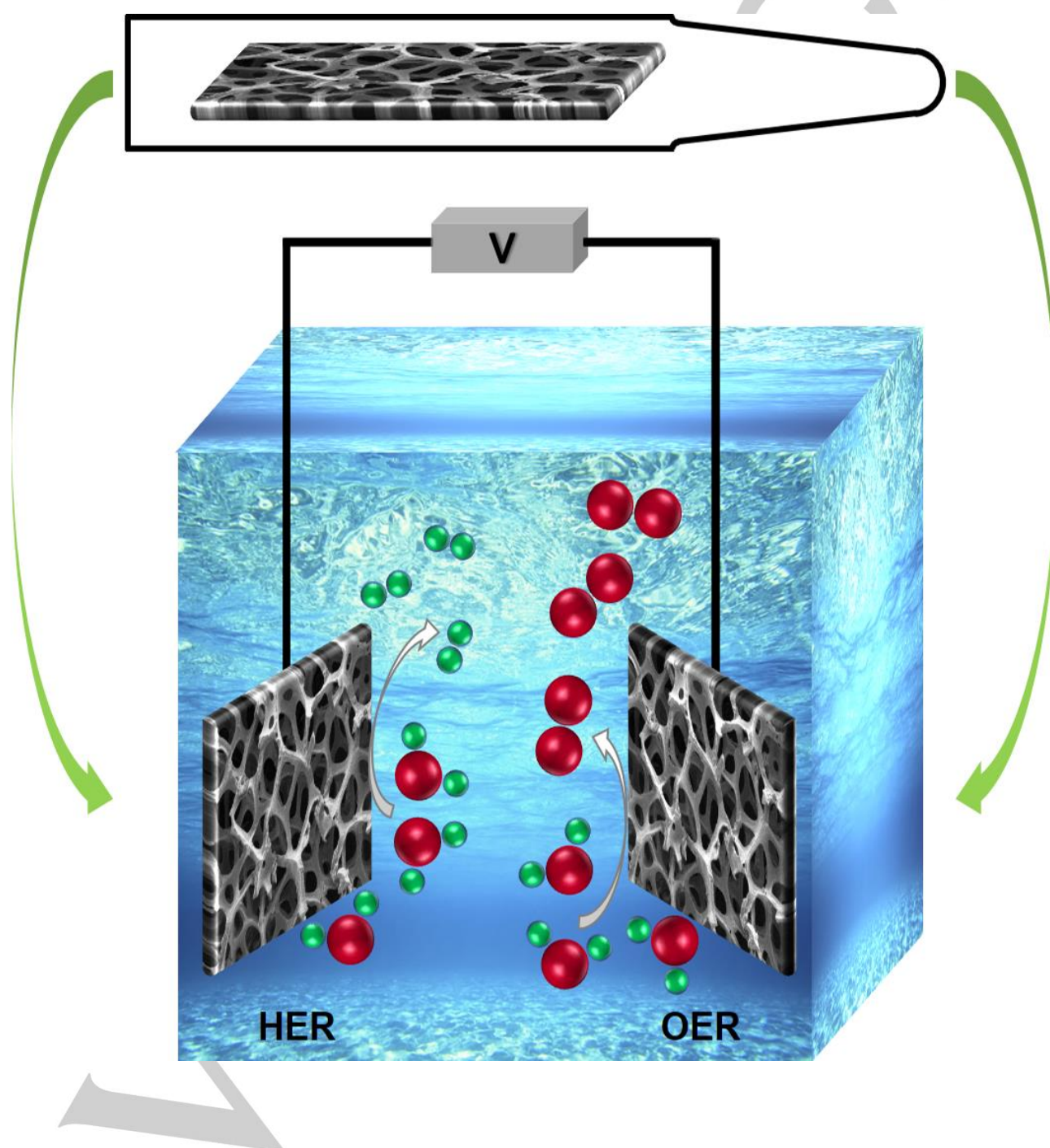
# CONCEPT

**Abstract:** The ampoule method provides a promising pathway towards controllable synthesis of novel electrocatalysts for water electrolysis due to its straightforward manipulation of reaction conditions, accessible experimental design, and controlled environment. This review introduces the development of the ampoule method and anticipates its application in electrocatalyst synthesis for water electrolysis. We first briefly introduce the history, device configuration, and merits of the ampoule method. Afterwards, we discuss typical materials that are synthesized by the ampoule method. Then, we highlight recent process in applying the ampoule method to synthesize electrocatalysts for water electrolysis. Finally, we discuss the opportunities and potentials of this method in facilitating electrocatalyst synthesis for water electrolysis.

## Introduction

The controllable synthesis of electrocatalysts for water electrolysis is an ongoing technological challenge for renewable hydrogen production.[1-5] Although numerous methods for material synthesis have been developed, including thermal routes,[6-8] chemical/physical vapour deposition,[9, 10] atomic layer deposition,[11] exfoliation,[12] sol-gel,[13] combustion,[14] microwave-induced,[15] electrochemical[16] and laser synthesis,[17] they suffer from unmanageable reaction conditions, environmental impact, and complicated device configuration. Therefore, controllable synthesis of water electrolysis catalysts via a simple method with accessible devices and controlled environment is highly desirable.
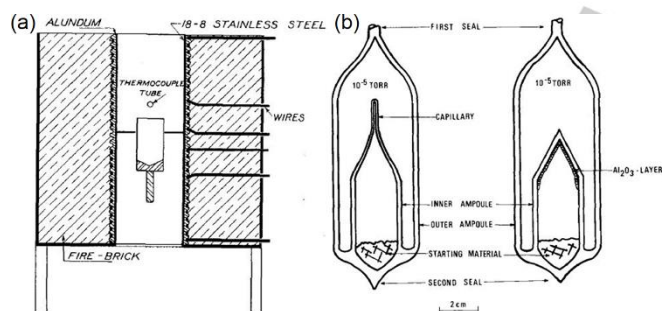


**Figure 1.** (a) Scheme of the ampoule developed by Stockbarger in cross section. The ampoule is vertically placed in a furnace. The top of the furnace is covered with an insulating lid and the bottom is open. Reproduced with permission from ref. [20]. Copyright 1936 American Institute of Physics. (b) Scheme of the ampoule featuring a vacuum jacket. Seed selection can be realized by the application of a capillary (left) and ampoule damage can be eliminated by coating the growth region with an evaporated $Al_2O_3$ layer (right). Adapted with permission from ref. [21]. Copyright 1971 Elsevier.

[a]   Y. Q. Zhao, Prof. B. Jin, A. Vasileff, Dr. Y. Jiao, Prof. S. Z. Qiao
      School of Chemical Engineering
      The University of Adelaide
      Adelaide, SA 5005, Australia
      E-mail: s.qiao@adelaide.edu.au
[b]   Prof. B. Shi
      School of Life Sciences
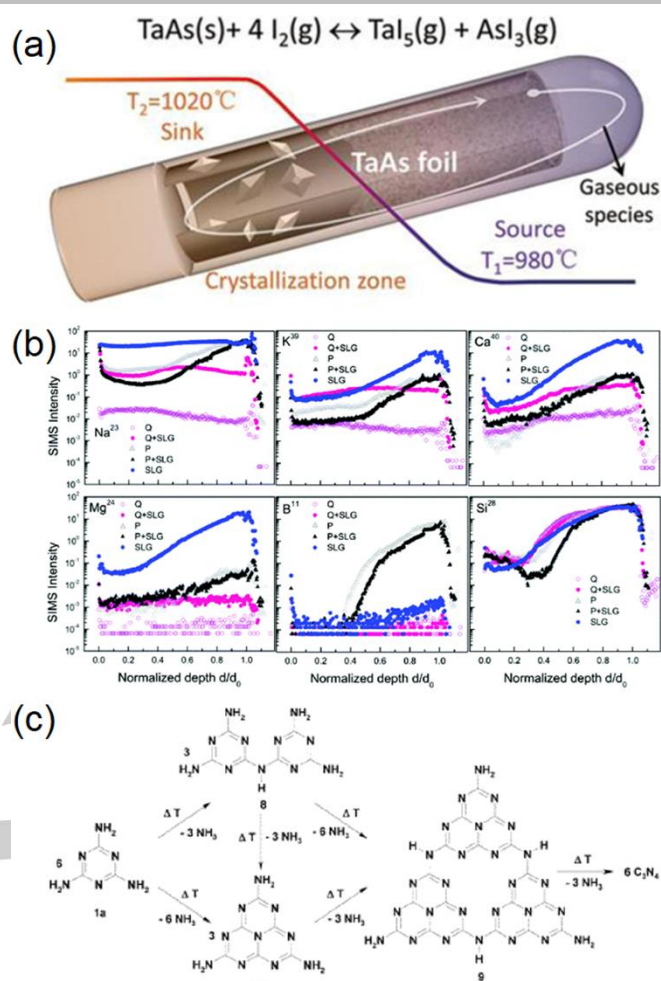      Henan University
      Kaifeng, Henan, 475004, China

**Figure 2.** (a) Schemes of the crystallization of TaAs in a temperature gradient via the ampoule method. TaAs is transported from the cooler end to the hotter part and crystallizes on the foil. Reproduced with permission from ref. [22]. Copyright 2016 American Chemical Society. (b) The time-of-flight secondary ion mass spectrometry (TOF-SIMS) depth profiles to study impurities Na, K, Ca, Mg, B and Si in copper zinc tin sulfide films synthesized on soda lime glass (SLG), Pyrex (P) and quartz (Q), with (P + SLG, Q + SLG) and without (P, Q) a bare SLG present in the ampoule. The SIMS intensity is shown in counts per primary ion pulse. Reproduced with permission from ref. [23]. Copyright 2014 The Royal Society of Chemistry. (c) Postulated condensation of melamine. Reproduced with permission from ref. [24]. Copyright 2003 American Chemical Society.

As a classical material synthesis pathway, the ampoule method is implemented in sealed ampoules that are placed in a furnace. Here, controllable synthesis is realized by manipulating reaction conditions and environmental impact is eliminated by the confined atmosphere.[18] The first work employing this method for material synthesis was reported by Bridgman in 1925.[19] Stockbarger later improved the ampoule method by implementing two vertically-situated furnaces separated by a baffle (Figure 1a).[20] A new ampoule was then developed which featured a vacuum jacket surrounding the growth chamber which reduces the radial temperature gradient and cooling (Figure 1b).[21] Material growth mechanisms via the ampoule method were also investigated. This included the thermodynamics (Figure 2a),[22] the role of impurity in material growth (Figure 2b),[23] and the intermediates (Figure 2c).[24] Diffusion that limits physical vapor transport in evacuated ampoules was modeled.[25]
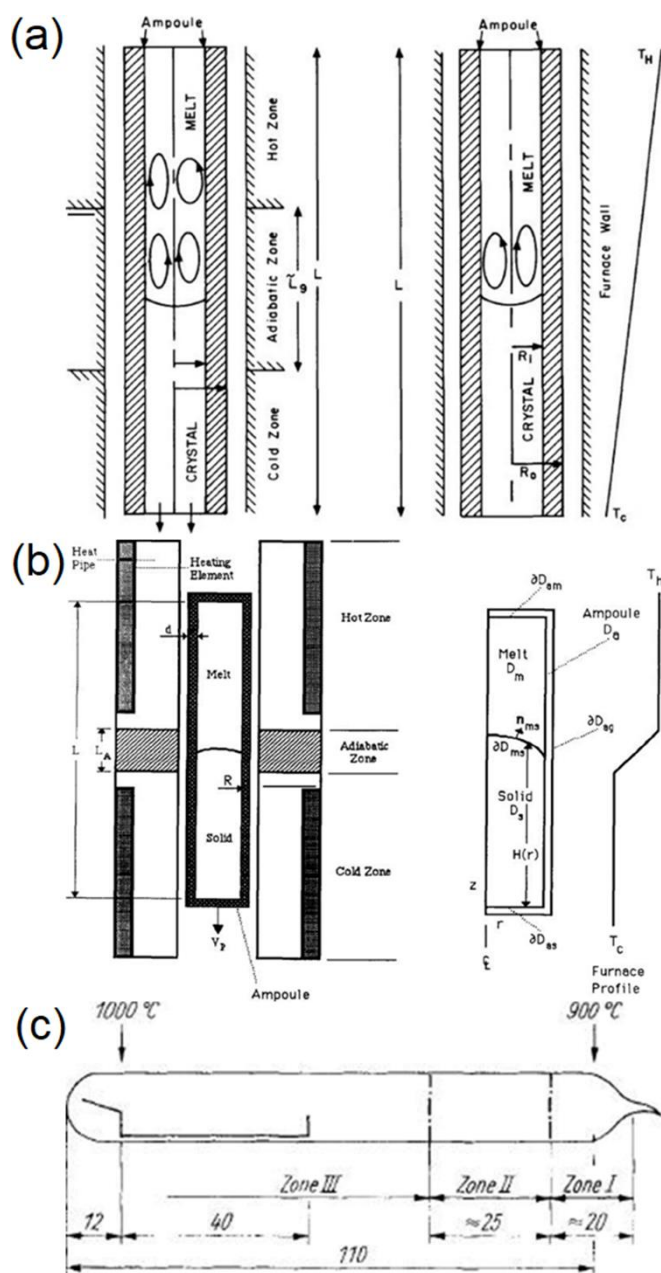
Figure 3 (a) Scheme of (left) the ampoule in a classical furnace and (right) a constant gradient furnace. Adapted with permission from ref. [32]. Copyright 1987 Elsevier. (b) Scheme of the vertical ampoule method (left) and its mathematical description (right). Adapted with permission from ref. [33]. Copyright 1992 Elsevier. (c) Schematic division of an ampoule into zones (dimensions in mm). Reproduced with permission from ref. [34]. Copyright 1970 Wiley-VCH.

Ampoules are made from silica, quartz, and corrosion-resistant niobium and tantalum and can be simply self-designed for various material synthesis. Starting materials are loaded inside the ampoule and thermally heated to react. The ampoule is evacuated or filled with inert gas. Afterwards, its open end is thermally melted and sealed. The ampoule method can be conducted over a wide temperature range, including low (≤ 300 °C),[26, 27] mild (300-900 °C)[28, 29] and high temperatures (≥ 1000 °C).[30, 31] Furnaces with heterogeneous or homogeneous

temperature can be applied. For the former configuration, isothermal hot and cold regions are formed and separated by an adiabatic zone (Figure 3a left), or a linear temperature profile is established by tapered heating (Figure 3a right).[32] The ampoule is transferred from the high temperature zone where starting materials melt and react, to the low temperature zone where material growth and crystallization occurs (Figure 3b);[33] or an elongated ampoule is statically placed in the furnace (Figure 3c).[34] For the latter configuration, the furnace is operated isothermally and the ampoule is not transferred. Ampoules can be easily self-designed and heated at a wide temperature range, whereby an extensive category of materials can be prepared via the ampoule method. Reaction conditions are easily manipulated, including reaction temperature and time, ratios of starting materials and/or ampoule transfer speed. The sealed ampoule eliminates environmental impacts and provides a confined atmosphere for volatile starting materials. Consequently, we expect that the ampoule method can provide a promising pathway towards controllable electrocatalyst synthesis for water electrolysis.

Herein, we review typical materials that are synthesized by the ampoule method, highlight recent progress in applying the ampoule method to synthesize electrocatalysts for water electrolysis and discuss the potential of this method in facilitating future electrocatalyst synthesis for water electrolysis.

## The Ampoule Method for Material Synthesis

The ampoule method exhibits great versatility in preparing various materials, including single crystals, alloys, nitrides and phosphides, chalcogenides and halides.
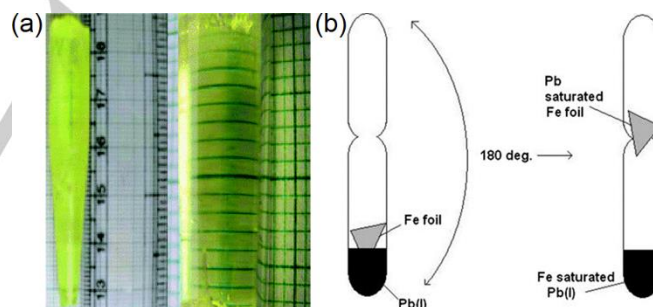


Figure 4 (a) Photographs of a benzil crystal grown in (left) a single-wall and (right) a double-walled ampoule. Adapted with permission from ref. [35]. Copyright 2011 The Royal Society of Chemistry. (b) Position of the samples inside the ampoule before (left) and after (right) equilibration. Reproduced with permission from ref. [39]. Copyright 2011 Elsevier.

The restricted atmosphere in the ampoule provides an impurity-free environment for single crystal growth. Both organic and inorganic single crystals can be prepared via the ampoule method. Typical organic single crystals include benzil (Figure 4a)[35] and benzimidazole[36] crystals for optical devices. Inorganic complex single crystals, such as magnetic $PrCo_2$[37] and superconducting $Ba_{1-x}Rb_xFe_2As_2$,[38] are synthesized via this method. Double-walled ampoules are applied to enable the crystal to expand along the C axis without restraint and circumvent the formation of cracks and dislocations in the crystal.

## CONCEPT

Ampoules provide easy access to self-design and are widely used for alloy preparation. A neck was devised in the middle of the ampoule for iron-lead alloy synthesis to separate the Fe saturated Pb melt and Pb saturated Fe foil after equilibration by turning the ampoule 180° before quenching into iced water (Figure 4b).[39] A double-ampoule was developed to overcome ampoule breaking and crystal cracking for $InAs_xSb_{1-x}$ alloy synthesis.[40] A carbon film was deposited on the inner wall of the ampoule to manipulate the microstructure and properties of GaSb alloys.[41]
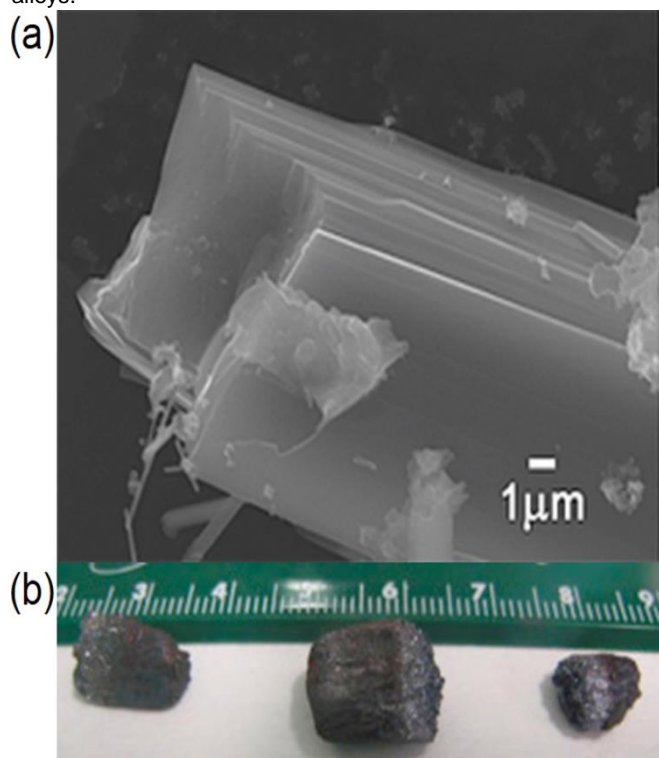


Figure 5 (a) Scanning electron microscopy image of $Sr_2Mg_3GaN_{4.33}$. Adapted with permission from ref. [46]. Copyright 2017 Wiley-VCH. (b) LiZnP grown by the ampoule method. Adapted with permission from ref. [51]. Copyright 2015 Elsevier.

Nitrides and phosphides have been prepared at mild temperature using the ampoule method. Due to silicon diffusion from the quartz ampoule to samples above 700 °C,[42] niobium and tantalum ampoules, which will not react with the precursors, are implemented to synthesize high-purity nitrides. In addition, the corrosion resistant niobium and tantalum ampoules also provide a mechanically robust reactor,[43] where highly active sodium azide is commonly used as a nitrogen source. The as-prepared nitrides include group (II) (Mg, Ca, Sr and Ba) nitrides (Figure 5a)[44-46] and group (III) nitrides, such as $GaN_3$[47] and $Al_2N_4$,[48] with doped lanthanide ion. Typical phosphides include zinc (Figure 5b)[49-51] and lanthanum phosphides.[52-54]

Chalcogenides can be easily synthesized in vacuum-sealed ampoules. The high gaseous sulfur pressure that is confined in vacuum-sealed ampoules benefits the sulfurization and crystallization of amorphous $FeS_2$ films, yielding highly-crystalline $FeS_2$ film, while flowing $H_2S$ is quantitatively insufficient to convert amorphous films into crystalline ones.[55] The controlled

atmosphere is critical for the synthesis of bismuth selenide which is reactive in open atmosphere at high temperature.[56] Ampoule rotation systems were applied to enhance the convection in the cadmium zinc telluride melt and prepare high-quality cadmium zinc telluride (CZT) (Figure 6a).[57, 58]
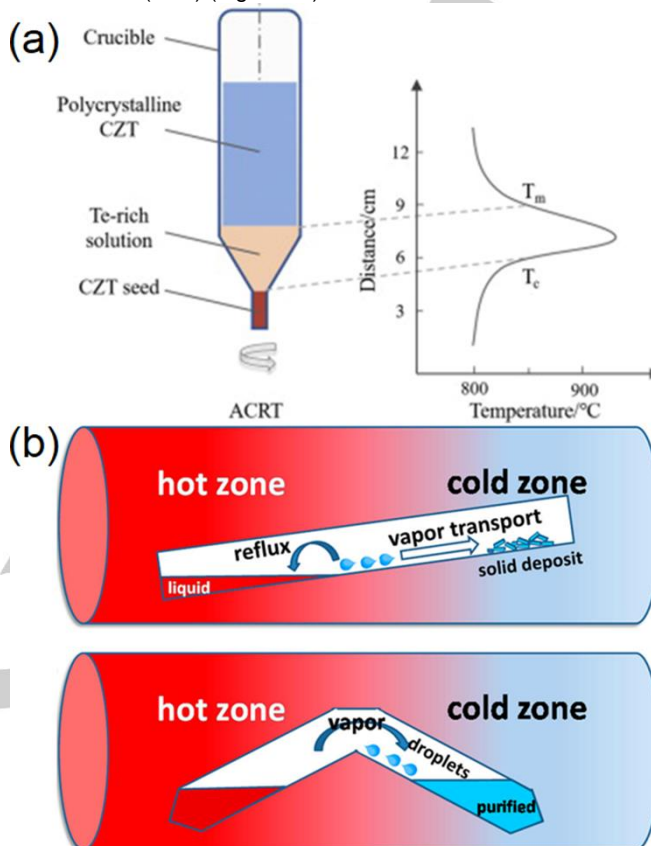


Figure 6 (a) Scheme of the ampoule method for CZT synthesis using accelerated crucible rotation technique (ACRT); (left) the ampoule and (right) thermal field; $T_c$ is the temperature at the growth interface and $T_m$ is the temperature at the dissolved interface. Adapted with permission from ref. [58]. Copyright 2018 Elsevier. (b) Scheme of (top) conventional purification by evaporation in a straight ampoule and (bottom) purification by evaporation in a bent ampoule. Adapted with permission from ref. [62]. Copyright 2018 American Chemical Society.

The toxicity and volatility of halogen elements requires a closed environment for halide synthesis, which can be realized by the ampoule method. When the reactions are performed in flowing inert gas, the process suffers from inferior control over the halogen concentration. Sealed ampoules are applied to precisely control the reaction and achieve high halogen content in the product. The organic fluorine source, polytetrafluoroethylene (PTFE, $-(CF_2-CF_2)_n-$), can decrease the temperature for fluoridation.[59] Chlorides and bromides that were synthesized by the ampoule method include mercury chloride and bromide[60] and lanthanum bromide.[61] Lin et al. reported the preparation of high purity $Tl_6SeI_4$ in which the purification of raw materials and the formation of $Tl_6SeI_4$ occurred simultaneously (Figure 6b).[62]

## The Application of Ampoule Method in Electrocatalysts Synthesis for Water

# CONCEPT

## Electrolysis

Although various materials have been synthesized via the ampoule method, their applications in water electrolysis are rarely reported. As nitrides, phosphides, and chalcogenides are widely used as electrocatalysts for water electrolysis, the ampoule method possesses great potential in electrocatalyst synthesis for water electrolysis.
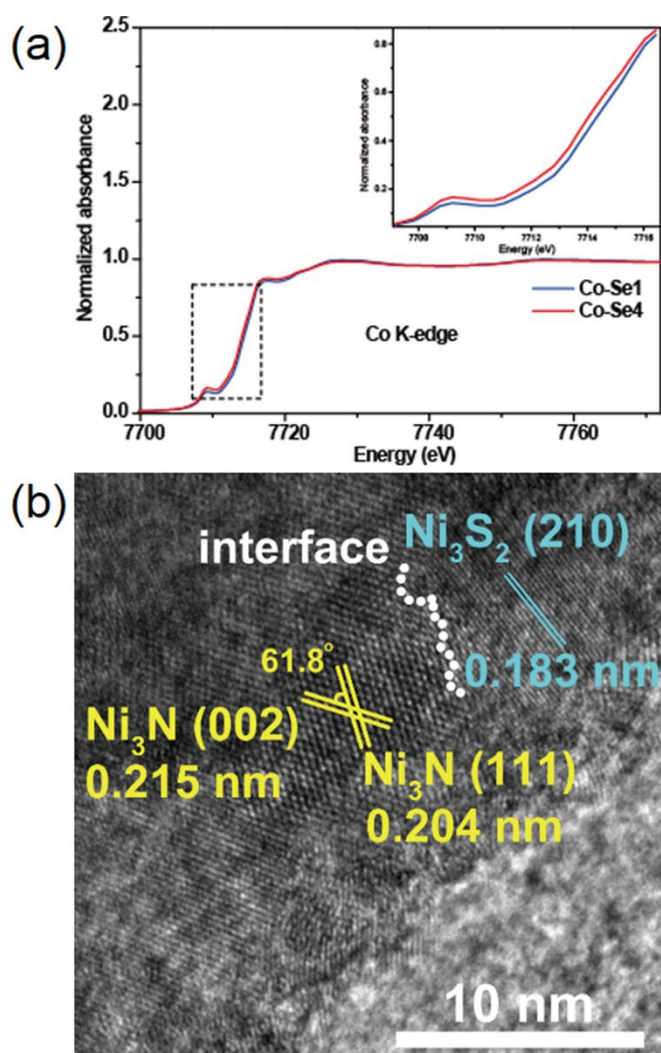


Figure 7 (a) Synchrotron-based Co K-edge X-ray absorption near-edge structure spectra and (insert) enlarged pre-edge spectra for cobalt selenide electrocatalysts. Adapted with permission from ref. [63]. Copyright 2018 Wiley-VCH. (b) High resolution transmission electron microscopy image of interfacial nickel nitride/sulfide electrocatalyst. Adapted with permission from ref. [64]. Copyright 2019 The Royal Society of Chemistry.

The ampoule method was implemented to synthesize cobalt selenide electrocatalysts.[63] This method was used to manipulate the cobalt charge state (Figure 7a) and electrocatalytic performance by controlling the Co to Se mass ratio in the precursor materials.[63] The cobalt selenide electrocatalysts consist of novel CoSe and $Co_9Se_8$ phases. A low Co charge state promotes hydrogen evolution reaction (HER) activity and a high Co charge state favors oxygen evolution reaction (OER)

performance. A 10.3 mA cm$^{-2}$ current density at 1.8 V is achieved for overall seawater electrolysis through exploiting as-synthesized cobalt selenide electrodes as both anode and cathode, which is three times higher than that for a noble-metal-based seawater electrolyzer at the same voltage (2.9 mA cm$^{-2}$).

A nickel nitride/sulfide electrocatalyst (NiNS), whereby $Ni_3N$ and $Ni_3S_2$ species are interfaced (Figure 7b), was synthesized via the ampoule method.[64] The resultant NiNS was employed directly as bifunctional electrocatalysts for water splitting with excellent activity toward the HER and OER. The significant electrocatalytic performance of NiNS was attributed to the interface between $Ni_3N$ and $Ni_3S_2$, which functions as the electrochemical active sites and is beneficial for dissociative adsorption of water molecules. Current densities of 12.4 mA cm$^{-2}$ and 48.3 mA cm$^{-2}$ at 1.8 V were achieved for overall water electrolysis under neutral pH conditions and in seawater, respectively, when NiNS was applied as both the anode and cathode. This performance was significantly better than that of the benchmark Ir-C and Pt-C electrode system.
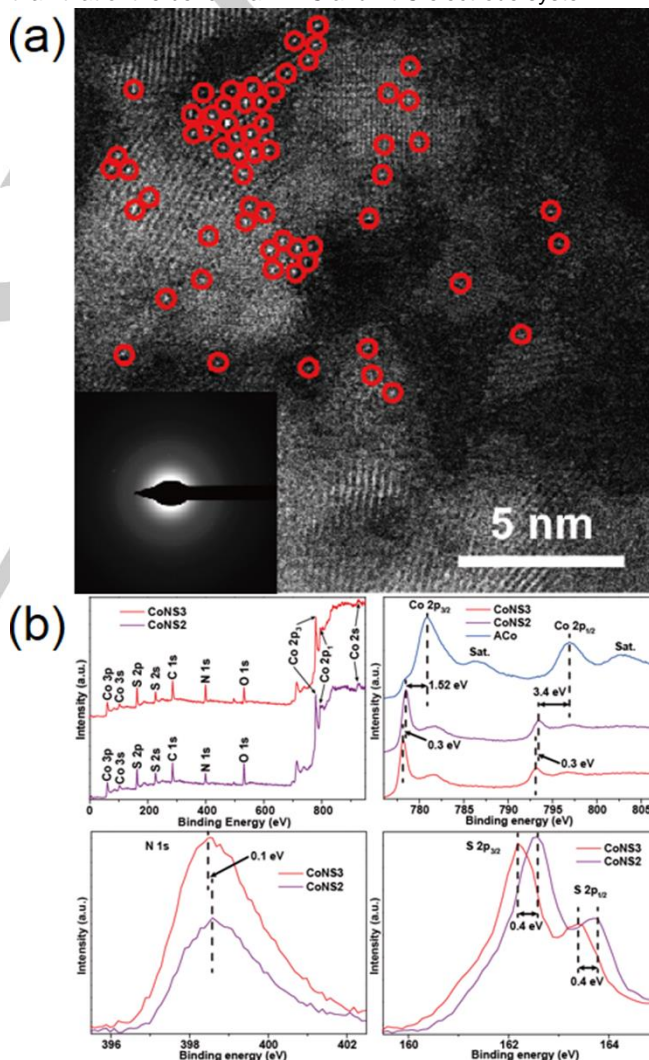


Figure 8 (a) Magnified HAADF-STEM image and (inset) corresponding selective area electron diffraction pattern of SANi-I. Adapted with permission from ref. [65]. Copyright 2019 Wiley-VCH. (b) (top left) X-ray photoelectron spectroscopy (XPS) survey spectra for CoNS, (top right) XPS spectra of Co 2p for CoNS and activated cobalt (ACo), XPS spectra of (bottom left) N 1s and (bottom right) S 2p for CoNS. Reproduced with permission from ref. [66]. Copyright 2019 The Royal Society of Chemistry.

A single atom nickel iodide (SANi-I) electrocatalyst with atomically dispersed non-metal iodine atoms for the HER was prepared via the ampoule method and subsequent cyclic voltammetry activation.[65] Aberration-corrected high-angle annular dark-field scanning transmission electron microscopy (HAADF-STEM) and synchrotron-based X-ray absorption spectroscopy confirmed the atomic-level dispersion of iodine atoms (Figure 8a) and detailed structure of SANi-I. In SANi-I, single iodine atoms are isolated by oxygen atoms. The SANi-I exhibits robust structural stability and exceptional electrocatalytic activity for the hydrogen evolution reaction. *In-situ* Raman spectroscopy reveals that hydrogen adatom ($H_{ads}$) are adsorbed by a single iodine atom, forming the I-$H_{ads}$ intermediate, which promotes the HER process.

The ampoule method was used to prepared cobalt nitride sulfide (CoNS) electrocatalysts.[66] The electrocatalytic performance was manipulated via contemporaneously tailoring the oxidation state of Co, N and S in the electrocatalysts (Figure 8b). A relatively low cobalt oxidation state led to a moderate bond strength which facilitates OER intermediates desorption; nitrogen and sulfur with a comparatively high oxidation state moderately bond with the HER intermediates and accelerate their desorption. The overall water splitting electrolyzer using CoNS as both the anode and cathode exhibited a decent cell voltage of 1.8 V to an output of 4.5 mA cm$^{-2}$ in neutral buffer solution, higher than that for the Ir-C and Pt-C electrode system (3.4 mA cm$^{-2}$).

## Summary and Outlook

In summary, the ampoule method has been widely applied to synthesize various materials due to its straightforward manipulation of reaction conditions, accessible experimental design, and controlled atmosphere. Material growth mechanisms, including the thermodynamics, the role of impurity in material growth, and the intermediates, have been investigated. Furnaces with heterogeneous or homogeneous temperature profiles are applied to heat starting materials that are sealed in the ampoule. Various materials can be synthesized via the ampoule method, including single crystals, alloys, nitrides and phosphides, chalcogenides, and halides. Material properties can be simply tailored by manipulating reaction conditions, including reaction temperature and time, ratios of starting materials and/or ampoule transfer speed. Therefore, we expect that the structure, composition and electrocatalytic properties of electrocatalysts can be easily manipulated via the ampoule method. Ampoules can be easily self-designed for various material synthesis and heated at a wide temperature range. Therefore, the number of electrocatalysts that can be prepared via the ampoule method is expected to be greatly increased. In addition, the controlled and impurity-free atmosphere benefits material synthesis where high-quality or reactive materials are prepared and toxic and volatile elements are used as starting materials. Consequently, novel electrocatalysts that cannot be obtained by other methods can be prepared by the ampoule method. Therefore, we anticipate the ampoule method will facilitate electrocatalyst synthesis for water electrolysis.

Despite the efficacy of the ampoule method for electrocatalyst design and synthesis, there are still two major challenges that need to be addressed. First, the majority of materials that have been synthesized via the ampoule method are bulk materials and do not possess nano-scaled morphology or structure, which may limit their applications in water electrolysis. A recent study shows that few-layer two-dimensional $WS_2$, $MoS_2$, $WSe_2$, $MoSe_2$, and $ReS_2$ can be synthesized via a microwave-induced-plasma assisted ampoule method.[67] In addition, it was believed that this method can be implemented to synthesize few-layer thin tellurides, arsenides, and antimonites. Therefore, it is anticipated that the ampoule method that is integrated with other synthesis technique will create new opportunities for nanomaterial synthesis. Second, the majority of material growth studies predominantly focus on the thermodynamics and ampoule design, which severely limit percipient comprehension of the mechanism of real-time material growth and deliberate material design. A clear understanding of electrocatalyst growth mechanisms *in operando* will enable us to develop devices for the ampoule method and consciously tailor the components, morphologies and structures of targeted electrocatalysts, aiming to improve their electrocatalytic performance. Progress regarding *in-situ* observation of material growth has been reported for physical vapor deposition synthesis via *in-situ* X-ray diffraction.[68] Consequently, the ampoule method that is integrated with *in-situ* characterizations, such as *in-situ* X-ray absorption spectroscopy,[69, 70] X-ray photoelectron spectroscopy,[71] infrared spectroscopy[72] and Raman spectroscopy[73] is anticipated to facilitate future electrocatalyst growth studies and guide their design.

[1]     Y. Shen, *J. Mater. Chem. A* **2015**, *3*, 13114-13188.
[2]     H. Osgood, S. V. Devaguptapu, H. Xu, J. Cho and G. Wu, *Nano Today* **2016**, *11*, 601-625.
[3]     M. D. Regulacio and M.-Y. Han, *Acc. Chem. Res.* **2016**, *49*, 511-519.
[4]     T.-F. Yi, J. Mei and Y.-R. Zhu, *J. Power Sources* **2016**, *316*, 85-105.
[5]     D. Zhang, B. Gökce and S. Barcikowski, *Chem. Rev.* **2017**, *117*, 3990-4103.
[6]     S. H. Sun, G. W. Meng, M. G. Zhang, X. H. An, G. S. Wu and L. D. Zhang, *J. Phys. D: Appl. Phys.* **2004**, *37*, 409-412.
[7]     L. Zheng, S. Han, H. Liu, P. Yu and X. Fang, *Small* **2016**, *12*, 1527-1536.
[8]     Z. Cai, Y. Bi, E. Hu, W. Liu, N. Dwarica, Y. Tian, X. Li, Y. Kuang, Y. Li, X.-Q. Yang, H. Wang and X. Sun, *Adv. Energy Mater.* **2018**, *8*, 1701694.
[9]     Y. Zhou, Q. Li, B. Dang, Y. Yang, T. Shao, H. Li, J. Hu, R. Zeng, J. He and Q. Wang, *Adv. Mater.* **2018**, *30*, 1805672.
[10]    R. Martínez-Morillas, R. Ramírez, J. Sánchez-Marcos, E. Fonda, A. de Andrés and C. Prieto, *ACS Appl. Mater. Interfaces* **2014**, *6*, 1781-1787.
[11]    L. Wen, M. Zhou, C. Wang, Y. Mi and Y. Lei, *Adv. Energy Mater.* **2016**, *6*, 1600468.
[12]    F. Li, M. Xue, X. Zhang, L. Chen, G. P. Knowles, D. R. MacFarlane and J. Zhang, *Adv. Energy Mater.* **2018**, *8*, 1702794.
[13]    G. D. Moon, J. B. Joo, M. Dahl, H. Jung and Y. Yin, *Adv. Funct. Mater.* **2014**, *24*, 848-856.
[14]    Y. Gao, X. Pu, D. Zhang, G. Ding, X. Shao and J. Ma, *Carbon* **2012**, *50*, 4093-4101.
[15]    S. Cho, J.-W. Jang, J. S. Lee and K.-H. Lee, *Nanoscale* **2012**, *4*, 2066-

2071.

[16] L. Qin, Y. Zhang, X. Wu, L. Nian, Z. Xie, L. Liu and Y. Ma, *Small* **2015**, *11*, 3028-3034.

[17] Y. Wang, A. Tabet-Aoul and M. Mohamedi, *J. Power Sources* **2015**, *299*, 149-155.

[18] P. Rudolph and F.-M. Kiessling, *Cryst. Res. Technol.* **1988**, *23*, 1207-1224.

[19] P. W. Bridgman, *Proc. Am. Acad. Arts Sci.* **1925**, *60*, 305-383.

[20] D. C. Stockbarger, *Rev. Sci. Instrum.* **1936**, *7*, 133-136.

[21] R. Widmer, *J. Cryst. Growth* **1971**, *8*, 216-218.

[22] Z. Li, H. Chen, S. Jin, D. Gan, W. Wang, L. Guo and X. Chen, *Cryst. Growth Des.* **2016**, *16*, 1172-1175.

[23] M. Johnson, S. V. Baryshev, E. Thimsen, M. Manno, X. Zhang, I. V. Veryovkin, C. Leighton and E. S. Aydil, *Energy. Environ. Sci.* **2014**, *7*, 1931-1938.

[24] B. Jürgens, E. Irran, J. Senker, P. Kroll, H. Müller and W. Schnick, *J. Am. Chem. Soc.* **2003**, *125*, 10288-10300.

[25] D. W. Greenwell, B. L. Markham and F. Rosenberger, *J. Cryst. Growth* **1981**, *51*, 413-425.

[26] O. Kysliak and J. Beck, *Eur. J. Inorg. Chem.* **2013**, *2013*, 124-133.

[27] T. Arivazhagan, G. Vinitha and N. P. Rajesh, *J. Cryst. Growth* **2019**, *512*, 181-188.

[28] Y. Cao, S. Yuan, M. Liu, B. Kang, B. Lu, J. Zhang and S. Cao, *J. Cryst. Growth* **2013**, *363*, 128-131.

[29] N. Eckstein, I. Krüger, F. Bachhuber, R. Weihrich, J. E. Barquera-Lozada, L. van Wüllen and T. Nilges, *J. Mater. Chem. A* **2015**, *3*, 6484-6491.

[30] M. Radziewski, T. Block, S. Klenner, Y. Zhang, B. P. T. Fokwa and O. Janka, *Inorg. Chem. Front.* **2019**, *6*, 137-147.

[31] S. Stein, S. F. Matar, L. Heletta and R. Pöttgen, *Solid State Sci.* **2018**, *82*, 70-77.

[32] P. M. Adornato and R. A. Brown, *J. Cryst. Growth* **1987**, *80*, 155-190.

[33] S. Brandon and J. J. Derby, *J. Cryst. Growth* **1992**, *121*, 473-494.

[34] H. Szydlowski, H. Lübbe and P. Kleinert, *Phys. Status Solidi A* **1970**, *3*, 769-778.

[35] T. Suthan, P. V. Dhanaraj, N. P. Rajesh, C. K. Mahadevan and G. Bhagavannarayana, *CrystEngComm* **2011**, *13*, 4018-4024.

[36] B. Riscob, N. Vijayan, M. Shakir, M. A. Wahab and G. Bhagavannarayana, *J. Appl. Crystallogr.* **2013**, *46*, 276-278.

[37] Y. Liu, Q. Lin, A. K. Pathak, D. Paudyal and T. A. Lograsso, *J. Cryst. Growth* **2019**, *507*, 209-212.

[38] J. Karpinski, N. D. Zhigadlo, S. Katrych, Z. Bukowski, P. Moll, S. Weyeneth, H. Keller, R. Puzniak, M. Tortello, D. Daghero, R. Gonnelli, I. Maggio-Aprile, Y. Fasano, Ø. Fischer, K. Rogacki and B. Batlogg, *Phys. C* **2009**, *469*, 370-380.

[39] I. Vaajamo and P. Taskinen, *Thermochim. Acta* **2011**, *524*, 56-61.

[40] M. Haris, Y. Hayakawa, F. C. Chou, P. Veeramani and S. Moorthy Babu, *J. Alloys Compd.* **2013**, *548*, 23-26.

[41] X. Gao, S. Zhai, J. Liu, D. Yang and W. Zhang, *J. Cryst. Growth* **2018**, *498*, 307-314.

[42] Z. Tang, D. Furniss, N. C. Neate, E. Barney, T. M. Benson and A. B. Seddon, *J. Am. Ceram. Soc.* **2016**, *99*, 2283-2291.

[43] R. Schmidt, M. Ströbele, K. Eichele and H.-J. Meyer, *Eur. J. Inorg. Chem.* **2017**, *2017*, 2727-2735.

[44] C. Poesl and W. Schnick, *Z. Anorg. Allg. Chem.* **2016**, *642*, 882-886.

[45] C. Poesl, R. Niklaus and W. Schnick, *Eur. J. Inorg. Chem.* **2017**, *2017*, 2422-2427.

[46] C. Poesl and W. Schnick, *Eur. J. Inorg. Chem.* **2017**, *2017*, 1498-1503.

[47] F. Hintze, N. W. Johnson, M. Seibald, D. Muir, A. Moewes and W. Schnick, *Chem. Mater.* **2013**, *25*, 4044-4052.

[48] P. Pust, F. Hintze, C. Hecht, V. Weiler, A. Locher, D. Zitnanska, S. Harm, D. Wiechert, P. J. Schmidt and W. Schnick, *Chem. Mater.* **2014**, *26*, 6113-6119.

[49] B. W. Montag, M. A. Reichenberger, K. R. Arpin, M. Sunder, K. A. Nelson, P. B. Ugorowski and D. S. McGregor, *J. Cryst. Growth* **2015**, *412*, 103-108.

[50] B. W. Montag, M. A. Reichenberger, N. Edwards, P. B. Ugorowski, M. Sunder, J. Weeks and D. S. McGregor, *J. Cryst. Growth* **2015**, *419*, 133-137.

[51] B. W. Montag, M. A. Reichenberger, M. Sunder, P. B. Ugorowski, K. A. Nelson and D. S. McGregor, *J. Cryst. Growth* **2015**, *419*, 143-148.

[52] J. Wang, K. Lee and K. Kovnir, *Inorg. Chem.* **2015**, *54*, 890-897.

[53] J. Wang, D. Kaseman, K. Lee, S. Sen and K. Kovnir, *Chem. Mater.* **2016**, *28*, 4741-4750.

[54] J. Wang, K. Lee and K. Kovnir, *Inorg. Chem.* **2017**, *56*, 783-790.

[55] S. Al Khateeb and T. D. Sparks, *J. Mater. Sci.* **2019**, *54*, 4089-4104.

[56] S. Gupta, N. Vijayan, A. Krishna, K. Thukral, K. K. Maurya, S. Muthiah, A. Dhar, B. Singh and G. Bhagavannarayana, *J. Appl. Crystallogr.* **2015**, *48*, 533-541.

[57] A. Datta, S. Swain, Y. Cui, A. Burger and K. Lynn, *J. Electron. Mater.* **2013**, *42*, 3041-3053.

[58] B. Zhou, W. Jie, T. Wang, L. Yin, F. Yang, B. Zhang, S. Xi and J. Dong, *J. Cryst. Growth* **2018**, *483*, 281-284.

[59] D. Hirai, O. Sawai, T. Nunoura and Z. Hiroi, *J. Fluorine Chem.* **2018**, *209*, 43-48.

[60] J.-S. Kim, S. B. Trivedi, J. Soos, N. Gupta and W. Palosz, *J. Cryst. Growth* **2008**, *310*, 2457-2463.

[61] H. Shi, L. Qin, W. Chai, J. Guo, Q. Wei, G. Ren and K. Shu, *Cryst. Growth Des.* **2010**, *10*, 4433-4436.

[62] W. Lin, O. Y. Kontsevoi, Z. Liu, S. Das, Y. He, Y. Xu, C. C. Stoumpos, K. M. McCall, A. J. E. Rettie, D. Y. Chung, B. W. Wessels and M. G. Kanatzidis, *Cryst. Growth Des.* **2018**, *18*, 3484-3493.

[63] Y. Zhao, B. Jin, Y. Zheng, H. Jin, Y. Jiao and S. Z. Qiao, *Adv. Energy Mater.* **2018**, *8*, 1801926.

[64] Y. Zhao, B. Jin, A. Vasileff, Y. Jiao and S. Z. Qiao, *J. Mater. Chem. A* **2019**, *7*, 8117-8121.

[65] Y. Zhao, T. Ling, S. Chen, B. Jin, A. Vasileff, Y. Jiao, L. Song, J. Luo and S. Z. Qiao, *Angew. Chem. Int. Ed.* **2019**, DOI: 10.1002/anie.201905554.

[66] Y. Zhao, B. Jin, A. Vasileff, Y. Jiao and S. Z. Qiao, *Chem. Commun.* **2019**, DOI: 10.1039/C9CC04231H.

[67] A. Chaturvedi, A. Slabon, P. Hu, S. Feng, K.-k. Zhang, R. R. Prabhakar and C. Kloc, *J. Cryst. Growth* **2016**, 450, 140-147.

[68] M. Ruiz-Osés, S. Schubert, K. Attenkofer, I. Ben-Zvi, X. Liang, E. Muller, H. Padmore, T. Rao, T. Vecchione, J. Wong, J. Xie and J. Smedley, *APL Mater.* **2014**, 2, 121101.

[69] Y. Gorlin, B. Lassalle-Kaiser, J. D. Benck, S. Gul, S. M. Webb, V. K. Yachandra, J. Yano and T. F. Jaramillo, *J. Am. Chem. Soc.* **2013**, 135, 8525-8534.

[70] B. Lassalle-Kaiser, D. Merki, H. Vrubel, S. Gul, V. K. Yachandra, X. Hu and J. Yano, *J. Am. Chem. Soc.* **2015**, 137, 314-321.

[71] H. Ali-Löytty, M. W. Louie, M. R. Singh, L. Li, H. G. Sanchez Casalongue, H. Ogasawara, E. J. Crumlin, Z. Liu, A. T. Bell, A. Nilsson and D. Friebel, *J. Phys. Chem. C* **2016**, 120, 2247-2253.

[72] Y. Liu, S. Chen, X. Quan and H. Yu, *J. Am. Chem. Soc.* **2015**, 137, 11631-11636.

[73] Y. Deng and B. S. Yeo, *ACS Catal.* **2017**, 7, 7873-7889.

## CONCEPT

**Entry for the Table of Contents**

## CONCEPT

The ampoule method provides a promising pathway towards controllable synthesis of novel electrocatalysts for water electrolysis. The history, device configuration and merits of the ampoule method are introduced. Typical materials that are synthesized by the ampoule method are discussed. Electrocatalyst synthesis via the ampoule method for water electrolysis is highlighted and anticipated.
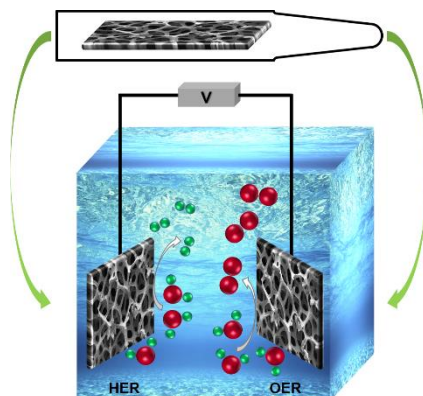
*Yongqiang Zhao, Bo Jin, Anthony Vasileff, Bingyang Shi, Yan Jiao, and Shi-Zhang Qiao\**

*Page No. – Page No.*

**The Ampoule Method: A Pathway towards Controllable Synthesis of Novel Electrocatalysts for Water Electrolysis**

# Chapter 3 Charge State Manipulation of Cobalt Selenide Catalyst for Overall Seawater Electrolysis

## 3.1 Introduction and Significance

The development of bifunctional electrocatalysts for overall seawater electrolysis with high activity and stability is preferable for commercialized hydrogen production and yet remains challenging. Cobalt selenide has been considered as promising electrocatalyst and Co charge state of cobalt selenide plays a key role in electrocatalytic activity. However, conventional preparations fail to manipulate Co charge state. Consequently, it is imperative to develop a facile method to manipulate Co charge state and electrocatalytic activity. Here, manipulation of Co charge state and electrocatalytic activity was realized by one-step calcination in vacuum-sealed ampoule, catalytic mechanism was studied by synchrotron-based analysis, and the as-prepared cobalt selenide electrodes exhibited excellent electrocatalytic performance for overall seawater electrolysis. The highlights of this work include:

- One-step calcination in vacuum-sealed ampoule was firstly applied to synthesized cobalt selenide electrocatalysts with CoSe and $Co_9Se_8$ phases. Manipulation of Co charge state and electrocatalytic activity of cobalt selenide was achieved by controlling the mass ratio of Co foil to Se powder.

- Synchrotron-based X-ray absorption near-edge structure (XANES) and extended X-ray absorption fine structure (EXAFS) were applied to characterize Co charge state and to study catalytic mechanism. Co K-edge of cobalt selenide with higher OER activity shifts toward higher energy (higher Co charge state) and Co K-edge of cobalt selenide with higher HER activity shifts toward lower energy (lower Co charge state). It can be concluded that high Co charge state favors OER performance and low Co charge state promotes HER activity for as-prepared cobalt selenide electrocatalysts.

- Owing to exposed electrocatalytic centers and rapid charge transfer capability, as-prepared cobalt selenide electrodes displayed excellent electrocatalytic activity and stability, which compared favorably with that of novel metal based electrocatalyst

for water splitting in alkaline media. A 10.3 mA/cm$^2$ current density at a voltage of 1.8 V was achieved for overall seawater electrolysis, which was three times higher than that for novel-metal-based seawater electrolyzer at the same voltage (2.9 mA/cm$^2$).

## 3.2 Charge State Manipulation of Cobalt Selenide Catalyst for Overall Seawater Electrolysis

This chapter is included as it appears as a journal paper published by Yongqiang Zhao, Bo Jin, Yao Zheng, Huanyu Jin, Yan Jiao and Shi-Zhang Qiao, *Advanced Energy Materials* 2018, 8, 1801926.

# Statement of Authorship

| Title of Paper | Charge State Manipulation of Cobalt Selenide Catalyst for Overall Seawater Electrolysis |
|---|---|
| Publication Status | ☑ Published      ☐ Accepted for Publication<br><br>☐ Submitted for Publication      ☐ Unpublished and Unsubmitted work written in manuscript style |
| Publication Details | Yongqiang Zhao, Bo Jin, Yao Zheng, Huanyu Jin, Yan Jiao and Shi-Zhang Qiao, Advanced Energy Materials 2018, 8, 1801926. |

## Principal Author

| Name of Principal Author (Candidate) | Yongqiang Zhao |
|---|---|
| Contribution to the Paper | Research plan, material synthesis, most of the characterizations and data analysis, electrochemical measurements and manuscript drafting. |
| Overall percentage (%) | 70 |
| Certification: | This paper reports on original research I conducted during the period of my Higher Degree by Research candidature and is not subject to any obligations or contractual agreements with a third party that would constrain its inclusion in this thesis. I am the primary author of this paper. |
| Signature | Date    21/05/2019 |

## Co-Author Contributions

By signing the Statement of Authorship, each author certifies that:

i. the candidate's stated contribution to the publication is accurate (as detailed above);

ii. permission is granted for the candidate in include the publication in the thesis; and

iii. the sum of all co-author contributions is equal to 100% less the candidate's stated contribution.

| Name of Co-Author | Bo Jin |
|---|---|
| Contribution to the Paper | 8%. Discussion of research plan, data analysis and manuscript revision. |
| Signature | Date    21.05.2019 |

| Name of Co-Author | Yao Zheng |
|---|---|
| Contribution to the Paper | 4%. Discussion of research plan and data analysis. |
| Signature | Date    21st. May. 2019 |

| Name of Co-Author | Huanyu Jin | | |
|---|---|---|---|
| Contribution to the Paper | 4%. Assistance with electrochemical tests and data analysis. | | |
| Signature | | Date | 21. 05. 2019. |

| Name of Co-Author | Yan Jiao | | |
|---|---|---|---|
| Contribution to the Paper | 4%. Discussion of research plan and data analysis. | | |
| Signature | | Date | 21 May 2019 |

| Name of Co-Author | Shi-Zhang Qiao | | |
|---|---|---|---|
| Contribution to the Paper | 10%. Supervision of the work, data interpretation and manuscript evaluation. | | |
| Signature | | Date | 21.05.2019 |

**FULL PAPER**

Seawater Electrolysis

ADVANCED
ENERGY
MATERIALS

www.advenergymat.de

# Charge State Manipulation of Cobalt Selenide Catalyst for Overall Seawater Electrolysis

*Yongqiang Zhao, Bo Jin, Yao Zheng, Huanyu Jin, Yan Jiao, and Shi-Zhang Qiao\**

Facile and controllable fabrication of highly active and stable bifunctional electrocatalysts for water electrolysis is important for hydrogen production. 3D cobalt selenide electrodes with CoSe and $Co_9Se_8$ phases are synthesized by one-step calcination of Co foil with Se powder in a vacuum-sealed ampoule. The charge state of Co species and the electrocatalytic performance of the prepared catalysts are manipulated by controlling Co to Se mass ratio. Mechanistic studies show that a high Co charge state favors oxygen evolution reaction performance and a low Co charge state promotes hydrogen evolution reaction activity for as-prepared cobalt selenide electrocatalysts. The resultant materials can act as free-standing bifunctional electrocatalytic electrodes for oxygen evolution reaction and hydrogen evolution reaction in alkaline media. Moreover, a 10.3 mA cm$^{-2}$ current density at 1.8 V is achieved for overall seawater electrolysis through exploiting as-synthesized cobalt selenide electrodes as both anode and cathode, which is three times higher than that for novel-metal-based seawater electrolyzer at the same voltage (2.9 mA cm$^{-2}$). Experimental results reveal that the cobalt selenide electrodes show significantly higher electrocatalytic performance than that of integrated Ni/Ir–C and Ni/Pt–C electrodes. Consequently, these novel bifunctional electrodes are promising candidates for realistic large-scale water electrolysis.

## 1. Introduction

Electrochemical water splitting into hydrogen and oxygen is one of the most attractive sustainable technologies for production of hydrogen fuel by converting electrical energy into chemical energy.[1–4] The water electrolysis is the decomposition of water into oxygen gas ($O_2$) through oxygen evolution reaction (OER) at anode and hydrogen gas ($H_2$) via hydrogen evolution reaction (HER) at cathode. Both OER and HER are circumscribed by extortionate electrocatalysts that consist of noble-metal materials (such as Ir-based for OER and Pt-based for HER).[5,6]

The development of nonprecious metal electrocatalysts with high activity, low overpotential, and long-term stability for electrocatalytic water splitting has been vigorously investigated. The electrocatalysts include perovskite oxides[7,8] and transition metal oxides/hydroxides[9–11] for OER electrocatalysis, and transition metal borides/carbides/nitrides/phosphides/sulfides/selenides[12–19] for HER electrocatalysis. OER electrocatalysts perform well in basic media, while HER electrocatalysts exhibit excellent activity in acid media. However, the incompatible combination of OER and HER electrocatalysts in the same electrolyte leads to inferior electrocatalytic performance of overall water splitting. Considering sustainable $H_2$ production, overall seawater splitting is a promising candidate for commercialization toward mass $H_2$ production.[20] As a result, highly efficient bifunctional electrocatalysts that simultaneously catalyze OER and HER in seawater splitting need to be developed for improving overall water electrolysis efficiency and reducing operation costs. Recent study indicates that the development of alternative bifunctional electrocatalysts for overall seawater electrolysis with high activity and low overpotential is eminently desirable and yet remains challenging.[21]

Cobalt selenide, as a typical transition metal dichalcogenide and newly discovered alternative earth-abundant electrocatalyst, has recently drawn broad attention owing to its excellent electrocatalytic activity, high chemical stability, and low cost.[6,22,23] The electrocatalytic activity of cobalt selenide electrocatalysts is mainly ascribed to proper surface active sites, resulting in moderate bonds between Se/Co species in the catalysts and reaction intermediates (*OOH for OER and H* for HER) associated with water electrolysis. The catalyst electrodes are fabricated in hydro/solvothermal route that comprises relatively laborious and sophisticated steps, followed by loading on a current collector by binders.[23–25] Alternative synthesis methods are reported as electrochemical deposition[26,27] and direct selenization in open tube.[28,29] However, these methods are unable to manipulate charge state of Co species, resulting in failing to modulate the OER and HER electrocatalytic performance.[30,31] Moreover, the most reported cobalt selenide electrocatalysts for water splitting are $CoSe_2$ based materials. Only a few case studies on $Co_{0.85}Se$[32] and $Co_3Se_4$[33] as electrocatalysts were reported. There is no reported study in the application of cobalt selenide

Y. Q. Zhao, Prof. B. Jin, Dr. Y. Zheng, H. Jin, Dr. Y. Jiao, Prof. S.-Z. Qiao
School of Chemical Engineering
The University of Adelaide
Adelaide, SA 5005, Australia
E-mail: s.qiao@adelaide.edu.au
Prof. S.-Z. Qiao
School of Materials Science and Engineering
Tianjin University
Tianjin 300072, China

The ORCID identification number(s) for the author(s) of this article can be found under https://doi.org/10.1002/aenm.201801926.

**ADVANCED**
**SCIENCE NEWS**
www.advancedsciencenews.com

**ADVANCED**
**ENERGY**
**MATERIALS**
www.advenergymat.de

electrocatalysts for seawater splitting. Therefore, it is important to develop a facile and controllable method to fabricate novel cobalt selenide electrocatalysts with controllable Co charge state and electrocatalytic performance for seawater splitting.

Here, we report the development of novel 3D free standing cobalt selenide electrodes consisting of CoSe and $Co_9Se_8$ phases. The cobalt selenide catalyst electrodes were prepared by directly selenizing Co foil with Se powder in vacuum-sealed ampoule. The charge state of Co species (i.e., relative mole ratio of $Co^{3+}/Co^{2+}$) and electrocatalytic performance of the cobalt selenide catalysts were manipulated by controlling the mass ratio of Co foil to Se powder. Synchrotron-based mechanism study reveals that high Co charge state favors OER performance and low Co charge state promotes HER activity. As-prepared electrocatalysts shows 3D network which facilitates charge transfer, and delivers efficient and stable electrocatalytic performance. Inspired by efficient electrocatalytic capability, a seawater electrolyzer was setup using as-synthesized cobalt selenide electrodes as an anode and a cathode. Experimental results show that these cobalt selenide electrodes exhibit a low onset potential and electrocatalytic activity retention in seawater compared with novel metal counterpart. It is concluded that the novel design and fabrication of unique cobalt selenide

electrocatalysts will provide a promising pathway for promoting overall performance and reducing operation costs of water electrolysis for $H_2$ production.

## 2. Results and Discussion

### 2.1. Synthesis and Characterization

The 3D cobalt selenide catalytic electrodes were synthesized by a facile one-step selenization of Co foil with Se powder in a vacuum sealed ampoule. One piece of precleaned Co foil and Se powder were sealed in ampoule under vacuum and calcinated at 550 °C for 5 h. A variety of Co to Se mass ratio, i.e., 1:0.02, 1:0.037, 1:0.085, 1:0.142, and 1:0.2, was employed, which are denoted as Co–Se1, Co–Se2, Co–Se3, Co–Se4, and Co–Se5 respectively. Among them, Co–Se1 exhibits best OER electrocatalytic activity and Co–Se4 shows optimal HER performance. During this process, Co foil was selenized by selenium vapor under a pressure. This can be confirmed by the elemental distribution mapping (inset of **Figure 1**b,d) and energy dispersive spectra (EDS) (inset of Figure S1a,b in the Supporting Information) that clearly show the element of Se in the Co–Se1
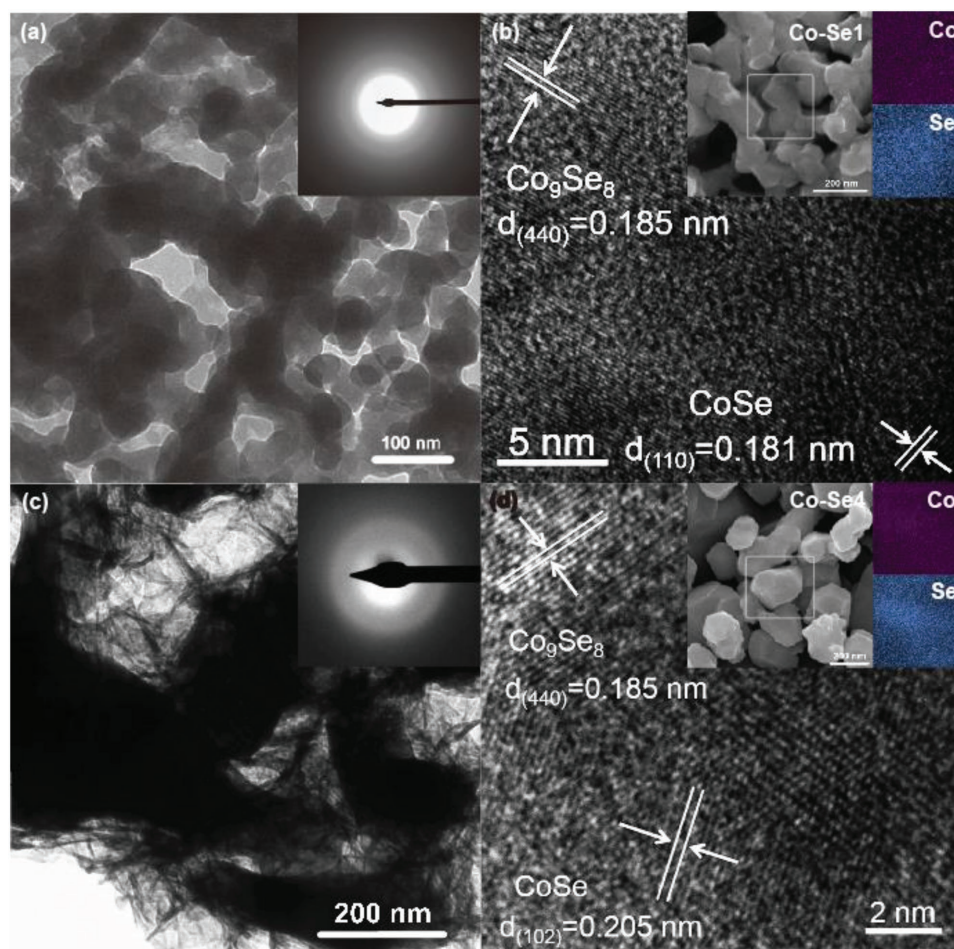


**Figure 1.** TEM images and (inset) corresponding SAED pattern of a) Co–Se1 and c) Co–Se4; HRTEM images, (inset) SEM and elemental distribution mapping of b) Co–Se1 and d) Co–Se4.

ADVANCED
SCIENCE NEWS
www.advancedsciencenews.com

ADVANCED
ENERGY
MATERIALS
www.advenergymat.de

and Co–Se4, respectively. Based on EDS, Element contents of Co and Se for Co–Se1 are calculated as 57.44% and 42.56% respectively and those for Co–Se4 are calculated as 37.75% and 62.25% respectively. As shown in Figure S1 in the Supporting Information, the as-synthesized free-standing electrodes exhibit 3D network. Scanning electron microscopy (SEM) images further reveal that both Co–Se1 (inset of Figure 1b) and Co–Se4 (inset of Figure 1d) electrodes consist of densely packed nanoparticles in the dimension of tens of nanometers. The fragments of Co–Se1 and Co–Se4 (exfoliated from the resulting electrodes) were studied by the transmission electron microscopy (TEM) and high resolution TEM (HRTEM), as shown in Figure 1. The TEM images demonstrate crystal structure of Co–Se1 (Figure 1a) and Co–Se4 (Figure 1c). The HRTEM images show clear lattice fringes of Co–Se1 (Figure 1b) with interplanar spacing of 0.181 and 0.185 nm, corresponding to the CoSe (110) and $Co_9Se_8$ (440) plane, and Co–Se4 (Figure 1d) with interplanar spacing of 0.205 and 0.185 nm corresponding to the CoSe (102) and $Co_9Se_8$ (440) plane. This indicates that both Co–Se1 and Co–Se4 possess CoSe and $Co_9Se_8$ phases. The selective area electron diffraction (SAED) patterns (inset of Figure 1a,c) display several continuous bright rings, indicating polycrystal nature of as-prepared Co–Se1 and Co–Se4.

The crystal structure of Co–Se1 and Co–Se4 was characterized by X-ray diffraction (XRD), as shown in **Figure 2**a. The diffraction peaks of Co–Se1 and Co–Se4 are consistent with the (100), (101), (102), (110), (103), (201), and (202) planes for CoSe (PDF# 70-2870), as well as the (311), (222), (511), (440), and (622) planes for $Co_9Se_8$ (PDF# 89-4180), which coincide with the HRTEM images, both indicating conversion of cobalt metal into polycrystal cobalt selenide. Three diffraction peaks of Co foil are still retained for Co–Se1 after selenization, while two diffraction peaks of Co foil are observed for Co–Se4.

Surface chemistry of the synthesized cobalt selenide electrodes was analyzed by X-ray photoelectron spectroscopy (XPS). The XPS survey spectra clearly display the presence of Se in Co–Se1 (Figure S2a, Supporting Information) and Co–Se4 (Figure S2b, Supporting Information), respectively. The different bonding states of Co 2p for Co–Se1 (Figure 2b) and Co–Se4 (Figure 2c) were certified by XPS spectra of Co 2p and the deconvolution procedure. Figure 2b,c shows that there are two core-level signals of Co in Co–Se1 and Co–Se4 located at ≈780 and 797 eV, which are attributed to $Co_{2p3/2}$ and $Co_{2p1/2}$, respectively. After deconvolution, the peaks at 778.3 eV for Co–Se1 and 778.4 eV for Co–Se4 are assigned to $Co^0$,[31] which is attributed to Co substrate. The relative mole ratio of $Co^{3+}$/$Co^{2+}$ of the materials was calculated as 2.77:1 for Co–Se1 and 2.02:1 for Co–Se4, indicating a higher concentration of $Co^{3+}$ in Co–Se1.[31,34] These results further demonstrate the coexistence of CoSe and $Co_9Se_8$ in the cobalt selenide catalysts. The high resolution Se 3d XPS spectra of Co–Se1 and Co–Se4 are shown in Figure S2c,d in the Supporting Information. The binding energies at ≈54 and 55 eV correspond to Se $3d_{5/2}$ and $3d_{3/2}$, respectively. The wide peak at ≈59.7 eV discloses the presence of $SeO_x$ in both Co–Se1 and Co–Se4.[22]

Additional information about the electronic nature and charge states of Co–Se1 and Co–Se4 was obtained from synchrotron-based X-ray absorption near-edge structure (XANES) and extended X-ray absorption fine structure (EXAFS) analysis.

Figure 2d shows the Co K-edge XANES spectra of Co–Se1 and Co–Se4. The enlarged preedge spectra show that Co–Se1 shifts toward higher energy compared to that of Co–Se4, indicating higher charge state of Co species in Co–Se1,[35] which is caused by a negative charge transfer from Co to Se.[36] This result corresponds well to the fact that Co–Se1 has higher concentration of $Co^{3+}$, which is demonstrated by deconvoluted Co 2p XPS spectra. Furthermore, Figure 2e displays the Fourier transformed $k^3$ – weighted EXAFS spectra for Co–Se1 and Co–Se4. Both Co–Se1 and Co–Se4 exhibit a strong peak at ≈2 Å, which can be assigned to the typical Co–Se bond. Clearly, the peak intensity of Co–Se1 is higher than that of Co–Se4, indicating higher coordination number of Co species for Co–Se1.[35]

## 2.2. Catalytic Performances of OER, HER, and Overall Water Splitting

The OER activities of Co–Se1 and Co–Se4 electrodes were assessed by directly using these 3D networked materials as the working electrodes in $O_2$-saturated 1.0 M KOH solution at a scan rate of 5 mV s$^{-1}$ in a typical three-electrode apparatus. For comparison, bare cobalt foil and Ir–C loaded on Ni foam were prepared to evaluate their OER electrocatalytic performance. The linear sweep voltammetry (LSV) curves demonstrate that Co–Se1 exhibits a much higher catalytic current density and lower overpotentials at a high current density (100 mA cm$^{-2}$) than Ir–C being loaded on Ni foam and Co–Se4 (**Figure 3**a). The OER current density of Co–Se1 increases dramatically beyond 1.49 V (vs RHE). A 100 mA cm$^{-2}$ current density is achieved at an overpotential of 280 mV ($\eta$ = 280 mV), which is lower than those for Ir–C (370 mV) and Co–Se4 (410 mV). The details for calculation of overpotential are described in the Supporting Information. A comparative summary of the electrocatalytic activity of state-of-the-art OER catalysts in recent reports is presented in Table S1 in the Supporting Information. It is very interesting to note that Co–Se1 demonstrates favorable electrocatalytic activity with most active non-noble metal based electrocatalysts, such as Cu@CoS$_x$/CF (210 mV),[37] CuCoO-NWs (340 mV),[34] Ni$_3$C/C (390 mV),[38] and Ni$_3$FeN-NPs (415 mV),[39] with overpotential of 280 mV at a great current density of 100 mA cm$^{-2}$, indicating potential practical value of this catalyst.

The OER kinetics was assessed by Tafel plots [$\eta$ vs log ($j$)] derived from LSV curves for these electrodes. Figure 3b presents that the Tafel slop for Co–Se1 catalyst is 40.4 mV dec$^{-1}$, which is lower than those of Ir–C on Ni foam (74.9 mV dec$^{-1}$) and Co–Se4 (70.9 mV dec$^{-1}$), indicating a favorable OER kinetics for the Co–Se1 electrode. The electrochemical OER in alkaline electrolyte is initialized by OH$^-$ electrosorption on the active sites of the catalyst. These results reveal that the catalyst with a favorable affinity for OH$^-$ intermediates can promote their formation and equilibrium coverage. Hence subsequent step to evolve oxygen will become rate-determining, leading to a lower Tafel slope.[5] Correspondingly, the reduced Tafel slope for Co–Se1 compared with Ir–C and Co–Se4 indicates an efficient OER process coinciding with higher current density for Co–Se1 relative to Ir–C and Co–Se4 in the high potential range.

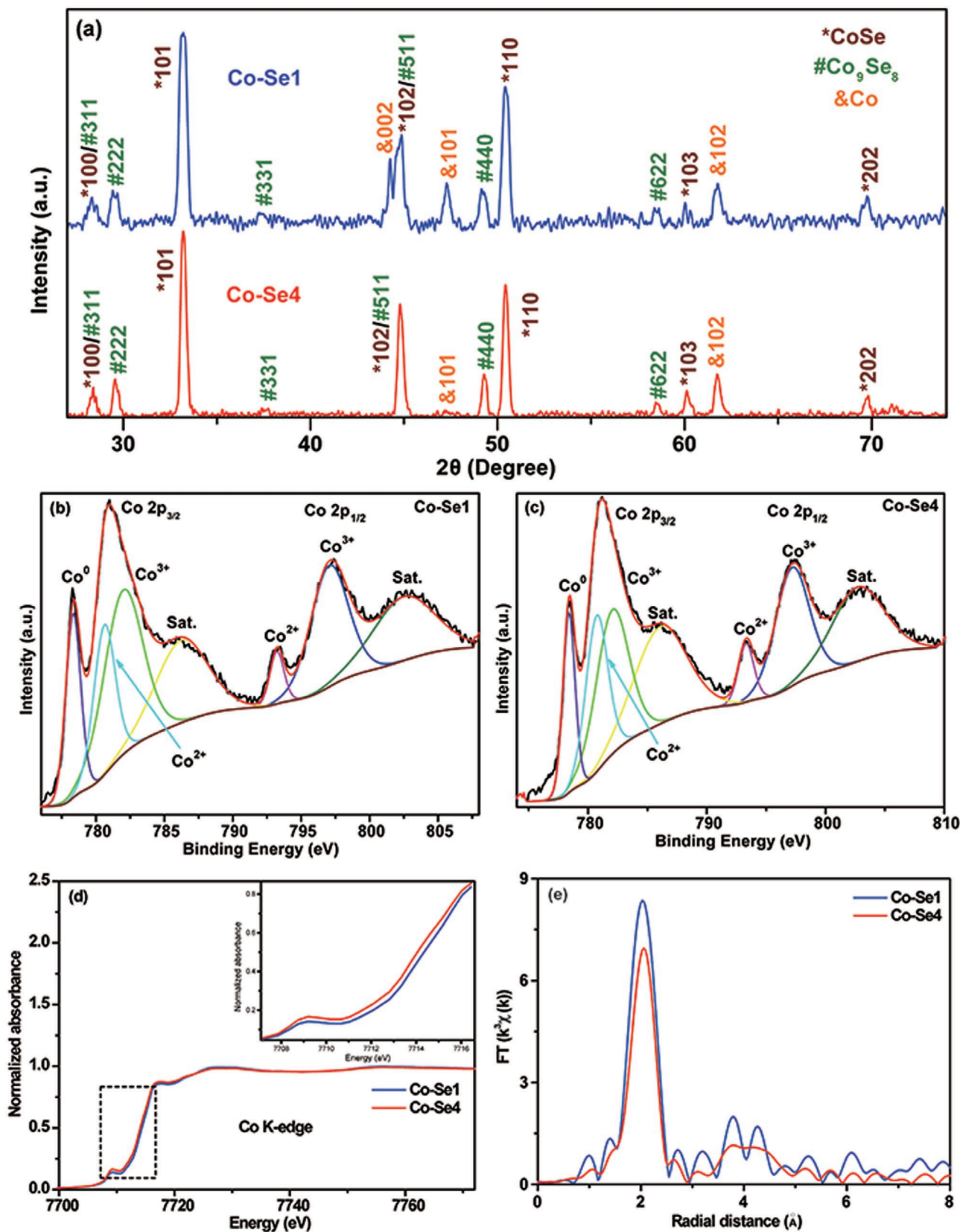Durability in alkaline electrolyte at a high concentration is one of the key features to evaluate the performance of

**ADVANCED
SCIENCE NEWS**

www.advancedsciencenews.com

**ADVANCED
ENERGY
MATERIALS**

www.advenergymat.de

**Figure 2.** a) XRD patterns for Co–Se1 and Co–Se4, b) XPS spectra of Co 2p for Co–Se1, c) XPS spectra of Co 2p for Co–Se4; d) synchrotron-based Co K-edge XANES spectra and (insert) enlarged preedge spectra for Co–Se1 and Co–Se4, and e) Fourier transformed k3—weighted EXAFS spectra for Co–Se1 and Co–Se4.
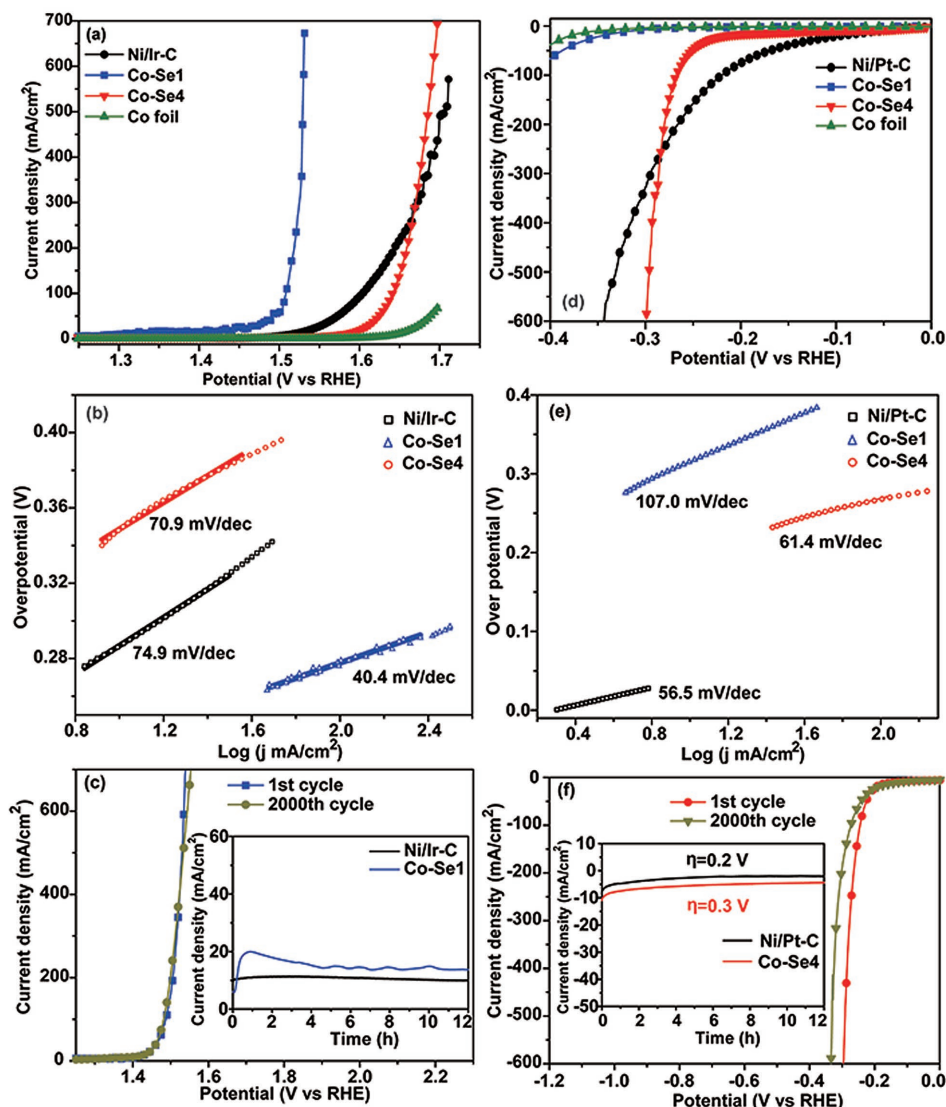
**Figure 3.** a) OER performance of Ni/Ir–C, Co–Se1, Co–Se4, and Co foil in 1.0 M KOH; b) corresponding Tafel plots with associated linear fittings; c) cycle stability of Co–Se1 and (inset) time dependence of current density under a constant potential of 1.57 V (vs RHE) of Ni/Ir–C and Co–Se1 in 1.0 M KOH; d) HER performance of Ni/Pt–C, Co–Se1, Co–Se4, and Co foil in 1.0 M KOH; e) corresponding Tafel plots with associated liner fittings; f) cycle stability of Co–Se4 and (inset) time dependence of current density under constant potentials of Ni/Pt–-C and Co–Se4 in 1.0 M KOH.

catalysts in practical application. In this work, cycle stability measurement of Co–Se1 was implemented in alkaline media (Figure 3c). After a long-term test with 2000 cycles, no obvious degradation is observed for Co–Se1. Furthermore, the long-term electrochemical stability of Ir–C on Ni foam and Co–Se1 in 1.0 M KOH for bulk electrolysis was measured at a constant overpotential of 1.57 V (vs RHE). As demonstrated in inset of Figure 3c, Co–Se1 exhibits stable current density during 12 h continuous operation. The current density of Co–Se1 is higher than that of Ni/Ir–C under the same overpotential. Interestingly, Co–Se1 shows an enhanced electrocatalytic activity in the first hour, which is commonly found in transition metal based electrocatalysts. The enhanced electrocatalytic activity can be attributed to the increased active electrocatalytic species enabling in alkaline solution.[33] An activation process could occur

in the first hour for stability measurement with the conversion of surface cobalt selenide to OER active cobalt hydroxide species (Figures S3 and S4, Supporting Information). In addition, the self-growth merit endows Co–Se1 electrode with 3D network structure, which is favorable for $O_2$ release and long-term duality. Strong connection between catalytic cobalt selenide and Co substrate could also be beneficial for enhancing their exceptional OER stability.

The HER operation is significant to pursue bifunctional water electrolysis electrode and to simplify the processing installation. Hence, the catalytic capacity of the cobalt selenide electrodes to HER was evaluated in the identical electrolyte to OER. The electrochemically catalyzed HER on Co–Se1 and Co–Se4 catalyst electrodes were evaluated in Ar-saturated 1.0 M KOH electrolyte at a scan rate of 5 mV s$^{-1}$ in a typical three-electrode cell. Bare
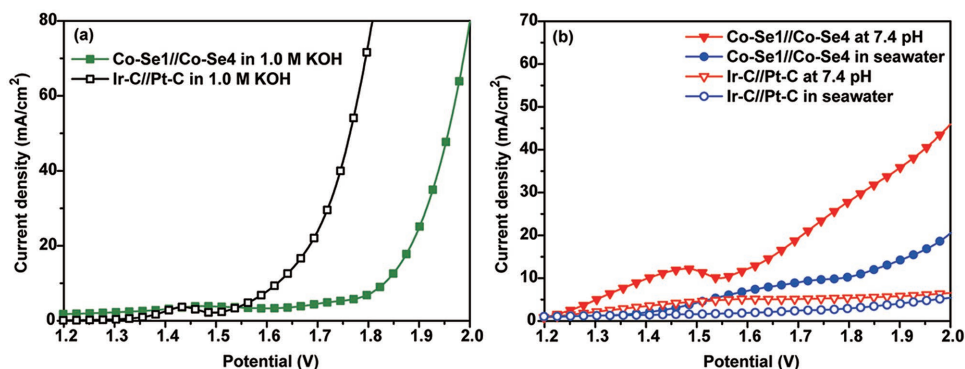
**Figure 4.** Polarization curves of Co–Se1//Co–Se4 and Ir–C//Pt–C in a) 1.0 M KOH and b) buffer solution and seawater at a scan rate of 5 mV s$^{-1}$.

cobalt foil and Pt–C loaded on Ni foam were also selected for comparison. The LSV curves of the Ni/Pt–C, Co–Se1, Co–Se4, and Co foil electrodes are illustrated in Figure 3d. Co–Se4 displays a much higher catalytic current density than Pt–C on Ni foam and Co–Se1. The HER current density of Co–Se4 exhibits a dramatic increase beyond −0.25 V (vs RHE). A 100 mA cm$^{-2}$ current density is realized at an overpotential of 268 mV for Co–Se4, which is lower than that for Co–Se1 (416 mV) and comparable with that for Pt–C (221 mV). A comparative summary of the HER electrocatalytic performance of state-of-the-art catalysts in recently reported works is presented in Table S2 in the Supporting Information. It is seen that the electrocatalytic performance of Co–Se4 compares favorably with that of the most active non-noble metal based electrocatalysts, such as Ni$_3$FeN-NPs (320 mV),[39] NiMoP$_2$/CC (330 mV),[40] Ni$_3$S$_2$/Ni (440 mV),[41] and CoP/CC (505 mV),[42] with overpotential of 268 mV at a great current density of 100 mA cm$^{-2}$, suggesting that Co–Se4 practically acts as a high-efficient HER electrocatalyst.

Figure 3e shows the Tafel plots of Co–Se1, Co–Se4, and Ni/Pt C catalytic electrodes for HER operation. The measured Tafel slope of Pt–C on Ni foam is about 56.5 mV dec$^{-1}$, which is consistent with reported values.[43] The Tafel slop for Co–Se4 catalyst is 61.4 mV dec$^{-1}$, which is comparable with that of Pt–C and is smaller than that of Co–Se1 (107.9 mV dec$^{-1}$), indicating a favorable HER kinetics for the Co–Se4 electrode. Furthermore, the slopes of Co–Se1 and Co–Se4 fall within the range of 40–120 mV dec$^{-1}$, indicating that the HER on their surfaces might have proceeded via Volmer–Heyrovsky mechanism.[44] HER kinetics with electrocatalytic activity was further analyzed through electrochemical impedance spectroscopy (EIS) investigations (Figure S5, Supporting Information). The Nyquist plots of both Co–Se1 and Co–Se4 catalysts display a semicircle in the low-frequency range (an indicator of charge transfer resistance of the catalysts). The calculated resistance of the Co–Se4 catalyst (56.7 Ω) is significantly lower than that of the Co–Se1 (107.5 Ω), indicating more rapid charge transfer within the Co–Se4 catalyst which is possibly associated with higher HER catalytic activity. Figure 3f shows that Co–Se4 displays stable electrocatalytic performance after 2000 HER cycles. Furthermore, the catalytic stability of Co–Se4 for HER was evaluated by continuous chronoamperometric response in 1.0 M KOH at a constant potential of −0.30 V (vs RHE). The resulting time-dependent current density curve is illustrated in inset of Figure 3f. Co–Se4 exhibits stable HER electrocatalytic

performance with negligible degradation of current density during 12 h, which is comparable with that for Pt–C. In a similar vein, the self-growth merit and 3D network could be responsible for its excellent stability during HER process.

Based on current studies, it can be reasonably anticipated that as-prepared cobalt selenides act as highly efficient and stable bifunctional catalysts for OER and HER. Therefore, two electrode electrolyzers in 1.0 M KOH (Figure S6, Supporting Information), buffer solution (pH = 7.4) and seawater were established with integration of Co–Se1 and Co–Se4 catalytic electrodes as the anode and cathode of overall water electrolysis (denoted as Co–Se1//Co–Se4), respectively. Ir–C and Pt–C loaded on Ni foam denoted as Ir–C//Pt–C were also determined for comparison. **Figure 4** presents the LSV curves of the Co–Se1//Co–Se4 and Ir–C//Pt–C in overall water splitting system at a scan rate of 5 mV s$^{-1}$. Although the electrocatalytic performance of Ir–C//Pt–C in 1.0 M KOH electrolyte exceeds that of Co–Se1//Co–Se4 (Figure 4a), Co–Se1//Co–Se4 system exhibits better electrocatalytic activity in buffer solution and seawater (Figure 4b). The current density achieved at a potential of 1.8 V for Co–Se1//Co–Se4 is 10.3 mA cm$^{-2}$, higher than that for Ir–C//Pt–C (2.9 mA cm$^{-2}$). This is probably attributed to rapid charge transfer and 3D network with lacunose surface benefiting for ion and gas transportation.[45] The OER and HER activities of Co–Se1 and Co–Se4 in seawater were also assessed (Figure S7, Supporting Information). Notably, electrocatalytic activity of Co–Se1//Co–Se4 in seawater compares favorably with that of the most active non-noble metal based electrocatalysts, such as PtRuMo[20] and MHCM-z-BCC/NiMoS.[21] The duality of Co–Se1//Co–Se4 electrolyzer in 1.0 M KOH was evaluated at a constant potential of 1.95 V (Figure S8, Supporting Information). Co–Se1//Co–Se4 system exhibits stable current density during 12 h continuous operation. Interestingly, Co–Se1//Co–Se4 system shows enhanced electrocatalytic activity in the first hour, which is attributed to an activation process happening to Co–Se1 electrode with the conversion of surface cobalt selenide to OER active cobalt hydroxide species (Figures S3 and S4, Supporting Information) in alkaline solution.[33]

### 2.3. Catalytic Mechanism

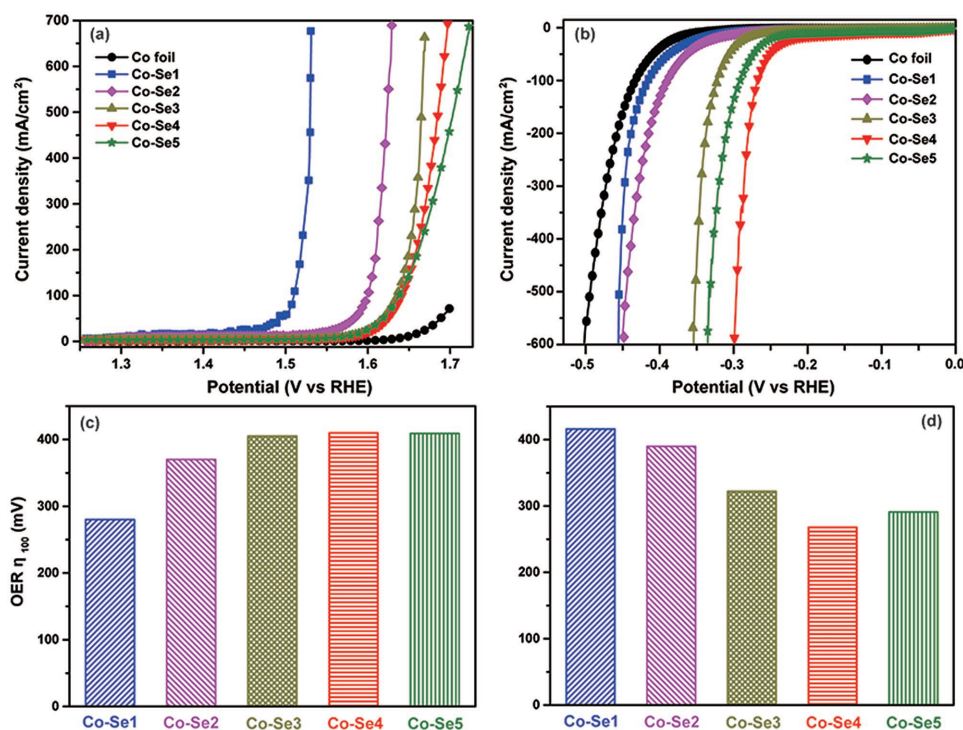Catalytic mechanism of the electrocatalyst electrodes was studied using a serious of cobalt selenide electrodes (i.e.,

ADVANCED
SCIENCE NEWS
www.advancedsciencenews.com

ADVANCED
ENERGY
MATERIALS
www.advenergymat.de

**Figure 5.** a) OER and b) HER performance of Co foil, Co–Se1, Co–Se2, Co–Se3, Co–Se4, and Co–Se5 in 1.0 M KOH at a scan rate of 5 mV s$^{-1}$; overpotentials of as-prepared cobalt selenide for achieving the current density of 100 mA cm$^{-2}$ for c) OER and d) HER operation.

Co–Se1, Co–Se2, Co–Se3, Co–Se4, and Co–Se5). Their electrocatalytic OER and HER performances in 1.0 M KOH were systematically studied. **Figure 5**a,c presents the electrocatalytic performance for OER operation deteriorates with increasing Co:Se mass ratio. Overpotentials of the cobalt selenide electrodes for achieving the current density of 100 mA cm$^{-2}$ for OER operation increases from Co–Se1 to Co–Se3 and remains unchanged from Co–Se3 to Co–Se5. It is worthwhile to note that the electrocatalytic performance for HER operation demonstrates opposite tendency compared with that for OER (Figure 5b,d). The electrocatalytic performance for HER operation deteriorates from Co–Se4 to Co–Se5 with further increasing Co:Se mass ratio.

It has been reported that introducing more highly oxidized metal species in electrocatalysts would promote oxidation reactions.[46] Metal cations are oxidized to higher charge states in OER before the onset of the reaction. These highly oxidative metal cations are supposed as electrocatalytic active sites.[47] For example, it was revealed that enhanced oxidation of cobalt oxide by a metal support could improve OER activity.[30] XPS analysis results (Figure 2b,c) confirm that Co–Se1 exhibits higher relative mole ratio of Co$^{3+}$/Co$^{2+}$ (0.22:1) than Co–Se4 (0.15:1), indicating higher charge states of Co species for Co–Se1. This finding corresponds well with the results obtained from synchrotron-based XANES (Figure 2d). These highly oxidized Co species are able to enhance OER activity of the electrocatalyst. This can be clarified by the widely accepted five-step OER mechanism for transition metal electrocatalysts. [(1) * + OH$^-$ → *OH + e$^-$; (2) *OH + OH$^-$ → H$_2$O + *O + e$^-$; (3) *O + OH$^-$ → *OOH + e$^-$; (4) *OOH + OH$^-$ → *O$_2$ + e$^-$; (5) *O$_2$ → * + O$_2$].[48]

It was reported that the third step involved in the formation of (*OOH) intermediate is the key in OER.[5,49] The higher charge state of Co can assist electrostatic adsorption of OH$^-$ ions, and reduce the energy barrier of Co transition from a lower- to a higher- charge state in the selenides promoting electrocatalytic OER. It was also revealed that Co$^{3+}$ centers in electrocatalysts can be oxidized to Co$^{4+}$ under anodic bias, and these Co$^{4+}$ centers oxidize water to oxygen.[50] Moreover, the localized negative charges on negatively-charged Se active centers (Se$^{\delta-}$) can deactivate electrocatalysts from coordinating with the hydroxide ligand as a result of the increased 3p–2p repulsion between Co and Se.[23] This may considerably increase the overpotential for OER. As a result, Co–Se1 with higher Co$^{3+}$ and lower Se$^{\delta-}$ species exhibits a much greater catalytic current density, lower overpotential at 100 mA cm$^{-2}$, and lower Tafel slope than Co–Se4 for OER operation.

Interestingly, Co–Se4 with lower relative mole ratio of Co$^{3+}$/Co$^{2+}$ exhibits increased electrocatalytic performance for HER. This can be attributed to rapid charge transfer based on analyses of the EIS results (Figure S5, Supporting Information). The corresponding double layer capacitances were also measured to compare the electrochemical surface areas of Co–Se1 and Co–Se4. The Co–Se4 has a significantly larger electrochemical surface area than Co–Se1 (Figures S9, Supporting Information). The high electrocatalytic activity of the Co–Se4 electrocatalyst for the HER can also be ascribed to less positively-charged Co species and consequent more Se$^{\delta-}$.[23] XPS and XANES spectra reveal that Co–Se4 electrodes with lower relative mole ration of Co$^{3+}$/Co$^{2+}$ possess more Se$^{\delta-}$. The HER process of the prepared cobalt selenides electrodes could

be carried out through a Volmer ($H_2O + e^- \rightarrow H^* + OH^-$) – Heyrovsky ($H_2O + e^- + H^* \rightarrow H_2 + OH^-$) pathway in alkaline media. Such pathway includes adsorption of $H_2O$ and the electrochemical decomposition of trapped $H_2O$ into adsorbed $H^*$ and $OH^-$ species, followed by detachment of $OH^-$ and formation of $H^*$ to obtain $H_2$. The $H^*$ species generated by Volmer step would preferentially attach to $Se^{\delta-}$. The polarization-induced partial negative charges localized on E (E = P, S, and Se) centers with E-terminated surface can significantly enhance adsorption and discharge of $H^*$, and promote the HER.[23,51] This can be attributed to moderate strength of Se–H bond (276 kJ mol$^{-1}$). Consequently, Co–Se4 with moderate number of $Se^{\delta-}$ centers exhibits best electrocatalytic performance for HER among all cobalt selenides electrodes.

## 3. Conclusion

A facile and scalable method for fabrication of new 3D cobalt selenide electrodes with novel CoSe and $Co_9Se_8$ phases was developed. The charge state of Co species and electrocatalytic performance of the prepared cobalt selenide catalysts were manipulated by controlling mass ratio of raw materials and calcining in vacuum-sealed ampoule at high temperature. Resultant 3D network, exposed electrocatalytic centers, and rapid charge transfer capability are responsible for highly active and stable OER and HER electrocatalytic activity of these novel electrodes. These merits resulted in excellent overall seawater splitting performance. This work will shed a light on development of cobalt selenide electrocatalysts and uncover new horizons for research of clean energy systems.

## 4. Experimental Section

*Fabrication of Cobalt Selenide Electrodes*: The cobalt selenide electrodes were fabricated by a facile one-step selenization of Co (Sigma-Aldrich, USA, 99.95% trace metals basis, foil, thickness 0.1 mm) with Se (Sigma-Aldrich, Canada, ≥99.95% trace metals basis, powder, −100 mesh) in a vacuum sealed ampoule. In a typical synthesis, a Co foil (70.29 mg, 1.8 cm × 0.3 cm × 0.01 cm, length × width × height) was cleaned with alcohol, acetone, 1.0 M HCl and Milli-Q water for 5 min in sequence. The Co foil and Se powder were sealed in ampoule under vacuum and then calcinated at 550 °C for 5 h. Heating rate was 5 °C min$^{-1}$ and the cooling process took place naturally. A variety of Co to Se mass ratio, i.e., 1:0.02, 1:0.037, 1:0.085, 1:0.142, and 1:0.2, was employed. In the order of small to large in Co to Se mass ratio, the as-prepared cobalt selenide electrodes were denoted as Co–Se1, Co–Se2, Co–Se3, Co–Se4, and Co–Se5, respectively. The loading of electrocatalyst materials for Co–Se1 and Co–Se4 are around 2.6 and 18.2 mg, respectively.

*Fabrication of Pt–C and Ir–C Loaded Electrodes*: 4 mg Pt–C or Ir–C were dispersed in 1 mL water, followed by sonication for 30 min to obtain a homogeneous catalyst ink. 150 µL catalyst ink and 40 µL 2% Nifion solution were loaded on the surface of Ni foam (surface area: 0.6 cm$^2$) in succession. The overall loading amount is 1 mg cm$^{-2}$.

*Electrochemical Characterization*: The HER, OER, and overall water splitting measurements were performed in a three-electrode glass cell. The data were recorded using a CHI 760 D bipotentiostat (CH Instruments, Inc., USA). The as-prepared electrodes were directly used as the working electrode for electrochemical characterizations. The reference electrode was Ag/AgCl in 4.0 M KCl solution and the

counter electrode was a carbon electrode. The phosphate buffer solution (Sigma-Aldrich, USA, 1.0 M, pH = 7.4) was used for overall water electrolysis in neutral media. To investigate the performance of the systems in seawater, neutral-buffered seawater electrolyte was prepared. Natural seawater was collected from Glenelg beach in Adelaide, Australia, and was applied directly without further purification. The neutral-buffered seawater electrolyte was prepared by mixing phosphate buffer solution with natural seawater, and the pH of the mixed electrolyte was adjusted to 7.09. The current density was normalized to the geometrical surface area and the measured potentials versus Ag/AgCl were converted to a reversible hydrogen electrode (RHE) scale according to the Nernst equation

$$E_{RHE} = E_{Ag/AgCl} + 0.059 \times pH + 0.205 \tag{1}$$

A flow of Ar was maintained over the electrolyte during electrochemical measurements. The polarization curves were recorded in the range of 1.0–1.8 V versus RHE for OER and −0.6 to 0 V versus RHE for HER at a slow scan rate of 5 mV s$^{-1}$ to minimize the capacitive current. The working electrodes were scanned for several times until the signals were stabilized, and then the data for polarization curves were collected and corrected for the iR contribution within the cell. The long time durability test was conducted by using controlled-potential electrolysis method without iR compensation. The EIS was obtained by AC impedance spectroscopy within the frequency range from 10 to 100 kHz in 1.0 M KOH. The equivalent circuit for fitting of the EIS data was achieved with ZView software. The Tafel slope was calculated according to Tafel equation as follows

$$\eta = b\log(j/j_0) \tag{2}$$

where $\eta$ denotes the overpotential, $b$ denotes the Tafel slope, $j$ denotes the current density, and $j_0$ denotes the exchange current density. The onset potentials were determined based on the beginning of the linear region in Tafel plots. The overpotential was calculated as follows

$$\eta = E(vs\,RHE) - E_r(vs\,RHE) \tag{3}$$

where $E$ denotes the actual applied potential and $E_r$ denotes the reversible potential of the reaction. $E_r$ is 1.23 V versus RHE for OER and 0 V versus RHE for HER. And HER $\eta$ is always negative. The electrochemical surface area of the electrodes was related to double-layer charging curves using cyclic voltammetry in a potential range (0.1–0.2 V vs SCE). The double-layer capacitance values were determined from the slope of the capacitive current versus scan rate.

## Supporting Information

Supporting Information is available from the Wiley Online Library or from the author.

## Acknowledgements

## Conflict of Interest

The authors declare no conflict of interest.

**ADVANCED
SCIENCE NEWS**

www.advancedsciencenews.com

**ADVANCED
ENERGY
MATERIALS**

www.advenergymat.de

[1] I. Roger, M. A. Shipman, M. D. Symes, *Nat. Rev. Chem.* **2017**, *1*, 0003.

[2] L. Han, S. Dong, E. Wang, *Adv. Mater.* **2016**, *28*, 9266.

[3] Y. Yan, B. Y. Xia, B. Zhao, X. Wang, *J. Mater. Chem. A* **2016**, *4*, 17587.

[4] H. Jin, C. Guo, X. Liu, J. Liu, A. Vasileff, Y. Jiao, Y. Zheng, S. Z. Qiao, *Chem. Rev.* **2018**, *118*, 6337.

[5] Y. Jiao, Y. Zheng, M. Jaroniec, S. Z. Qiao, *Chem. Soc. Rev.* **2015**, *44*, 2060.

[6] J. Wang, W. Cui, Q. Liu, Z. Xing, A. M. Asiri, X. Sun, *Adv. Mater.* **2016**, *28*, 215.

[7] J. Jae-Il, J. H. Young, L. Jang Soo, K. M. Gyu, C. Jaephil, *Angew. Chem., Int. Ed.* **2014**, *53*, 4582.

[8] J. G. Lee, J. Hwang, H. J. Hwang, O. S. Jeon, J. Jang, O. Kwon, Y. Lee, B. Han, Y. G. Shul, *J. Am. Chem. Soc.* **2016**, *138*, 3541.

[9] C. G. Morales-Guio, L. Liardet, X. Hu, *J. Am. Chem. Soc.* **2016**, *138*, 8946.

[10] R. Liu, Y. Wang, D. Liu, Y. Zou, S. Wang, *Adv. Mater.* **2017**, *29*, 1701546.

[11] B. Zhang, X. Zheng, O. Voznyy, R. Comin, M. Bajdich, M. García-Melchor, L. Han, J. Xu, M. Liu, L. Zheng, F. P. García de Arquer, C. T. Dinh, F. Fan, M. Yuan, E. Yassitepe, N. Chen, T. Regier, P. Liu, Y. Li, P. De Luna, A. Janmohamed, H. L. Xin, H. Yang, A. Vojvodic, E. H. Sargent, *Science* **2016**, *352*, 333.

[12] M. Justus, W. Philipp, S. Daniel, S. Ilya, X. Wei, S. Zhenyu, S. Christoph, M. Martin, S. Wolfgang, *Adv. Energy Mater.* **2016**, *6*, 1502313.

[13] H. Park, A. Encinas, J. P. Scheifers, Y. Zhang, B. P. T. Fokwa, *Angew. Chem., Int. Ed.* **2017**, *56*, 5575.

[14] P. Xiao, X. Ge, H. Wang, Z. Liu, A. Fisher, X. Wang, *Adv. Funct. Mater.* **2015**, *25*, 1520.

[15] S. Wang, J. Wang, M. Zhu, X. Bao, B. Xiao, D. Su, H. Li, Y. Wang, *J. Am. Chem. Soc.* **2015**, *137*, 15753.

[16] H. Yan, C. Tian, L. Wang, A. Wu, M. Meng, L. Zhao, H. Fu, *Angew. Chem., Int. Ed.* **2015**, *54*, 6325.

[17] T. Liu, D. Liu, F. Qu, D. Wang, L. Zhang, R. Ge, S. Hao, Y. Ma, G. Du, A. M. Asiri, L. Chen, X. Sun, *Adv. Energy Mater.* **2017**, *7*, 1700020.

[18] Y. Yang, K. Zhang, H. Lin, X. Li, H. C. Chan, L. Yang, Q. Gao, *ACS Catal.* **2017**, *7*, 2357.

[19] Y. Hou, M. R. Lohe, J. Zhang, S. Liu, X. Zhuang, X. Feng, *Energy Environ. Sci.* **2016**, *9*, 478.

[20] H. Li, Q. Tang, B. He, P. Yang, *J. Mater. Chem. A* **2016**, *4*, 6513.

[21] S. H. Hsu, J. Miao, L. Zhang, J. Gao, H. Wang, H. Tao, S. F. Hung, A. Vasileff, S. Z. Qiao, B. Liu, *Adv. Mater.* **2018**, *0*, 1707261.

[22] D. Kong, H. Wang, Z. Lu, Y. Cui, *J. Am. Chem. Soc.* **2014**, *136*, 4897.

[23] S. Anantharaj, S. R. Ede, K. Sakthikumar, K. Karthick, S. Mishra, S. Kundu, *ACS Catal.* **2016**, *6*, 8069.

[24] Y. Liu, H. Cheng, M. Lyu, S. Fan, Q. Liu, W. Zhang, Y. Zhi, C. Wang, C. Xiao, S. Wei, B. Ye, Y. Xie, *J. Am. Chem. Soc.* **2014**, *136*, 15670.

[25] Y. Hou, M. Qiu, T. Zhang, X. Zhuang, C. S. Kim, C. Yuan, X. Feng, *Adv. Mater.* **2017**, *29*, 1701589.

[26] T. Liu, Q. Liu, A. M. Asiri, Y. Luo, X. Sun, *Chem. Commun.* **2015**, *51*, 16683.

[27] X. Xu, P. Du, Z. Chen, M. Huang, *J. Mater. Chem. A* **2016**, *4*, 10933.

[28] H. Zhou, Y. Wang, R. He, F. Yu, J. Sun, F. Wang, Y. Lan, Z. Ren, S. Chen, *Nano Energy* **2016**, *20*, 29.

[29] X. Li, L. Zhang, M. Huang, S. Wang, X. Li, H. Zhu, *J. Mater. Chem. A* **2016**, *4*, 14789.

[30] B. S. Yeo, A. T. Bell, *J. Am. Chem. Soc.* **2011**, *133*, 5587.

[31] H. Jin, J. Wang, D. Su, Z. Wei, Z. Pang, Y. Wang, *J. Am. Chem. Soc.* **2015**, *137*, 2688.

[32] J. J. Zhang, H. Su, H.-H. Wang, Z. H. Xue, B. Zhang, X. Wei, X. H. Li, S. I. Hirano, J.-S. Chen, *Nano Energy* **2017**, *39*, 321.

[33] W. Li, X. Gao, D. Xiong, F. Wei, W. G. Song, J. Xu, L. Liu, *Adv. Energy Mater.* **2017**, *7*, 1602579.

[34] M. Kuang, P. Han, Q. Wang, J. Li, G. Zheng, *Adv. Funct. Mater.* **2016**, *26*, 8555.

[35] X. Wang, Z. Chen, X. Zhao, T. Yao, W. Chen, R. You, C. Zhao, G. Wu, J. Wang, W. Huang, J. Yang, X. Hong, S. Wei, Y. Wu, Y. Li, *Angew. Chem., Int. Ed.* **2018**, *57*, 1944.

[36] T. Meng, J. Qin, S. Wang, D. Zhao, B. Mao, M. Cao, *J. Mater. Chem. A* **2017**, *5*, 7001.

[37] Y. Liu, Q. Li, R. Si, G. D. Li, W. Li, D. P. Liu, D. Wang, L. Sun, Y. Zhang, X. Zou, *Adv. Mater.* **2017**, *29*, 1606200.

[38] K. Xu, H. Ding, H. Lv, P. Chen, X. Lu, H. Cheng, T. Zhou, S. Liu, X. Wu, C. Wu, Y. Xie, *Adv. Mater.* **2016**, *28*, 3326.

[39] X. Jia, Y. Zhao, G. Chen, L. Shang, R. Shi, X. Kang, G. I. N. Waterhouse, L. Z. Wu, C. H. Tung, T. Zhang, *Adv. Energy Mater.* **2016**, *6*, 1502585.

[40] X. D. Wang, H. Y. Chen, Y. F. Xu, J. F. Liao, B. X. Chen, H. S. Rao, D. B. Kuang, C. Y. Su, *J. Mater. Chem. A* **2017**, *5*, 7191.

[41] L. L. Feng, G. Yu, Y. Wu, G. D. Li, H. Li, Y. Sun, T. Asefa, W. Chen, X. Zou, *J. Am. Chem. Soc.* **2015**, *137*, 14023.

[42] J. Tian, Q. Liu, A. M. Asiri, X. Sun, *J. Am. Chem. Soc.* **2014**, *136*, 7587.

[43] Z. Fang, L. Peng, Y. Qian, X. Zhang, Y. Xie, J. J. Cha, G. Yu, *J. Am. Chem. Soc.* **2018**, *140*, 5241.

[44] Z. Huang, Z. Chen, Z. Chen, C. Lv, M. G. Humphrey, C. Zhang, *Nano Energy* **2014**, *9*, 373.

[45] M. S. Faber, R. Dziedzic, M. A. Lukowski, N. S. Kaiser, Q. Ding, S. Jin, *J. Am. Chem. Soc.* **2014**, *136*, 10053.

[46] C. Guo, Y. Zheng, J. Ran, F. Xie, M. Jaroniec, S. Z. Qiao, *Angew. Chem., Int. Ed.* **2017**, *56*, 8539.

[47] L. Trotochaud, S. L. Young, J. K. Ranney, S. W. Boettcher, *J. Am. Chem. Soc.* **2014**, *136*, 6744.

[48] J. O. Bockris, T. Otagawa, *J. Phys. Chem.* **1983**, *87*, 2960.

[49] J. Rossmeisl, Z. W. Qu, H. Zhu, G. J. Kroes, J. K. Nørskov, *J. Electroanal. Chem.* **2007**, *607*, 83.

[50] J. G. McAlpin, Y. Surendranath, M. Dincă, T. A. Stich, S. A. Stoian, W. H. Casey, D. G. Nocera, R. D. Britt, *J. Am. Chem. Soc.* **2010**, *132*, 6882.

[51] Y. Shi, B. Zhang, *Chem. Soc. Rev.* **2016**, *45*, 1529.

**ADVANCED ENERGY MATERIALS**

# Supporting Information

## Charge State Manipulation of Cobalt Selenide Catalyst for Overall Seawater Electrolysis

*Yongqiang Zhao, Bo Jin, Yao Zheng, Huanyu Jin, Yan Jiao, and Shi-Zhang Qiao\**

Supporting Information

**Charge state manipulation of cobalt selenide catalyst for overall seawater electrolysis**

*Yongqiang Zhao, Bo Jin, Yao Zheng, Huanyu Jin, Yan Jiao, Shi-Zhang Qiao\**

Y. Q. Zhao, Prof. B. Jin, Dr. Y. Zheng, H. Jin, Dr. Y. Jiao, Prof. S. Z. Qiao

School of Chemical Engineering
The University of Adelaide
Adelaide, SA 5005, Australia
E-mail: s.qiao@adelaide.edu.au

Prof. S. Z. Qiao
School of Materials Science and Engineering
Tianjin University
Tianjin, 300072, China

## 1. Experimental

*Physicochemical Characterization:* Transmission electron microscopy (TEM) images and the selected area electron diffraction (SAED) patterns were obtained on a JEOL 2100F microscope at an acceleration voltage of 200 kV. High resolution TEM (HRTEM) images were obtained on an FEI Titan Themis 80-200 microscope at an acceleration voltage of 200 kV. Scanning electron microscopy (SEM) images were collected on the FEI Quanta 450 at high vacuum with an accelerating voltage of 30 kV. Elemental composition was recorder on the FEI Quanta 450 using a silicon drift detector energy-dispersive X-ray spectroscopy (SDD EDS). X-ray diffraction (XRD) patterns were collected on a powder X-ray diffractometer at 40 kV and 15 mA using Co-Kα radiation (Miniflex, Rigaku). X-ray photoelectron spectra (XPS) were obtained using an Axis Ultra (Kratos Analytical, UK) XPS spectrometer equipped with an Al Kα source (1486.6 eV). The synchrotron-based X-ray absorption near-edge structure (XANES) and extended X-ray absorption fine structure (EXAFS) measurements were conducted at the Shanghai Synchrotron Radiation Facility (SSRF).

1

**Figure S1.** SEM images and (inset) corresponding EDS of a) Co-Se1 and b) Co-Se4.
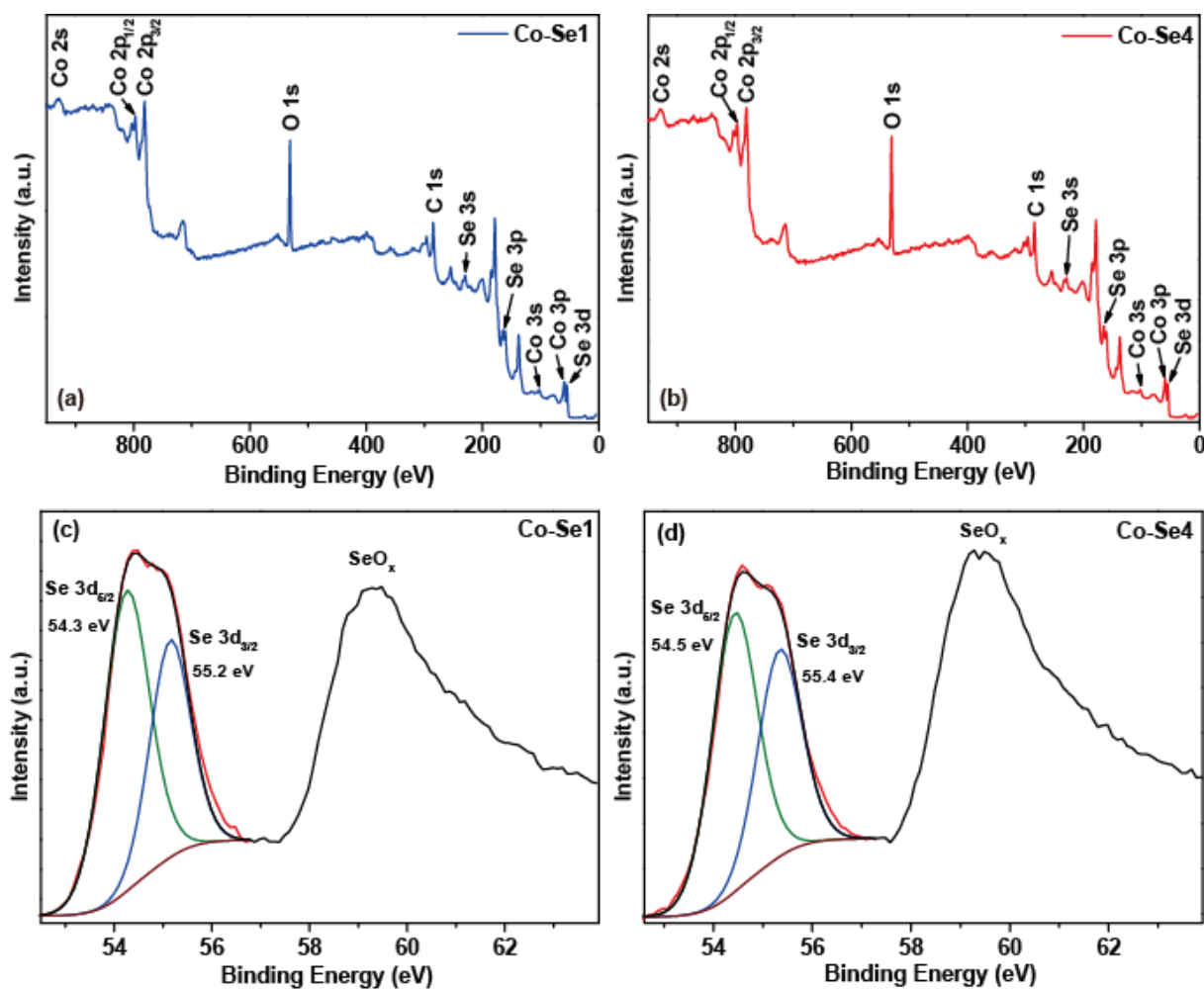


**Figure S2.** XPS survey spectra for a) Co-Se1 and b) Co-Se4; XPS spectra of Se 3d for c) Co-Se1 and d) Co-Se4.

**2. Supplementary Results**

2
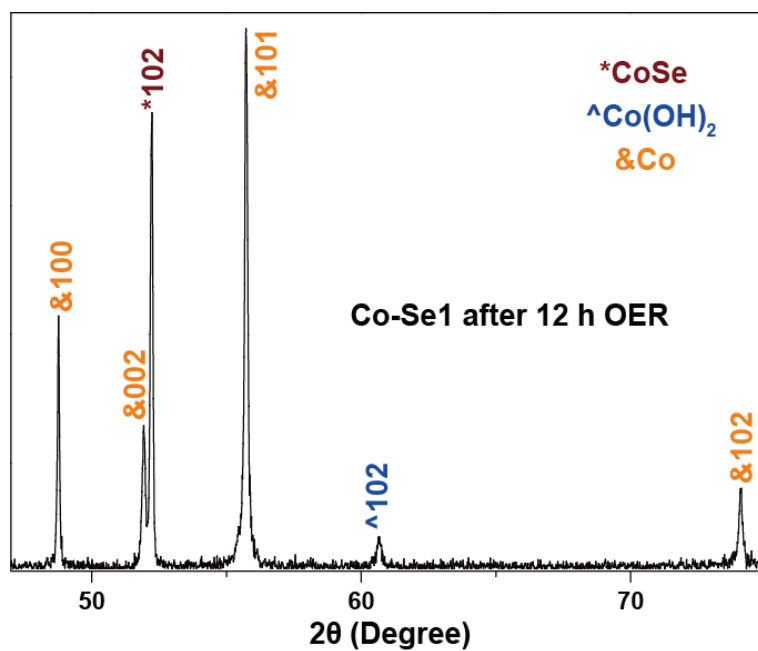
**Figure S3.** XRD patterns of Co-Se1 after 12 h continuous OER operation.
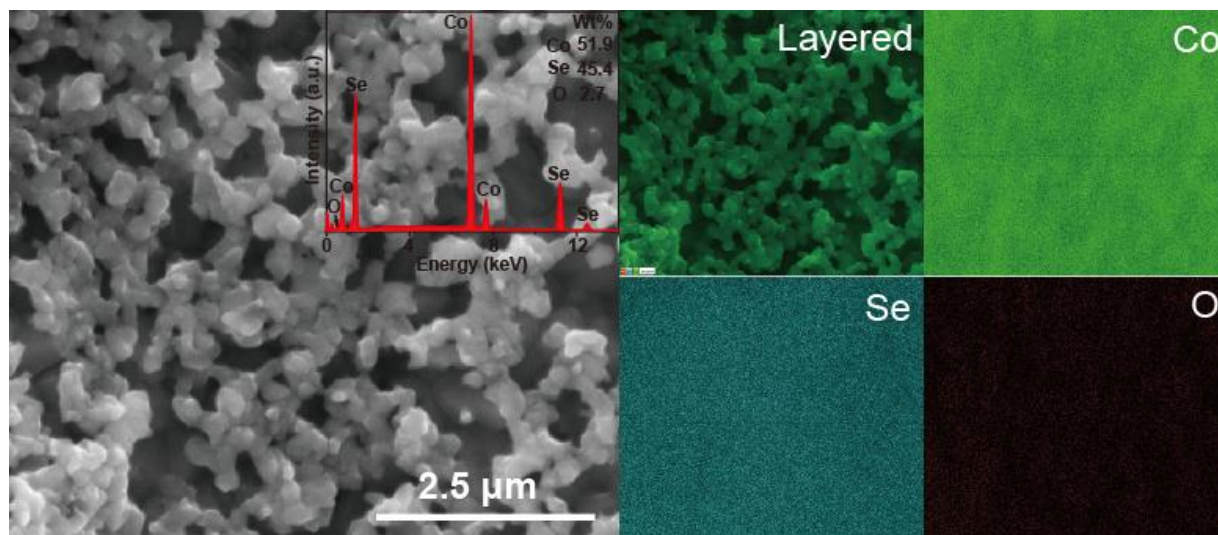


**Figure S4.** SEM image, (inset) corresponding EDS and SAED pattern of Co-Se1 after the OER in 1.0 M KOH.
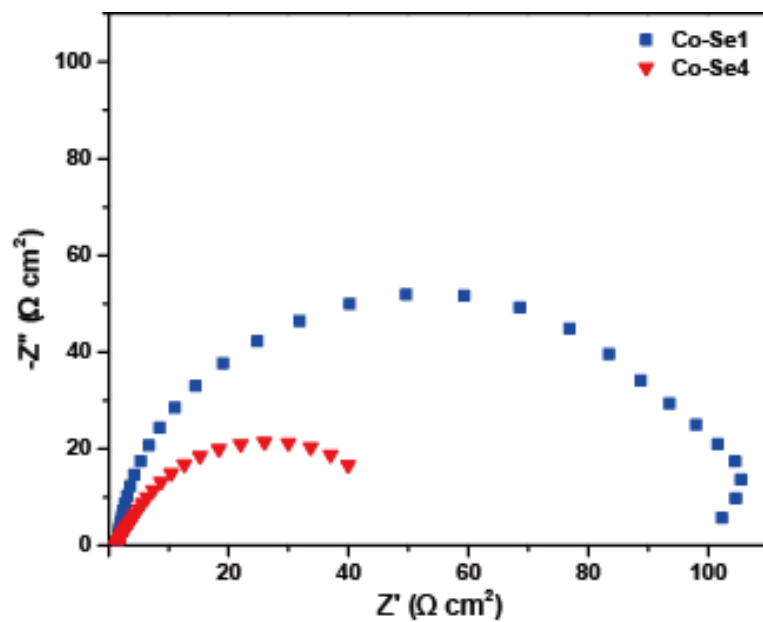
3

**Figure S5.** Nyquist plots of Co-Se1 and Co-Se4 electrodes in 1.0 M KOH with the potential of -0.214 V versus RHE.
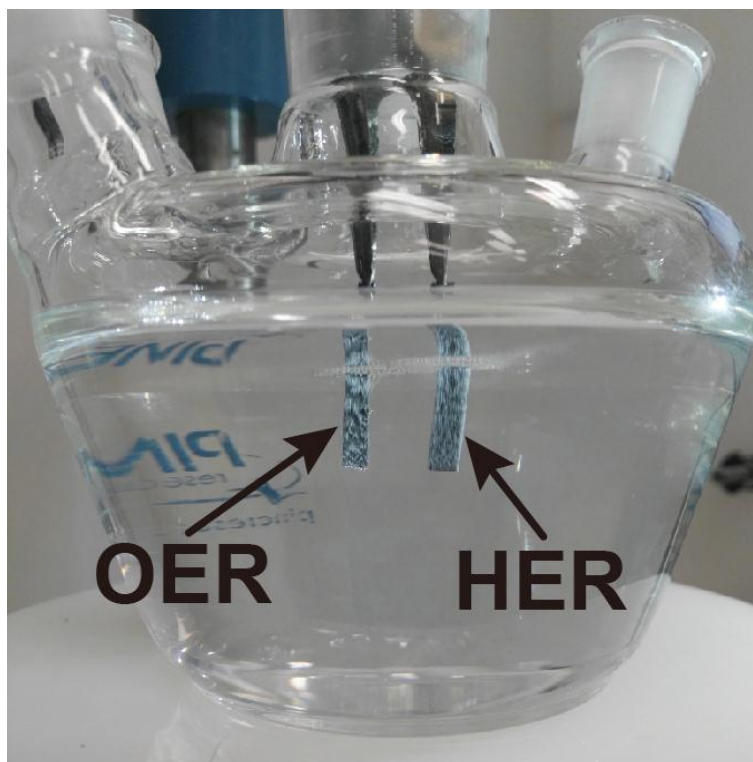


**Figure S6.** Digital photo of two electrodes electrolyzer in 1.0 M KOH.
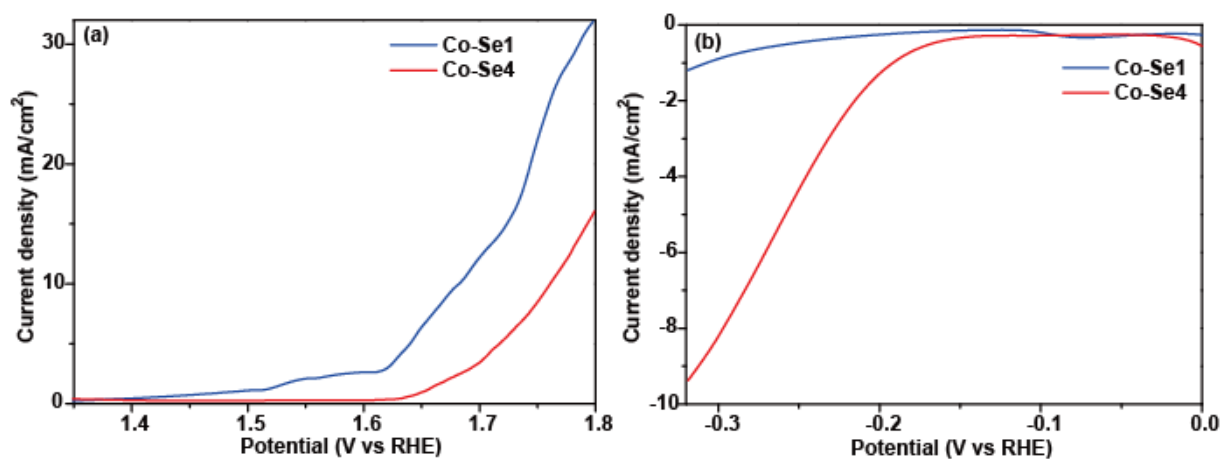
**Figure S7.** a) OER and b) HER performance of Co-Se1 and Co-Se4 in seawater at a scan rate of 5 mV/s.
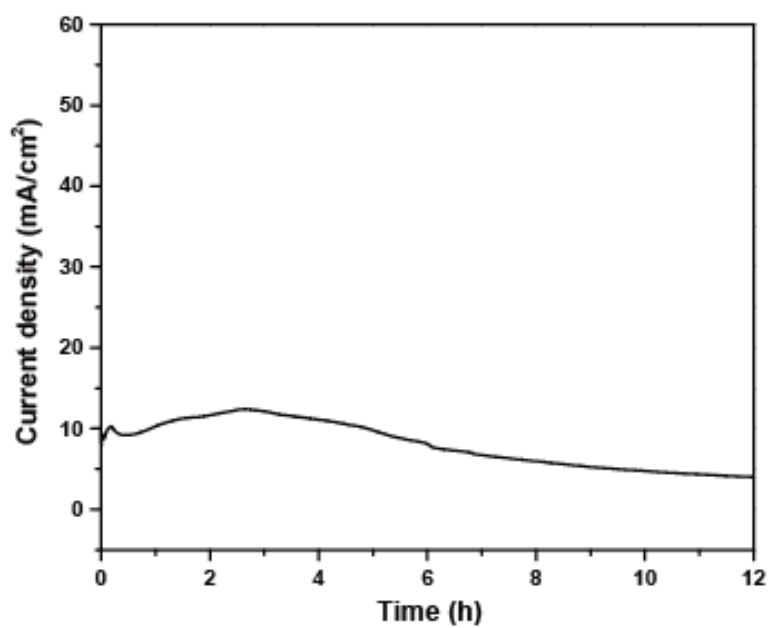


**Figure S8.** Time dependence of current density under a constant potential of 1.95 V of Co-Se1//Co-Se4 in 1.0 M KOH.

5
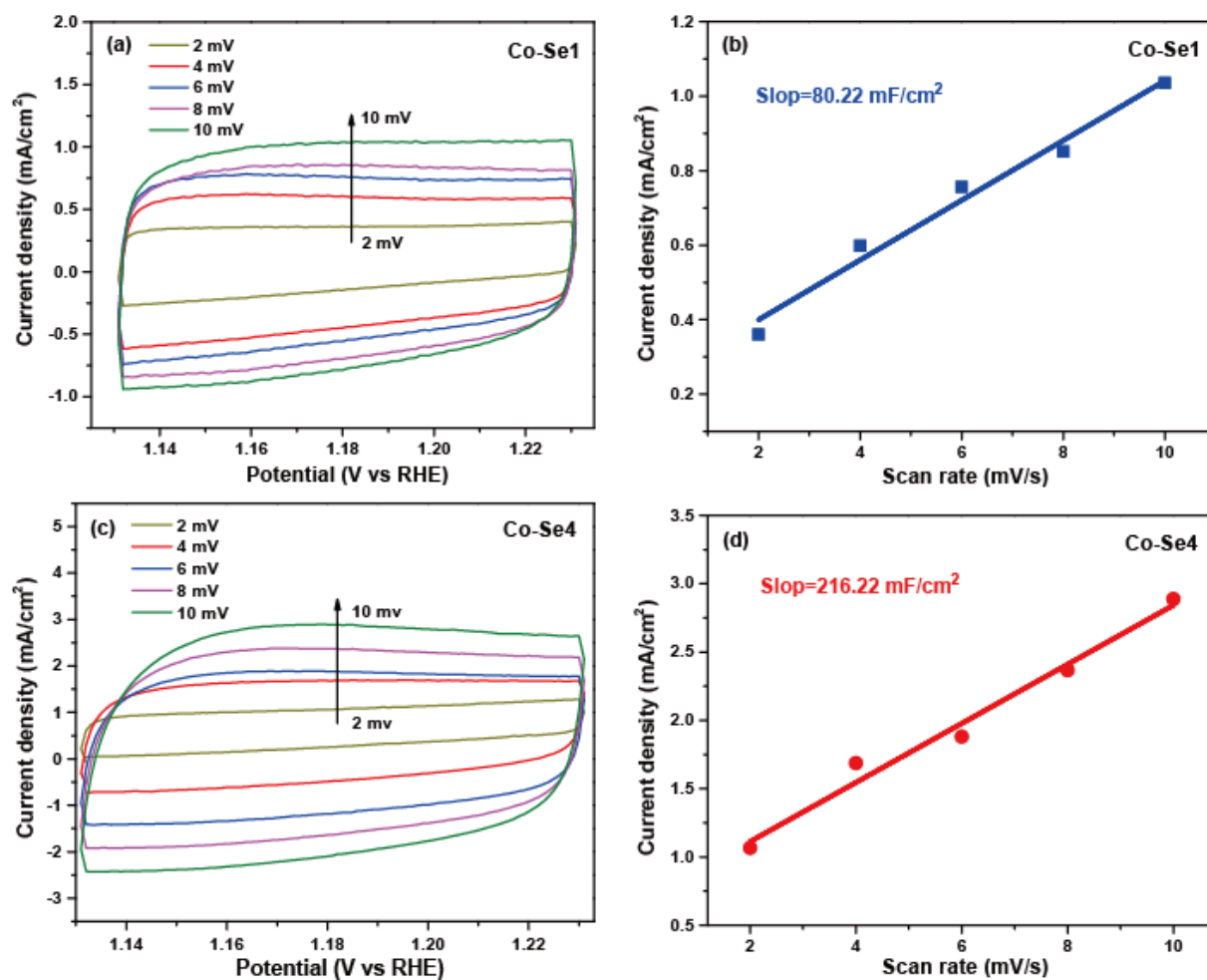
**Figure S9.** The double-layer region with scan rates ranging from 2 to 10 mV/s for a) Co-Se1 and c) Co-Se4; charging current density with different scan rates for b) Co-Se1 and d) Co-Se4.

6

**Table S1.** OER performance comparison between Co-Se1 and recently reported bifunctional catalysts in alkaline media.

| Catalysts | Electrolyte | j, mA/cm$^2$ | η required, mV | Tafel slope, mV/dec | Ref |
|---|---|---|---|---|---|
| Co-Se1 | 1.0 M KOH | 100 | 280 | 40.4 | This work |
| Cu@CoS$_x$/CF | 1.0 M KOH | 100 | ~210 | ----- | S1 |
| CuCoO-NWs | 1.0 M KOH | 100 | ~340 | 68 | S2 |
| Ni$_3$C/C | 1.0 M KOH | 100 | ~390 | 46 | S3 |
| Ni$_3$FeN-NPs | 1.0 M KOH | 100 | 415 | 46 | S4 |
| NiMoO$_4$ nanowires | 1.0 M KOH | 100 | ~460 | 40 | S5 |
| CoSe/Ti | 1.0 M KOH | 100 | ~360 | 69 | S6 |
| NiFe/NF | 1.0 M KOH | 100 | ~370 | 28 | S7 |
| ZnxCo$_{3-x}$O$_4$ nanoarrays | 1.0 M KOH | 100 | ~470 | 51 | S8 |
| LT-LiCoO$_2$ | 0.1 M KOH | 100 | 437 | 52 | S9 |
| NiMoO$_4$/CC | 1.0 M KOH | 100 | ~400 | 96.7 | S10 |

**Table S2.** HER performance comparison between Co-Se4 and recently reported bifunctional catalysts in alkaline media.

| Catalysts | Electrolyte | j, mA/cm$^2$ | η required, mV | Tafel slope, mV/dec | Ref |
|---|---|---|---|---|---|
| Co-Se4 | 1.0 M KOH | 100 | 268 | 61.4 | This work |
| Ni$_3$FeN-NPs | 1.0 M KOH | 100 | ~320 | 42 | S4 |
| NiMoP$_2$/CC | 0.5 M H$_2$SO$_4$ | 100 | ~330 | 56 | S10 |
| NixCo$_{3-x}$S$_4$/Ni$_3$S$_2$/NF | 1.0 M KOH | 100 | 258 | 95 | S11 |
| MoS$_2$/CoSe$_2$ | 0.5 M H$_2$SO$_4$ | 100 | ~240 | 36 | S12 |
| Ni$_3$S$_2$/Ni | 1.0 M KOH | 100 | ~440 | ----- | S13 |
| CoP/CC | 1.0 M KOH | 100 | ~505 | 129 | S14 |

**References**

[S1]  Y. Liu, Q. Li, R. Si, G. D. Li, W. Li, D. P. Liu, D. Wang, L. Sun, Y. Zhang, X. Zou, *Adv. Mater.* **2017**, 29, 1606200.

[S2]  M. Kuang, P. Han, Q. Wang, J. Li, G. Zheng, *Adv. Funct. Mater.* **2016**, 26, 8555.

[S3]  K. Xu, H. Ding, H. Lv, P. Chen, X. Lu, H. Cheng, T. Zhou, S. Liu, X. Wu, C. Wu, Y. Xie, *Adv. Mater.* **2016**, 28, 3326.

[S4]  X. Jia, Y. Zhao, G. Chen, L. Shang, R. Shi, X. Kang, G. I. N. Waterhouse, L. Z. Wu, C. H. Tung, T. Zhang, *Adv. Energy Mater.* **2016**, 6, 1502585.

[S5]  H. Liu, H. Li, P. He, X. Wang, *Small* **2016**, 12, 1006.

[S6]  T. Liu, Q. Liu, A. M. Asiri, Y. Luo, X. Sun, *Chem. Commun.* **2015**, 51, 16683.

[S7]  X. Lu, C. Zhao, *Nat. Commun.* **2015**, 6, 6616.

[S8]  X. Liu, Z. Chang, L. Luo, T. Xu, X. Lei, J. Liu, X. Sun, *Chem. Mater.* **2014**, 26, 1889.

[S9]  T. Maiyalagan, K. A. Jarvis, S. Therese, P. J. Ferreira, A. Manthiram, *Nat. Commun.* **2014**, 5, 3949.

[S10]  X. D. Wang, H. Y. Chen, Y. F. Xu, J. F. Liao, B. X. Chen, H. S. Rao, D. B. Kuang, C. Y. Su, *J. Mater. Chem. A* **2017**, 5, 7191.

[S11]  Y. Wu, Y. Liu, G. D. Li, X. Zou, X. Lian, D. Wang, L. Sun, T. Asefa, X. Zou, *Nano Energy* **2017**, 35, 161.

[S12]  M. R. Gao, J. X. Liang, Y. R. Zheng, Y. F. Xu, J. Jiang, Q. Gao, J. Li, S. H. Yu, *Nat. Commun.* **2015**, 6, 5982.

[S13]  L. L. Feng, G. Yu, Y. Wu, G. D. Li, H. Li, Y. Sun, T. Asefa, W. Chen, X. Zou, *J. Am. Chem. Soc.* **2015**, 137, 14023.

[S14]  J. Tian, Q. Liu, A. M. Asiri, X. Sun, *J. Am. Chem. Soc.* **2014**, 136, 7587.

# Chapter 4 Interfacial Nickel Nitride/Sulfide as a Bifunctional Electrode for Highly Efficient Overall Water/Seawater Electrolysis

## 4.1 Introduction and Significance

The development of bifunctional $Ni_3N$ and $Ni_3S_2$ electrocatalysts for overall water electrolysis with high activity and stability is preferable for commercialized hydrogen production and yet remains challenging. The interface plays a significant role in accelerating dissociative adsorption of water, which further improves the sluggish kinetics for electrochemical water electrolysis. However, conventional preparations fail to create the interface between the $Ni_3N$ and $Ni_3S_2$ species. Consequently, it is imperative to develop a facile method to create interface between the $Ni_3N$ and $Ni_3S_2$ species and to accelerate the kinetics for overall water electrolysis. Here, the regulation of interface and acceleration of dissociative adsorption of water were realized by one-step calcination in vacuum-sealed ampoule, catalytic mechanism was proposed, and the as-prepared interfacial nickel nitride and sulfide electrode exhibited excellent electrocatalytic performance for overall water electrolysis under neutral condition and in seawater. The highlights of this work include:

- One-step calcination in vacuum-sealed ampoule was firstly applied to synthesize $Ni_3N$ and $Ni_3S_2$ with abundant interface. And the dissociative adsorption of water was accelerated at the ubiquitous interface between the $Ni_3N$ and $Ni_3S_2$ species.

- Electrochemical impedance spectroscopy reveals that interfacial nickel nitride and sulfide electrode (NiNS) display comparable charge transfer with that of mechanically mixed nickel nitride and sulfide electrode (MNiNS). Meanwhile, the electrochemical surface area of NiNS is 16 times of that of MNiNS under similar loading. Therefore, the promoted electrocatalytic performance of NiNS is attributed to enlarged electrochemical surface area, which is a result of abundant interface between the $Ni_3N$ and $Ni_3S_2$ species. Consequently, dissociative adsorption of water was accelerated and electrocatalytic performance of NiNS was

enhanced.

- Owing to abundant interface between the $Ni_3N$ and $Ni_3S_2$ species, as-prepared NiNS electrode displayed excellent electrocatalytic activity and stability, which compared favorably with that of novel metal based electrocatalyst for water splitting under alkaline and neutral conditions and in seawater. The current density achieved at a potential of 1.8 V for NiNS//NiNS in buffer solution and seawater is 12.4 mA cm$^{-2}$ and 48.3 mA cm$^{-2}$, respectively, higher than that for Ir-C//Pt-C in buffer solution (6.7 mA cm$^{-2}$) and seawater (2.9 mA cm$^{-2}$).

## 4.2 Interfacial Nickel Nitride/Sulfide as a Bifunctional Electrode for Highly Efficient Overall Water/Seawater Electrolysis

This chapter is included as it appears as a journal paper published by Yongqiang Zhao, Bo Jin, Anthony Vasileff, Yan Jiao and Shi-Zhang Qiao, **Journal of Materials Chemistry A** 2019, 7, 8117.

# Statement of Authorship

| Title of Paper | Interfacial nickel nitride/sulfide as a bifunctional electrode for highly efficient overall water/seawater electrolysis |
|---|---|
| Publication Status | ☑ Published    ☐ Accepted for Publication<br>☐ Submitted for Publication    ☐ Unpublished and Unsubmitted work written in manuscript style |
| Publication Details | Yongqiang Zhao, Bo Jin, Anthony Vasileff, Yan Jiao and Shi-Zhang Qiao, Journal of Materials Chemistry A 2019, 7, 8117–8121. |

## Principal Author

| Name of Principal Author (Candidate) | Yongqiang Zhao |
|---|---|
| Contribution to the Paper | Research plan, material synthesis, most of the characterizations and data analysis, electrochemical measurements and manuscript drafting. |
| Overall percentage (%) | 70 |
| Certification: | This paper reports on original research I conducted during the period of my Higher Degree by Research candidature and is not subject to any obligations or contractual agreements with a third party that would constrain its inclusion in this thesis. I am the primary author of this paper. |
| Signature | Date  21/05/2019 |

## Co-Author Contributions

By signing the Statement of Authorship, each author certifies that:

    i.      the candidate's stated contribution to the publication is accurate (as detailed above);

    ii.     permission is granted for the candidate in include the publication in the thesis; and

    iii.    the sum of all co-author contributions is equal to 100% less the candidate's stated contribution.

| Name of Co-Author | Bo Jin |
|---|---|
| Contribution to the Paper | 8%. Discussion of research plan, data analysis and manuscript revision. |
| Signature | Date  1.05.2019 |

| Name of Co-Author | Anthony Vasileff |
|---|---|
| Contribution to the Paper | 6%. Assistance with manuscript edit and polish. |
| Signature | Date  21.05.2019. |

| Name of Co-Author | Yan Jiao |
|---|---|
| Contribution to the Paper | 6%. Discussion of research plan and data analysis. |
| Signature | | Date | 21 May 2019 |

| Name of Co-Author | Shi-Zhang Qiao |
|---|---|
| Contribution to the Paper | 10%. Supervision of the work, data interpretation and manuscript evaluation. |
| Signature | | Date | 21.05.2019 |

ROYAL SOCIETY
OF CHEMISTRY

## COMMUNICATION

Check for updates

# Interfacial nickel nitride/sulfide as a bifunctional electrode for highly efficient overall water/ seawater electrolysis†

Yongqiang Zhao,[a] Bo Jin,[a] Anthony Vasileff, [ID][a] Yan Jiao[a] and Shi-Zhang Qiao [ID] *[ab]

Simple methods for fabricating highly active and stable bifunctional electrocatalysts for water electrolysis are essential for hydrogen production. A nickel nitride/sulfide electrode (NiNS), whereby $Ni_3N$ and $Ni_3S_2$ species are interfaced, is synthesized *via* a one-step calcination process of Ni foam with thiourea in a vacuum-sealed ampoule. The resultant NiNS can be employed directly as a bifunctional electrocatalyst for water splitting with excellent activity toward the hydrogen evolution reaction and oxygen evolution reaction. The significant electrocatalytic performance of NiNS is attributed to the interface between $Ni_3N$ and $Ni_3S_2$, which functions as the electrochemical active sites and is beneficial for dissociative adsorption of water molecules. Current densities of 12.4 mA cm$^{-2}$ and 48.3 mA cm$^{-2}$ at 1.8 V are achieved for overall water electrolysis under neutral pH conditions and in seawater, respectively, when NiNS is applied as both the anode and cathode. This performance is significantly better than that of the benchmark Ir–C and Pt–C electrode system. Accordingly, interfacial NiNS is a promising bifunctional candidate for realistic large-scale water electrolysis.

## Introduction

Production of hydrogen and oxygen *via* electrochemical water splitting is an appealing and sustainable method of energy storage for renewable sources.[1–4] Overall water electrolysis requires effective electrocatalysts to accelerate both the hydrogen evolution reaction (HER) and oxygen evolution reaction (OER). Therefore, the development of bifunctional electrocatalysts that are active for both the HER and the OER is a crucial factor.[5] Currently, the benchmark electrocatalysts for the HER are Pt-based materials and the most effective

electrocatalysts for the OER are Ir/Ru-based materials.[6] However, their large-scale application is circumscribed by their high cost and scarcity. Therefore, the development of non-precious bifunctional electrocatalysts with high activity and long-term stability for overall water electrolysis is required.[7]

During recent years, non-precious metal and non-metal electrocatalysts have been intensely investigated. These materials include transition metal borides/carbides/nitrides/phosphides/oxides/chalcogenides,[8–14] perovskites,[15] and carbon materials.[16] Among these electrocatalysts, nitride- and sulfide-based compounds are found to be very promising water splitting electrocatalysts due to their high electronic conductivities.[17,18] However, improving their electrocatalytic activities is greatly hindered by their lack of active sites. Consequently, various strategies like doping hetero-atoms,[19] optimizing chemical composition,[20] regulating specific morphologies,[21] and exposing high-index facets,[22] have been developed to address this challenge. Despite the many strategies developed, there has been little research on promoting the electrocatalytic activity of nitride and sulfide materials by creating interfaces between nitride and sulfide species. It has been documented that the interface plays a significant role in accelerating dissociative adsorption of water,[23] which further improves the kinetics for electrochemical water electrolysis.[24] In this regard, interface regulation would be a favorable strategy to enhance catalytic activity of electrocatalysts for both the HER and OER.

Herein, we report a novel interfacial nickel nitride/sulfide (NiNS) electrode that is fabricated by a simple one-step calcination process of nickel foam with thiourea in a vacuum sealed ampoule. Benefiting from the interfacial contact between the $Ni_3N$ and $Ni_3S_2$ species, the as-prepared NiNS exhibited excellent electrocatalytic activity and stability for the HER and the OER. A mechanically-mixed $Ni_3N$ and $Ni_3S_2$ electrode (MNiNS) with similar loading was also prepared to explore its catalytic performance. Inspired by its significant electrocatalytic capability, as-synthesized NiNS was used as both anode and cathode for overall water electrolysis. Results show that NiNS exhibits greater electrocatalytic activity at low

*[a]School of Chemical Engineering, The University of Adelaide, Adelaide, SA 5005, Australia. E-mail: s.qiao@adelaide.edu.au*

*[b]School of Materials Science and Engineering, Tianjin University, Tianjin, 300072, China*

This journal is © The Royal Society of Chemistry 2019

*J. Mater. Chem. A*, 2019, 7, 8117–8121 | 8117

53

overpotentials under neutral pH conditions and in seawater compared to the benchmark system. This is attributed to the interfacial contact between $Ni_3N$ and $Ni_3S_2$ species. It is concluded that the novel design and fabrication of interfacial NiNS can provide a promising pathway for promoting neutral water/seawater electrolysis performance and reducing costs for hydrogen production.

## Results and discussion

The interfacial NiNS was synthesized by a simple one-step calcination process of Ni foam with thiourea powder in a vacuum sealed ampoule. During the calcination, interfacial NiNS was formed under a self-generated pressure (see details in ESI†). The elemental mappings of NiNS (Fig. 1a and S1, ESI†) show that Ni, N and S are homogeneously dispersed over the whole architecture. The composition of NiNS was characterized by elemental analysis (Table S1, ESI†). The as-prepared NiNS consists of nickel (87.18 wt%), nitrogen (4.17 wt%) and sulfur (8.65 wt%). The fragments of NiNS (exfoliated from the resulting electrode) were studied by scanning transmission electron microscopy (STEM), transmission electron microscopy (TEM) and high resolution TEM (HRTEM). The STEM and TEM images demonstrate the crystal structure of NiNS (Fig. 1a and b). The selective area electron diffraction (SAED) pattern (inset of Fig. 1b) displays several continuous bright rings, indicating a polycrystalline structure for as-prepared NiNS. The HRTEM images of the interfacial NiNS (Fig. 1c and d) show the prevalence of interfacial regions between $Ni_3N$ and $Ni_3S_2$ species. The interface is distinctly observed between the well-resolved lattice fringes of the (100) plane for $Ni_3N$ species and the ($1\bar{1}0$) plane of the $Ni_3S_2$ species (Fig. 1c). The well-defined lattice fringes with

inter-planar spacing of 0.204 and 0.215 nm can be unambiguously assigned to the (111) and (002) crystal planes of $Ni_3N$ with an intersection angle of 61.8° (Fig. 1d), in agreement with previous reports.[10,18,25] The unique lattice fringes with inter-planar distance of 0.183 nm correspond to the (210) crystal plane of $Ni_3S_2$. Noticeable interface between the (111) and (002) planes of $Ni_3N$ and the (210) plane of $Ni_3S_2$ is also observed. Interfacial regions between various planes of $Ni_3N$ and $Ni_3S_2$ species were confirmed by HRTEM, suggesting ubiquitous interfacial contact between the two throughout the material. We propose the formation mechanism of interfacial regions as follows. $NH_3$ and $H_2S$ that were produced by decomposition of thiourea over the nickel substrate at high temperature. Nickel sulfide was formed first given the bond energy of H–S is lower than that of H–N. Subsequently, $NH_3$ reacted with surface atoms of nickel sulfide forming interfacial regions between $Ni_3N$ and $Ni_3S_2$.

X-ray diffraction (XRD) was applied to characterize the crystal structure of NiNS (Fig. 2a). The diffraction peaks of NiNS are consistent with the (110), (002), (111), (112), and (300) planes for $Ni_3N$, as well as the (100), ($1\bar{1}0$), (111), (210), ($2\bar{1}1$), (310), and ($1\bar{3}1$) planes for $Ni_3S_2$, and agrees with HRTEM images.

Surface chemistry of NiNS was analyzed by X-ray photoelectron spectroscopy (XPS). The XPS survey spectrum (Fig. 2b) shows the presence of N and S in NiNS, indicating the formation of nickel nitride and sulfide. The high-resolution XPS spectrum of Ni 2p (Fig. 2c) displays two core-level peaks
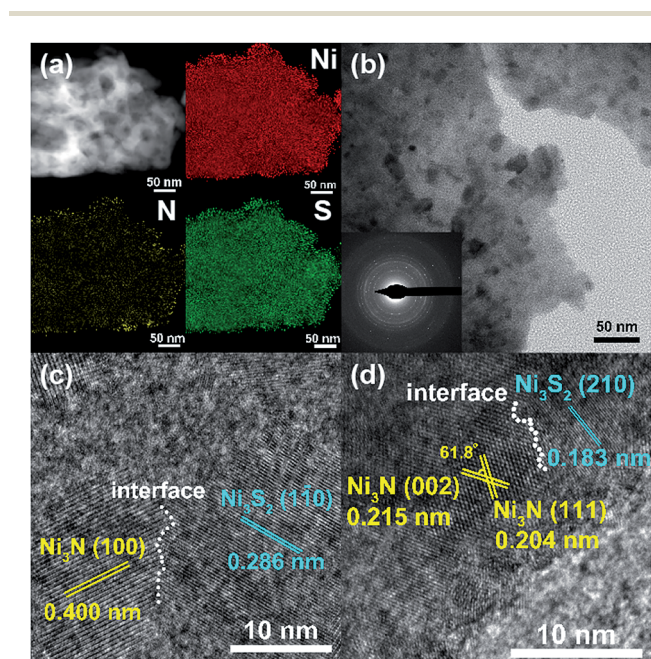


Fig. 1 (a) STEM image of NiNS and corresponding mapping images of Ni, N and S. (b) TEM image and (inset) corresponding SAED pattern of NiNS. (c, d) HRTEM images of NiNS.
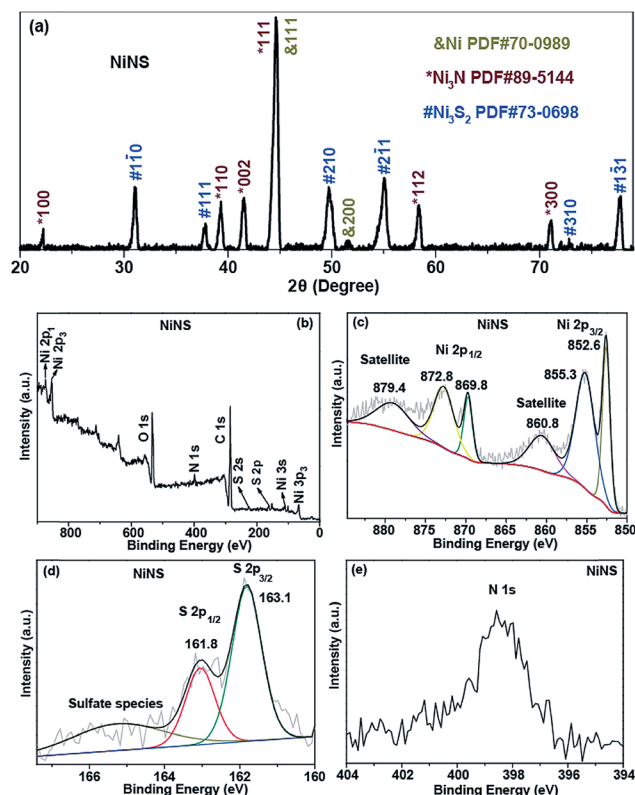


Fig. 2 (a) XRD pattern for NiNS. (b) XPS survey spectrum for NiNS. XPS spectrum of (c) Ni 2p, (d) S 2p and (e) N 1s for NiNS.

**8118** | *J. Mater. Chem. A*, 2019, **7**, 8117–8121

This journal is © The Royal Society of Chemistry 2019

54

of Ni centered at 855.3 and 872.8 eV, which are ascribed to $Ni^{2+}$ $2p_{3/2}$ and $Ni^{2+}$ $2p_{1/2}$, respectively.[26] Two satellite peaks at 860.8 ($2p_{3/2}$) and 879.4 eV ($2p_{1/2}$) are also observed. Two peaks at 852.6 ($2p_{3/2}$) and 869.8 eV ($2p_{1/2}$) suggest a metallic state of nickel,[26] which is consistent with the XRD patterns. The core-level scan spectrum of S 2p (Fig. 2d) can be divided into two main characteristic peaks at 161.8 and 163.1 eV, and are ascribed to the S $2p_{3/2}$ and S $2p_{1/2}$, respectively.[19] The high-resolution N 1s spectrum (Fig. 2e) shows a distinct peak at 398.6 eV that can be assigned to Ni–N bonding.[27] Based on the aforementioned discussions, nickel nitride/sulfide was successfully incorporated on the Ni substrate and formed an interfacial NiNS electrode.

Individual nickel nitride and nickel sulfide samples were also prepared. The scanning electron microscopy (SEM) images and elemental mappings of nickel nitride (Fig. S2, ESI†) and nickel sulfide (Fig. S3, ESI†) demonstrate that nickel nitride and nickel sulfide were successfully synthesized. The crystal structure of nickel nitride (Fig. S4a, ESI†) and nickel sulfide (Fig. S4b, ESI†) samples were characterized by XRD.

The HER activity of interfacial NiNS was evaluated by directly using the material as the working electrode. For comparison, MNiNS, bare nickel foam and Pt–C loaded on Ni foam (Ni/Pt–C) were prepared. The linear sweep voltammetry (LSV) curves
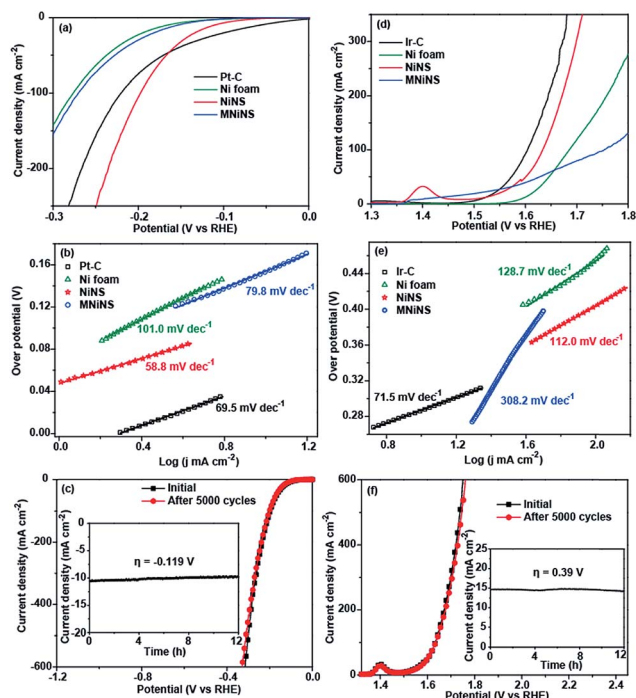


**Fig. 3** (a) HER performance of NiNS, MNiNS, Ni foam, and Pt–C in Ar-saturated 1.0 M KOH. (b) Corresponding Tafel plots with associated linear fittings. (c) Cycle stability of NiNS and (inset) time-dependent current density of NiNS under a constant overpotential of −0.119 V (vs. RHE) in 1.0 M KOH. (d) OER performance of NiNS, MNiNS, Ni foam, and Ir–C in $O_2$-saturated 1.0 M KOH. (e) Corresponding Tafel plots with associated linear fittings. (f) Cycle stability of NiNS and (inset) time-dependent current density of NiNS under a constant overpotential of 0.39 V (vs. RHE) in 1.0 M KOH.

(Fig. 3a) display that a 100 mA $cm^{-2}$ current density was achieved at an overpotential of 197 mV for NiNS, which was lower than that for MNiNS (271 mV) and Pt–C (220 mV). A comparative summary of the electrocatalytic activities of state-of-the-art HER catalysts reported recently is presented in Table S2 in the ESI.† With an overpotential of 197 mV at 100 mA $cm^{-2}$, NiNS demonstrated more favorable electrocatalytic activity compared to most active non-noble metal based electrocatalysts, such as $Ni_3N$–Co (290 mV),[28] $Co_3Se_4$/Co (262 mV),[29] $Pr_{0.5}(Ba_{0.5}Sr_{0.5})_{0.5}Co_{0.8}Fe_{0.2}O_{3-\delta}$ (310 mV),[30] and $NiCo_2O_4$/Ni (275 mV).[31] The Tafel slope for NiNS was found to be 58.8 mV $dec^{-1}$ (Fig. 3b), which is smaller than that of Ni/Pt–C (69.5 mV $dec^{-1}$) and MNiNS (79.8 mV $dec^{-1}$), indicating more favorable HER kinetics. A Tafel slope within the range of 40–120 mV $dec^{-1}$ suggests that the HER might proceed via the Volmer–Heyrovsky mechanism on NiNS.[32] NiNS displayed stable electrocatalytic performance for 5000 HER cycles (Fig. 3c) and negligible degradation of current density during 12 h of operation (inset of Fig. 3c). The XRD pattern of NiNS after 12 h continuous HER operation (Fig. S5a, ESI†) showed that NiNS was structurally stable under operating conditions.

The HER kinetics were further analyzed through electrochemical impedance spectroscopy (EIS) (Fig. S6, ESI†). The Nyquist plots of NiNS and MNiNS display a semicircle in the low-frequency range (an indicator of charge transfer resistance of the catalysts). The calculated resistance of NiNS (1.47 Ω) is similar with that of MNiNS (1.89 Ω), indicating comparable charge transfer. To obtain a profound insight into the electrocatalytic mechanism, the electrochemical surface areas of NiNS and MNiNS were characterized from the double layer capacitance (Fig. S7, ESI†). The electrochemical surface area of NiNS is 16 times of that of MNiNS under similar loading, suggesting that NiNS possess extra electrochemical active sites. From previous discussion, it is clearly seen that NiNS and MNiNS possess similar composition and structure, except for the presence of interfacial regions. Consequently, the increased number of electrochemically active sites on NiNS could be attributed to the ubiquitous interfaces between $Ni_3N$ and $Ni_3S_2$ species. Previous study showed that interfacial sites are effective for water adsorption and subsequent cleavage of the HO–H bond.[33] We propose that efficient dissociative adsorption of water molecules happens at interfacial sites between $Ni_3N$ and $Ni_3S_2$ species, followed by hydrogen adsorption ($H_{ad}$) on the adjacent $E^{\delta-}$ (E = N and S) centers. These $E^{\delta-}$ centers can significantly enhance adsorption and discharge of $H_{ad}$ and promote the HER.[34–36] Finally, two $H_{ad}$ atoms recombine to form $H_2$ ($H_2$ desorption) and $OH^-$ desorbs, followed by adsorption of another water molecule on the interfacial site. Given that NiNS and MNiNS possess similar charge transfer resistance, the substantially promoted HER performance of NiNS is predominantly attributed to the ubiquitous interface between $Ni_3N$ and $Ni_3S_2$ species.

The catalytic activity of NiNS for the OER was evaluated in identical electrolyte to that of the HER study. MNiNS, bare nickel foam and Ir–C loaded on Ni foam (Ni/Ir–C) were selected for comparison. The LSV curves (Fig. 3d) show that a 100 mA $cm^{-2}$ current density was realized at an overpotential of 404 mV

This journal is © The Royal Society of Chemistry 2019

J. Mater. Chem. A, 2019, 7, 8117–8121 | **8119**

55

for NiNS, which was lower than that for MNiNS (524 mV) and comparable with that for Ni/Ir–C (374 mV). An oxidation peak at around 1.4 V (*vs.* reversible hydrogen electrode, RHE) for NiNS is observed in Fig. 3d, which is attributed to the formation of nickel oxide and hydroxide species.[37] A comparative summary of the OER electrocatalytic performance of state-of-the-art catalysts reported in recent works is presented in Table S3 in ESI.† The electrocatalytic activity of NiNS (an overpotential of 404 mV at 100 mA cm$^{-2}$) is comparable with most active non-noble metal based electrocatalysts, such as $MoS_2/NiS$ (475 mV),[38] NF@Ni/C-600 (460 mV),[39] $Ni_3S_2$/NF-2 (425 mV),[40] and $NiCo_2O_4$@$CoMoO_4$/NF-7 (510 mV).[41] The Tafel slope for NiNS was found to be 112.0 mV dec$^{-1}$ (Fig. 3e), which is much lower than that of MNiNS (308.2 mV dec$^{-1}$), indicating more favorable OER kinetics. After continuous testing with 5000 cycles, no obvious current density attenuation was observed for NiNS (Fig. 3f). NiNS also exhibited stable current density over 12 h of continuous operation (inset of Fig. 3f). The XRD pattern of NiNS after 12 h continuous OER operation (Fig. S5b, ESI†) indicates that NiNS structurally very stable, demonstrating its potential value as a catalyst.

Further, two electrodes electrolyzer systems with 1.0 M KOH, buffer solution and seawater were established. These systems integrated two NiNS electrodes as both anode and cathode for overall water electrolysis (denoted as NiNS//NiNS). Ir–C/Ni and Pt–C/Ni (denoted as Ir–C//Pt–C) were also applied for comparison. Fig. 4 presents the LSV curves of the NiNS//NiNS and Ir–C//Pt–C for overall water electrolysis in various solutions. Although the electrocatalytic performance of Ir–C//Pt–C in 1.0 M KOH electrolyte exceeded that of NiNS//NiNS, the latter exhibited superior electrocatalytic activity in buffer solution and seawater (Fig. 4a). The current density achieved at a potential of 1.8 V for NiNS//NiNS in buffer solution and seawater was 12.4 mA cm$^{-2}$ and 48.3 mA cm$^{-2}$, respectively, higher than that for Ir–C//Pt–C (6.7 mA cm$^{-2}$ and 2.9 mA cm$^{-2}$). This is likely attributed to the ubiquitous interfacial contact between $Ni_3N$ and $Ni_3S_2$ species which acts as the electrocatalytic active sites. Notably, the electrocatalytic activity of NiNS//NiNS in seawater compares extraordinarily well with that of the most active metal based electrocatalysts, such as $WO_3$/g-$C_3N_4$,[42] PtRuMo,[43] and MHCM-z-BCC/NiMoS.[44] NiNS//NiNS also exhibited stable current density at a constant potential of 1.88 V during 12 h of continuous operation (Fig. 4b).

## Conclusions

A simple method was developed to fabricate bifunctional NiNS electrodes with abundant interfacial contact between $Ni_3N$ and $Ni_3S_2$ species. The obvious interface between various planes of $Ni_3N$ and $Ni_3S_2$ species was confirmed by HRTEM. Acting as the electrocatalytic active sites, these ubiquitous interfaces are beneficial for dissociative adsorption of water molecules and consequent water electrolysis. This structural feature resulted in excellent overall water splitting performance under neutral pH conditions and in seawater. The electrocatalytic mechanism was explored by the study of electrochemical active sites, which suggested that the abundant interfacial regions is predominantly responsible for the excellent catalytic performance. This work provides new opportunities for the development of low cost and efficient bifunctional interfacial electrocatalysts for overall water electrolysis under neutral pH conditions and in seawater.

## Conflicts of interest

There are no conflicts to declare.

## Acknowledgements

## Notes and references

1 M. Tahir, L. Pan, F. Idrees, X. Zhang, L. Wang, J.-J. Zou and Z. L. Wang, *Nano Energy*, 2017, **37**, 136–157.

2 Q. Zhao, Z. Yan, C. Chen and J. Chen, *Chem. Rev.*, 2017, **117**, 10121–10211.

3 B. You and Y. Sun, *Acc. Chem. Res.*, 2018, **51**, 1571–1580.

4 Y. Zheng, Y. Jiao, A. Vasileff and S.-Z. Qiao, *Angew. Chem., Int. Ed.*, 2018, **57**, 7568–7579.

5 I. Roger, M. A. Shipman and M. D. Symes, *Nat. Rev. Chem.*, 2017, **1**, 0003.

6 Y. Jiao, Y. Zheng, M. Jaroniec and S.-Z. Qiao, *Chem. Soc. Rev.*, 2015, **44**, 2060–2086.

7 V. Vij, S. Sultan, A. M. Harzandi, A. Meena, J. N. Tiwari, W.-G. Lee, T. Yoon and K. S. Kim, *ACS Catal.*, 2017, **7**, 7196–7225.

8 J. Masa, P. Weide, D. Peeters, I. Sinev, W. Xia, Z. Sun, C. Somsen, M. Muhler and W. Schuhmann, *Adv. Energy Mater.*, 2016, **6**, 1502313.

9 N. Han, K. R. Yang, Z. Lu, Y. Li, W. Xu, T. Gao, Z. Cai, Y. Zhang, V. S. Batista, W. Liu and X. Sun, *Nat. Commun.*, 2018, **9**, 924.

10 F. Song, W. Li, J. Yang, G. Han, P. Liao and Y. Sun, *Nat. Commun.*, 2018, **9**, 4531.



Fig. 4 (a) Polarization curves of NiNS//NiNS and Ir−C//Pt−C overall water splitting systems in 1.0 M KOH, buffer solution (pH = 7.4) and seawater. (b) Time-dependent current density of NiNS//NiNS under 1.88 V for an overall water splitting system in 1.0 M KOH.

11 K. Xu, H. Cheng, H. Lv, J. Wang, L. Liu, S. Liu, X. Wu, W. Chu, C. Wu and Y. Xie, *Adv. Mater.*, 2018, **30**, 1703322.

12 Y. Hao, Y. Xu, W. Liu and X. Sun, *Mater. Horiz.*, 2018, **5**, 108–115.

13 T. Ling, D.-Y. Yan, H. Wang, Y. Jiao, Z. Hu, Y. Zheng, L. Zheng, J. Mao, H. Liu, X.-W. Du, M. Jaroniec and S.-Z. Qiao, *Nat. Commun.*, 2017, **8**, 1509.

14 J.-X. Feng, J.-Q. Wu, Y.-X. Tong and G.-R. Li, *J. Am. Chem. Soc.*, 2018, **140**, 610–617.

15 E. Fabbri, M. Nachtegaal, T. Binninger, X. Cheng, B.-J. Kim, J. Durst, F. Bozza, T. Graule, R. Schäublin, L. Wiles, M. Pertoso, N. Danilovic, K. E. Ayers and T. J. Schmidt, *Nat. Mater.*, 2017, **16**, 925–931.

16 Y. Zheng, Y. Jiao, J. Chen, J. Liu, J. Liang, A. Du, W. Zhang, Z. Zhu, S. C. Smith, M. Jaroniec, G. Q. Lu and S.-Z. Qiao, *J. Am. Chem. Soc.*, 2011, **133**, 20116–20119.

17 N. Jiang, Q. Tang, M. Sheng, B. You, D. Jiang and Y. Sun, *Catal. Sci. Technol.*, 2016, **6**, 1077–1084.

18 K. Xu, P. Chen, X. Li, Y. Tong, H. Ding, X. Wu, W. Chu, Z. Peng, C. Wu and Y. Xie, *J. Am. Chem. Soc.*, 2015, **137**, 4119–4125.

19 P. Chen, T. Zhou, M. Zhang, Y. Tong, C. Zhong, N. Zhang, L. Zhang, C. Wu and Y. Xie, *Adv. Mater.*, 2017, **29**, 1701584.

20 Y. Yang, K. Zhang, H. Lin, X. Li, H. C. Chan, L. Yang and Q. Gao, *ACS Catal.*, 2017, **7**, 2357–2366.

21 H. Q. Fu, L. Zhang, C. W. Wang, L. R. Zheng, P. F. Liu and H. G. Yang, *ACS Energy Lett.*, 2018, **3**, 2021–2029.

22 Y. Tang, H. Yang, J. Sun, M. Xia, W. Guo, L. Yu, J. Yan, J. Zheng, L. Chang and F. Gao, *Nanoscale*, 2018, **10**, 10459–10466.

23 M. A. Henderson, *Surf. Sci. Rep.*, 2002, **46**, 85–150.

24 H. Wu, S. Li, X. Lu, C. Y. Toe, H. Y. Chung, Y. Tang, X. Lu, R. Amal, L. Li and Y. H. Ng, *ChemPlusChem*, 2018, **83**, 934–940.

25 M.-S. Balogun, Y. Zeng, W. Qiu, Y. Luo, A. Onasanya, T. K. Olaniyi and Y. Tong, *J. Mater. Chem. A*, 2016, **4**, 9844–9849.

26 B. Zhang, C. Xiao, S. Xie, J. Liang, X. Chen and Y. Tang, *Chem. Mater.*, 2016, **28**, 6934–6941.

27 B. Li, H. Nam, J. Zhao, J. Chang, N. Lingappan, F. Yao, T. H. Lee and Y. H. Lee, *Adv. Mater.*, 2017, **29**, 1605083.

28 C. Zhu, A.-L. Wang, W. Xiao, D. Chao, X. Zhang, N. H. Tiep, S. Chen, J. Kang, X. Wang, J. Ding, J. Wang, H. Zhang and H. J. Fan, *Adv. Mater.*, 2018, **30**, 1705516.

29 W. Li, X. Gao, D. Xiong, F. Wei, W.-G. Song, J. Xu and L. Liu, *Adv. Energy Mater.*, 2017, **7**, 1602579.

30 X. Xu, Y. Chen, W. Zhou, Z. Zhu, C. Su, M. Liu and Z. Shao, *Adv. Mater.*, 2016, **28**, 6442.

31 A. Sivanantham, P. Ganesan and S. Shanmugam, *Adv. Funct. Mater.*, 2016, **26**, 4661.

32 B. E. Conway and B. V. Tilak, *Electrochim. Acta*, 2002, **47**, 3571–3594.

33 R. Subbaraman, D. Tripkovic, D. Strmcnik, K.-C. Chang, M. Uchimura, A. P. Paulikas, V. Stamenkovic and N. M. Markovic, *Science*, 2011, **334**, 1256–1260.

34 S. Anantharaj, S. R. Ede, K. Sakthikumar, K. Karthick, S. Mishra and S. Kundu, *ACS Catal.*, 2016, **6**, 8069–8097.

35 Y. Tang, P. Wang, J.-H. Yun, R. Amal and Y. H. Ng, *J. Mater. Chem. A*, 2015, **3**, 15876–15881.

36 Y. Tang, P. Traveerungroj, H. L. Tan, P. Wang, R. Amal and Y. H. Ng, *J. Mater. Chem. A*, 2015, **3**, 19582–19587.

37 D. Zhu, C. Guo, J. Liu, L. Wang, Y. Du and S.-Z. Qiao, *Chem. Commun.*, 2017, **53**, 10906–10909.

38 Z. Zhai, C. Li, L. Zhang, H.-C. Wu, L. Zhang, N. Tang, W. Wang and J. Gong, *J. Mater. Chem. A*, 2018, **6**, 9833–9838.

39 H. Sun, Y. Lian, C. Yang, L. Xiong, P. Qi, Q. Mu, X. Zhao, J. Guo, Z. Deng and Y. Peng, *Energy Environ. Sci.*, 2018, **11**, 2363–2371.

40 G. Liu, Z. Sun, X. Zhang, H. Wang, G. Wang, X. Wu, H. Zhang and H. Zhao, *J. Mater. Chem. A*, 2018, **6**, 19201–19209.

41 Y. Gong, Z. Yang, Y. Lin, J. Wang, H. Pan and Z. Xu, *J. Mater. Chem. A*, 2018, **6**, 16950–16958.

42 Y. Li, X. Wei, X. Yan, J. Cai, A. Zhou, M. Yang and K. Liu, *Phys. Chem. Chem. Phys.*, 2016, **18**, 10255–10261.

43 H. Li, Q. Tang, B. He and P. Yang, *J. Mater. Chem. A*, 2016, **4**, 6513–6520.

44 S. H. Hsu, J. Miao, L. Zhang, J. Gao, H. Wang, H. Tao, S. F. Hung, A. Vasileff, S.-Z. Qiao and B. Liu, *Adv. Mater.*, 2018, **30**, 1707261.

This journal is © The Royal Society of Chemistry 2019

*J. Mater. Chem. A*, 2019, **7**, 8117–8121 | **8121**

57

# Supporting Information

**Interfacial Nickel Nitride/Sulfide as a Bifunctional Electrode for Highly Efficient Overall Water/Seawater Electrolysis**

Yongqiang Zhao[a], Bo Jin[a], Anthony Vasileff[a], Yan Jiao[a], Shi-Zhang Qiao*[ab]

[a.] School of Chemical Engineering, The University of Adelaide, Adelaide, SA 5005, Australia,

E-mail: s.qiao@adelaide.edu.au

[b.] School of Materials Science and Engineering, Tianjin University, Tianjin, 300072, China

**Experimental**

**Chemicals:** Nickel foam (thickness 1.6 mm, 95%), thiourea (≥99.0%), sulphur (≥99.0%), phosphate buffer solution (1.0 M, pH=7.4) and nickel hydroxide (99%) were purchased from Sigma-Aldrich and used without further purification, except for the nickel foam. Milli-Q water (18.2 M $\Omega$cm, PURELAB Option-Q) was used in all experiments. The nickel foam was washed with dilute HCl, ultrapure water, acetone and ethanol, and dried in vacuum at 25 °C before use.

**Fabrication of the interfacial nickel nitride and sulfide electrode (NiNS):** The NiNS electrode was fabricated by a one-step calcination of nickel foam with thiourea in a vacuum sealed ampoule. In a typical synthesis, a pre-cleaned piece of Ni foam (20.60 mg, 1.5 cm × 0.3 cm × 0.16 cm, length × width × height) and thiourea (6.14 mg) were sealed in an ampoule under vacuum and then calcinated at 550 °C for 5 h. The heating rate was 5 °C min$^{-1}$ and the cooling process took place naturally. The mass ratio of Ni foam and thiourea was 1:0.298. The loading of nickel nitride and sufide was calculated to be 9.27 and 10.68 mg, respectively. The NiNS electrode was washed with ethanol and dried in vacuum at 25 °C before use.

**Fabrication of Pt-C and Ir-C Loaded Electrodes:** 4 mg Pt-C or Ir-C were dispersed in 1 mL water, followed by sonication for 30 min to obtain a homogeneous catalyst ink. 150 μL of the catalyst ink and 40 μL 2% Nafion solution were loaded in succession on the surface of Ni foam (surface area: 0.6 cm$^2$). The overall loading amount was 1 mg cm$^{-2}$.

**Fabrication of nickel nitride:** Nickel nitride ($Ni_3N$) was fabricated according to a modified method from previous literature.[S1] In a typical synthesis, 10 mg of nickel hydroxide was place in a tube furnace and heated to 390 °C under $NH_3$ flow (1 bar, 400 sccm) to prepare black $Ni_3N$.

**Fabrication of nickel sulfide:** Nickel sulfide ($Ni_3S_2$) was fabricated by a one-step calcination of nickel foam with sulfur in a vacuum sealed ampoule. In a typical synthesis, a pre-cleaned piece of Ni foam (20.60 mg, 1.5 cm × 0.3 cm × 0.16 cm, length × width × height) and sulfur (2.58 mg) were sealed in an ampoule under vacuum and then calcinated at 500 °C for 5 h. The heating rate was 5 °C min$^{-1}$ and the cooling process took place naturally. The nickel sulfide was washed with ethanol and dried in vacuum at 25 °C before use.

**Fabrication of mechanically mixed $Ni_3N$ and $Ni_3S_2$ electrode (MNiNS):** 103 mg $Ni_3N$ and 118.67 mg $Ni_3S_2$ were were dispersed in 1 mL 2% Nafion aqueous solution, followed by sonication for 30 min to obtain a homogeneous catalyst ink. 200 μL of the catalyst ink was loaded on the surface of pre-cleaned Ni foam (surface area: 1 cm$^2$). The as-prepared MNiNS electrode was dried at 40 °C in vacuum. The overall loading amount was 9.27 mg of $Ni_3N$ and 10.68 mg of $Ni_3S_2$, respectively.

**Electrochemical Characterization:** HER and OER measurements were performed on a CHI 760 D Bipotentiostat (CH Instruments, Inc., USA) in Ar or $O_2$ saturated 1.0 M KOH aqueous solution using a conventional three-electrode system with a graphite rod as the counter electrode and Ag/AgCl (4 M KCl) as the reference electrode. Overall water splitting measurements were performed in a three-electrode glass cell. The phosphate buffer solution was used for overall water electrolysis in neutral pH conditions. To investigate the performance of the systems in seawater, neutral-buffered seawater electrolyte was prepared. Natural seawater was collected from Glenelg beach in Adelaide, Australia, and was applied directly without further purification. The neutral-buffered seawater electrolyte was prepared by mixing phosphate buffer solution with natural seawater, and the pH of the mixed electrolyte was adjusted to 7.05. The current density was normalized to the geometric surface area and the measured potentials versus Ag/AgCl were converted to the reversible hydrogen electrode (RHE) scale according to the Nernst equation:

$$E_{RHE} = E_{Ag/AgCl} + 0.059 \times pH + 0.205 \tag{1}$$

The polarization curves were recorded in the range of 1.0-1.8 V vs. RHE for the OER and -0.6 to 0 V vs. RHE for the HER at a slow scan rate of 5 mV s$^{-1}$ to minimize the capacitive current. The working electrodes were scanned for several times until the signals were stabilized, and then the data for polarization curves were collected and corrected for the iR contribution within the cell. The stability test was conducted using a controlled-potential electrolysis method without iR compensation. The EIS was obtained by AC impedance spectroscopy within the frequency range from 0.01 to 100 kHz in 1.0 M KOH. The equivalent circuit for fitting of the EIS data was achieved with ZView software. The Tafel slope was calculated according to Tafel equation as follows:

$$\eta = b\log( j/j_0 ) \tag{2}$$

where $\eta$ denotes the overpotential, b denotes the Tafel slope, j denotes the current density, and $j_0$ denotes the exchange current density. The onset potentials were determined based on the beginning of the linear region in the Tafel plots. The overpotential was calculated as follows:

$$\eta = E \text{ (vs RHE)} – E_r \text{ (vs RHE)} \tag{3}$$

where E denotes the actual applied potential and $E_r$ denotes the reversible potential of the reaction. *E*r is 1.23 V versus RHE for the OER and 0 V vs. RHE for the HER. HER $\eta$ is always negative. The electrochemical surface area of the electrodes was related to double layer charging curves using cyclic voltammetry in the potential range 0.72 - 0.82 V vs. RHE. The double-layer capacitance values were determined from the slope of the capacitive current versus the scan rate.

**Physicochemical Characterization:** STEM images and corresponding mapping images were obtained on an FEI Titan Themis 80-200 system. Transmission electron microscopy (TEM) images and the selected area electron diffraction (SAED) patterns were obtained on a JEOL 2100F microscope at an acceleration voltage of 200 kV. High resolution TEM (HRTEM) images were obtained on a Philips CM200 microscope at an acceleration voltage of 200 kV. Scanning electron microscopy (SEM) images were collected on the FEI Quanta 450 at high vacuum with an accelerating voltage of 30 kV. X-ray diffraction (XRD) patterns were collected on a powder X-ray diffractometer at 40 kV and 15 mA using Co-Kα radiation (Miniflex, Rigaku). X-ray photoelectron spectra (XPS) were obtained using an Axis Ultra (Kratos Analytical, UK) XPS spectrometer equipped with an Al Kα source (1486.6 eV). The composition of NiNS was determined by element analysis (vario EL cube, ELE-MENTAR).

**Supplementary Results**
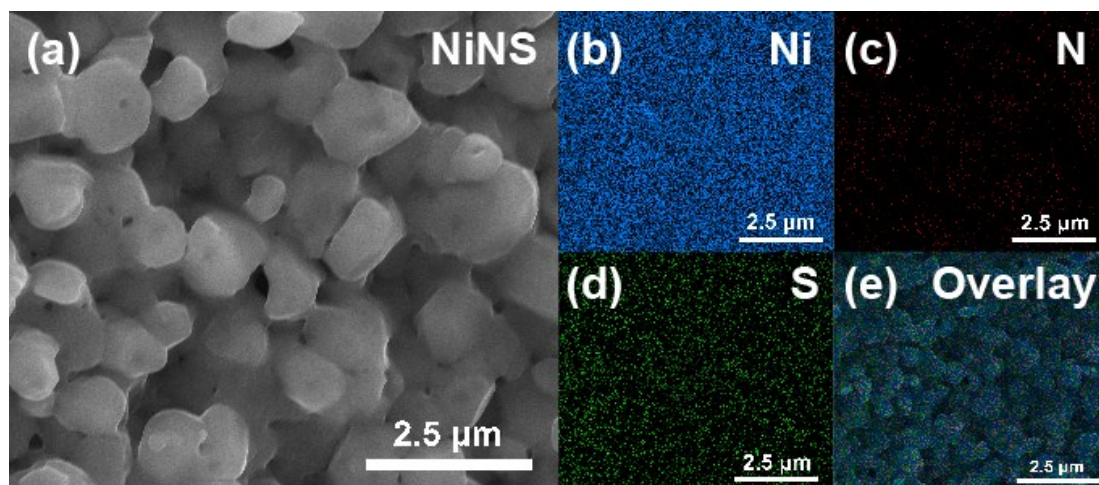


**Fig. S1** (a) SEM image of NiNS. Corresponding mapping of (b) Ni, (c) N, (d) S, and (e) overlay.
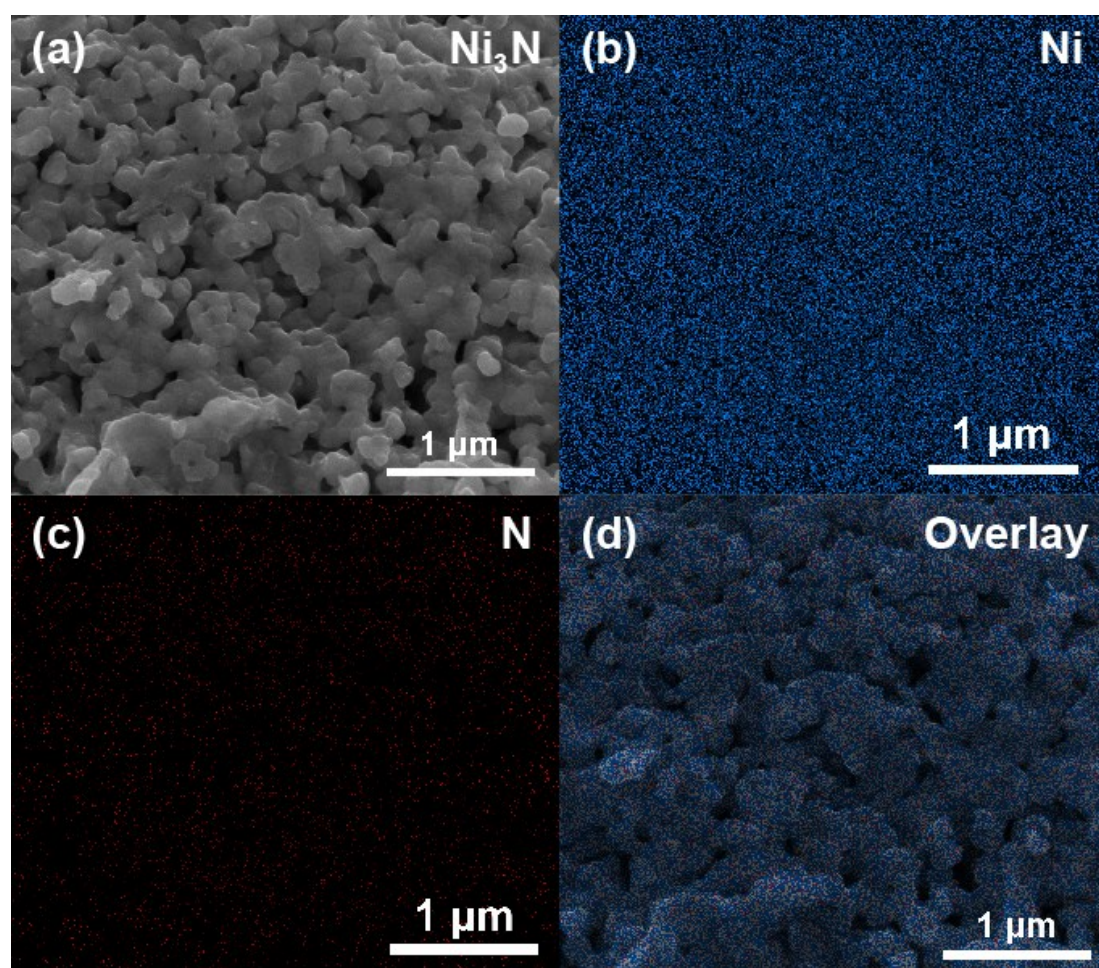


**Fig. S2** (a) SEM image of nickel nitride. Corresponding mapping of (b) Ni, (c) N, and (d) overlay.
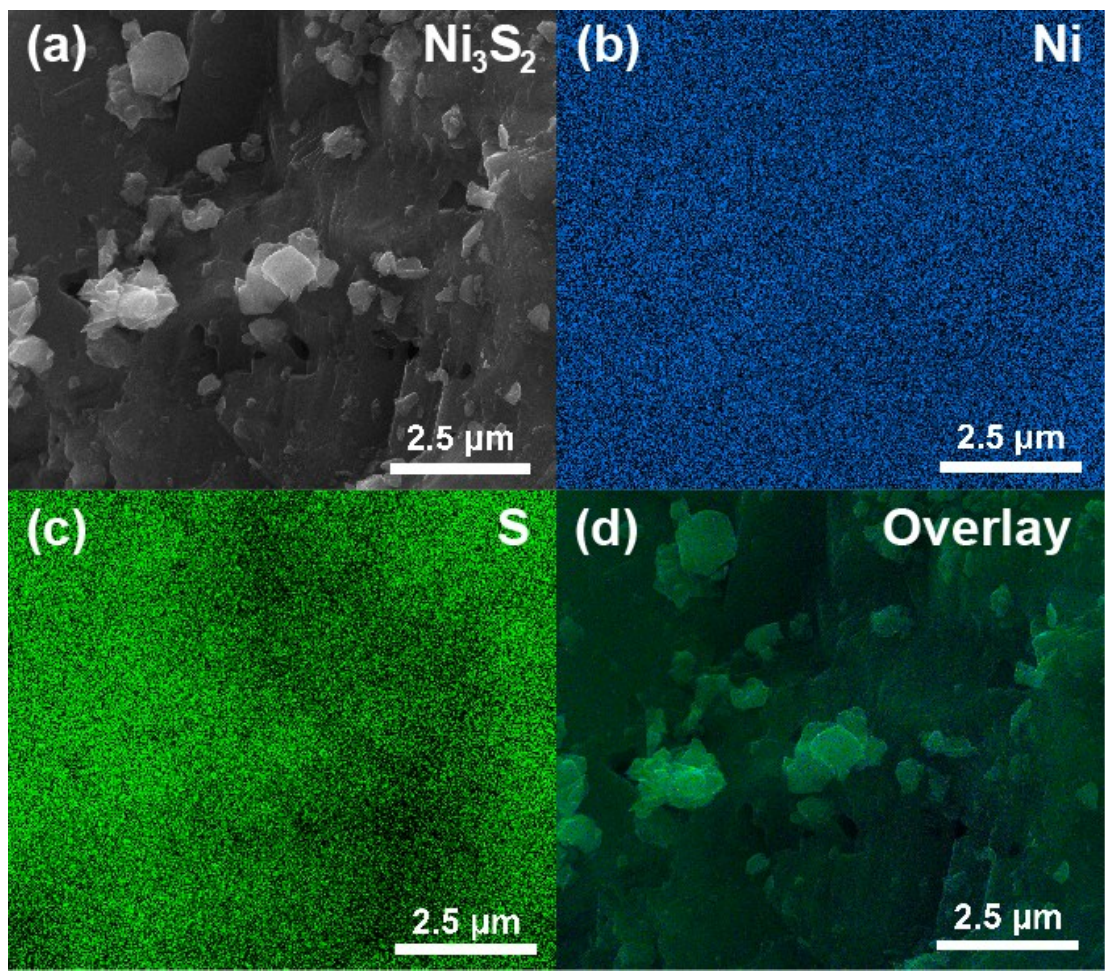
**Fig. S3** (a) SEM image of nickel sulfide. Corresponding mapping of (b) Ni, (c) S, and (d) overlay.
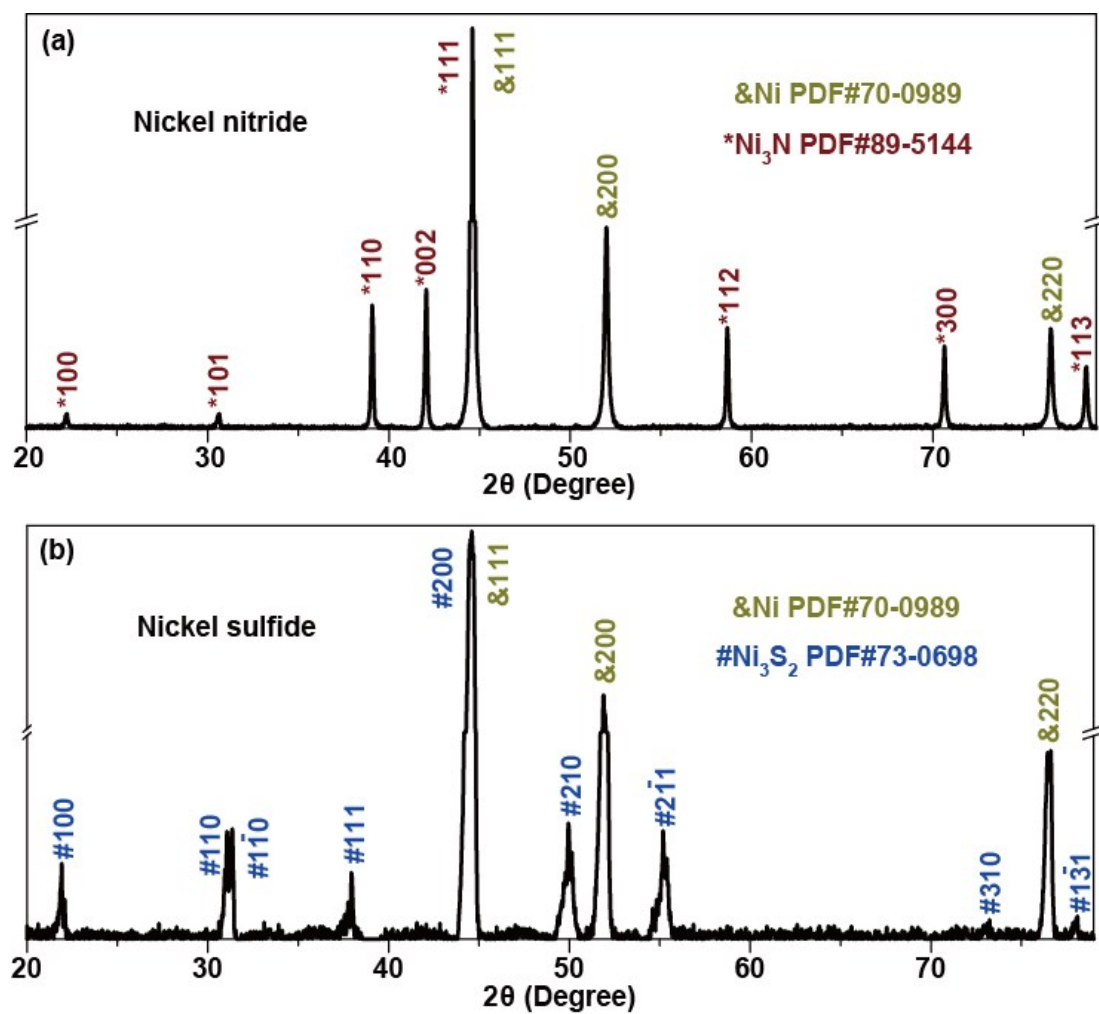
**Fig. S4** XRD patterns of (a) nickel nitride and (b) nickel sulfide.
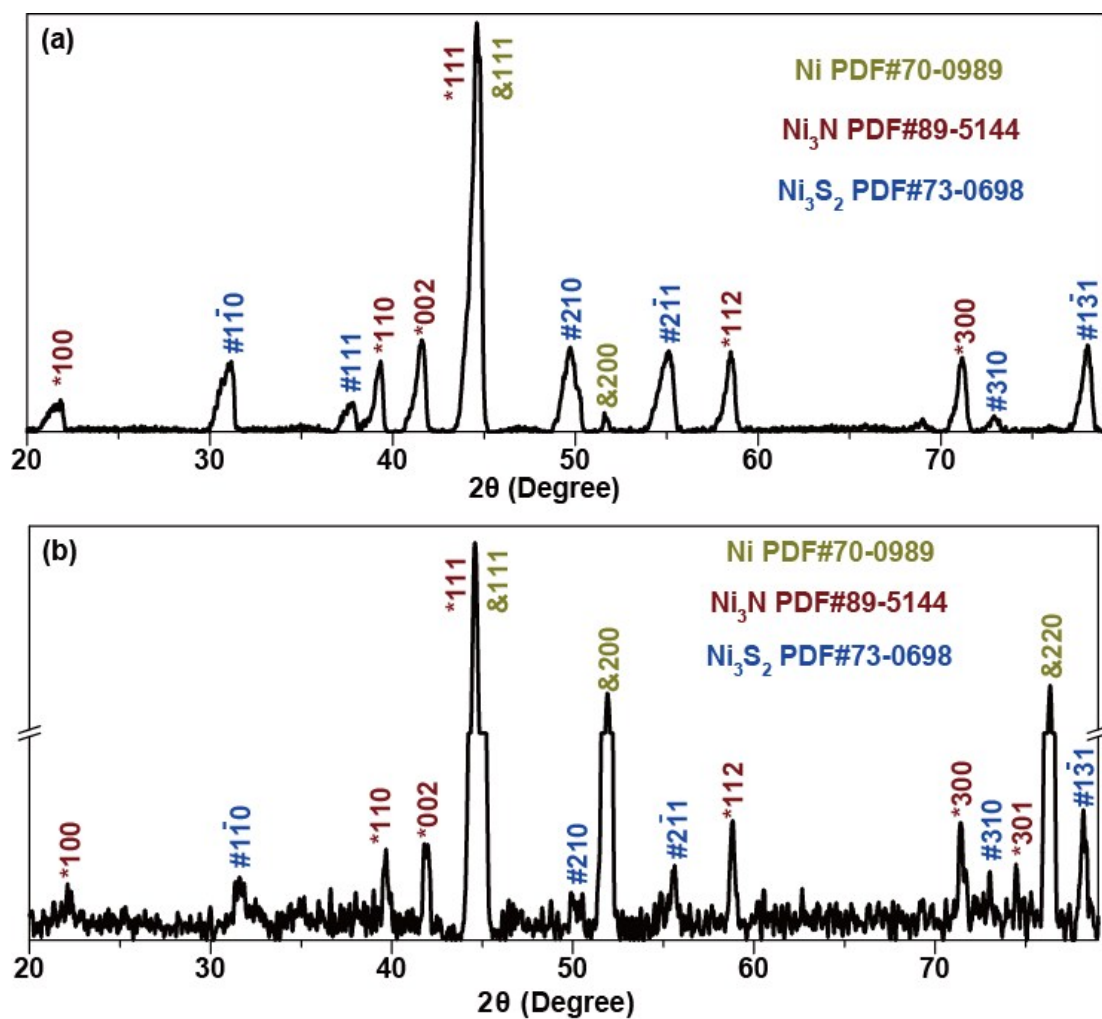
**Fig. S5** XRD patterns of NiNS after 12 h continuous (a) HER and (b) OER operation.
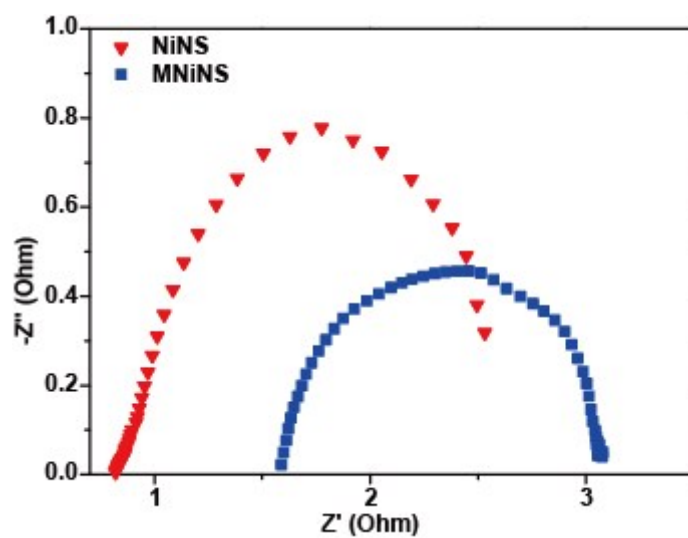


**Fig. S6** Nyquist plots of NiNS and MNiNS electrodes in 1.0 M KOH with the potential of -1.31 V vs. RHE.
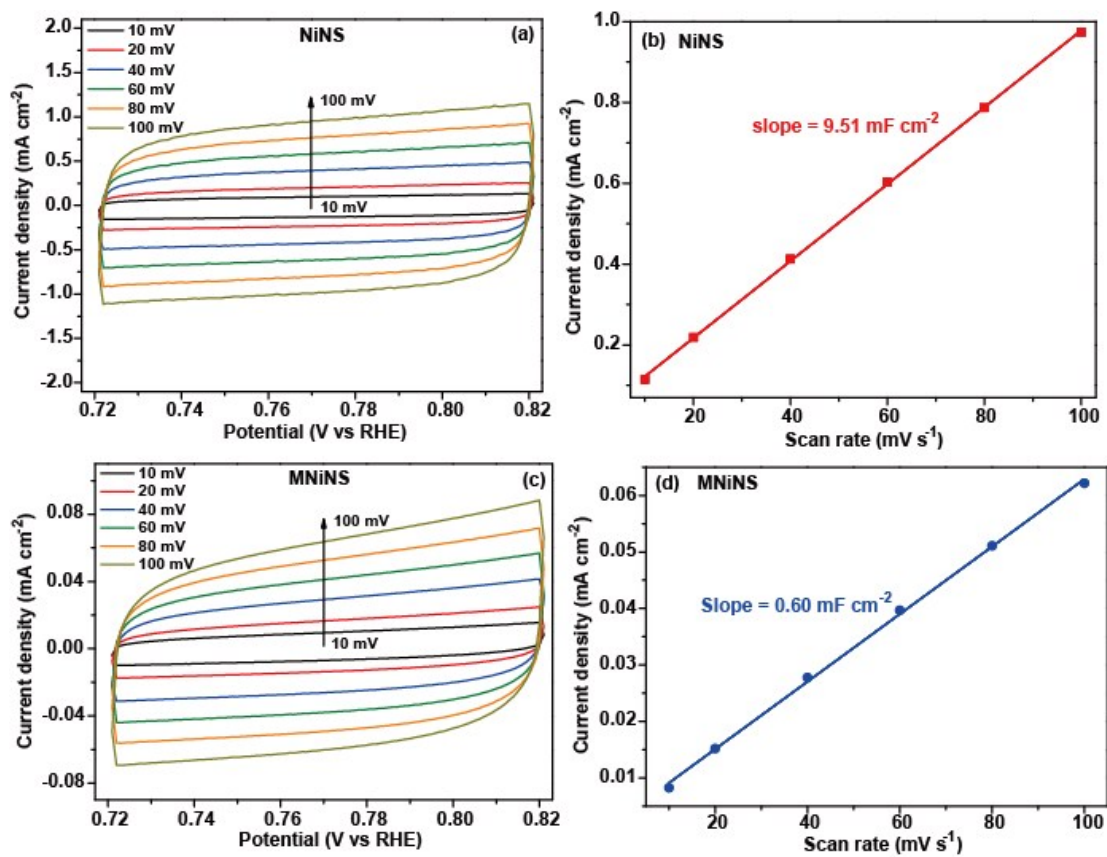
**Fig. S7** The double-layer region with scan rates ranging from 10 to 100 mV s$^{-1}$ in 1.0 M KOH for (a) NiNS and (c) MNiNS. Charging current density with different scan rates for (b) NiNS and (d) MNiNS.

**Table S1** Element analysis of NiNS, $Ni_3N$ and $Ni_3S_2$

|  | Nickel (wt.%)[1] | Nitrogen (wt.%) | Sulfur (wt.%) |
|---|---|---|---|
| NiNS | 87.18 | 4.17 | 8.65 |

[1]By difference

**Table S2** HER performance comparison between NiNS and recently reported electrocatalysts in alkaline media

| Electrocatalysts | Electrolyte | $j$, mA cm$^{-2}$ | $\eta$ required, mV | Tafel slop, mV dec$^{-1}$ | Reference |
|---|---|---|---|---|---|
| NiNS | 1.0 M KOH | 100 | 197 |  | This work |
| $Ni_3N$-Co | 1.0 M KOH | 100 | 290 | 156 | S2 |
| $NiMoN/Ni_3N$ on carbon cloth | 1.0 M KOH | 100 | 200 | 64 | S3 |
| $Ni_2P$@NPCNFs | 1.0 M KOH | 100 | 205 | 79.7 | S4 |
| $Ni_xCo_{3-x}S_4/Ni_3S_2$/NF | 1.0 M KOH | 100 | 258 | 107 | S5 |
| $Co_3Se_4$ nanowires on Co foam | 1.0 M KOH | 100 | 262 | 72 | S6 |
| 200-SMN/NF | 1.0 M KOH | 100 | 287 | 72.9 | S7 |
| $Pr_{0.5}(Ba_{0.5}Sr_{0.5})_{0.5}Co_{0.8}Fe_{0.2}O_{3-\delta}$ | 1.0 M KOH | 100 | 310 | 45 | S8 |
| $NiCo_2O_4$ nanowire arrays on nickel foam | 1.0 M KOH | 100 | 275 | 88 | S9 |
| $NiCo_2O_4$ hollow microcuboids | 1.0 M NaOH | 100 | 245 | 49.7 | S10 |
| $Ni_3N$ nanosheets on carbon cloth | 1.0 M KOH | 100 | 470 | N/A | S11 |

**Table S3** OER performance comparison between NiNS and recently reported electrocatalysts in alkaline media

| Electrocatalysts | Electrolyte | $j$, mA cm$^{-2}$ | $\eta$ required, mV | Tafel slop, mV dec$^{-1}$ | Reference |
|---|---|---|---|---|---|
| NiNS | 1.0 M KOH | 100 | 404 | | This work |
| MoS$_2$/NiS NCs | 1.0 M KOH | 100 | ~475 | 53 | S12 |
| NCP/G NSs | 1.0 M KOH | 100 | 400 | 65.9 | S13 |
| NF@Ni/C-600 | 1.0 M KOH | 100 | ~460 | 54 | S14 |
| Ni$_3$S$_2$/NF-2 | 1.0 M KOH | 100 | 425 | N/A | S15 |
| Fe$_1$-(Co$_3$O$_4$)$_{10}$ holy nanosheets | 1.0 M KOH | 100 | ~410 | 55 | S16 |
| NiCo$_2$O$_4$@CoMoO$_4$/NF-7 | 1.0 M KOH | 100 | ~510 | 102 | S17 |
| Ni-Mo$_x$C/NC-100 | 1.0 M KOH | 100 | 470 | 74 | S18 |
| NiSe-Ni$_{0.85}$Se/CP | 1.0 M KOH | 100 | 420 | 75 | S19 |
| NiMoN-NF700 | 1.0 M KOH | 100 | ~405 | 54 | S20 |
| NiCo$_2$O$_4$ nanowire arrays | 1.0 M KOH | 100 | 470 | 66.9 | S9 |

**Reference**

[S1] K. Xu, P. Chen, X. Li, Y. Tong, H. Ding, X. Wu, W. Chu, Z. Peng, C. Wu,Y. Xie, *J. Am. Chem. Soc.* **2015,** *137*, 4119.

[S2] C. Zhu, A.-L. Wang, W. Xiao, D. Chao, X. Zhang, N. H. Tiep, S. Chen, J. Kang, X. Wang, J. Ding, J. Wang, H. Zhang, H. J. Fan, *Adv. Mater.* **2018,** *30*, 1705516.

[S3] A. Wu, Y. Xie, H. Ma, C. Tian, Y. Gu, H. Yan, X. Zhang, G. Yang, H. Fu, *Nano Energy* **2018,** *44*, 353.

[S4] M.-Q. Wang, C. Ye, H. Liu, M. Xu, S.-J. Bao, *Angew. Chem., Int. Ed.* **2018,** *57*, 1963.

[S5] Y. Wu, Y. Liu, G.-D. Li, X. Zou, X. Lian, D. Wang, L. Sun, T. Asefa, X. Zou, *Nano Energy* **2017,** *35*, 161.

[S6] W. Li, X. Gao, D. Xiong, F. Wei, W.-G. Song, J. Xu, L. Liu, *Adv. Energy Mater.* **2017**, 7, 1602579.

[S7] Z. Cui, Y. Ge, H. Chu, R. Baines, P. Dong, J. Tang, Y. Yang, P. M. Ajayan, M. Ye, J. Shen, *J. Mater. Chem. A* **2017,** *5*, 1595.

[S8] X. Xu, Y. Chen, W. Zhou, Z. Zhu, C. Su, M. Liu, Z. Shao, *Adv. Mater.* **2016,** *28*, 6442.

[S9] A. Sivanantham, P. Ganesan,S. Shanmugam, *Adv. Funct. Mater.* **2016,** *26*, 4661.

[S10]    X. Gao, H. Zhang, Q. Li, X. Yu, Z. Hong, X. Zhang, C. Liang, Z. Lin, *Angew. Chem., Int. Ed.* **2016,** *55*, 6290.

[S11]    D. Gao, J. Zhang, T. Wang, W. Xiao, K. Tao, D. Xue, J. Ding, *J. Mater. Chem. A* **2016,** *4*, 17363.

[S12]    Z. Zhai, C. Li, L. Zhang, H.-C. Wu, L. Zhang, N. Tang, W. Wang, J. Gong, *J. Mater. Chem. A* **2018,** *6*, 9833.

[S13]    J. Tian, J. Chen, J. Liu, Q. Tian, P. Chen, *Nano Energy* **2018,** *48*, 284.

[S14]    H. Sun, Y. Lian, C. Yang, L. Xiong, P. Qi, Q. Mu, X. Zhao, J. Guo, Z. Deng, Y. Peng, *Energy. Environ. Sci.* **2018,** *11*, 2363.

[S15]    G. Liu, Z. Sun, X. Zhang, H. Wang, G. Wang, X. Wu, H. Zhang, H. Zhao, *J. Mater. Chem. A* **2018,** *6*, 19201.

[S16]    Y. Li, F.-M. Li, X.-Y. Meng, X.-R. Wu, S.-N. Li, Y. Chen, *Nano Energy* **2018,** *54*, 238.

[S17]    Y. Gong, Z. Yang, Y. Lin, J. Wang, H. Pan, Z. Xu, *J. Mater. Chem. A* **2018,** *6*, 16950.

[S18]    D. Das, S. Santra, K. K. Nanda, *ACS Appl. Mater. Interfaces* **2018,** *10*, 35025.

[S19]    Y. Chen, Z. Ren, H. Fu, X. Zhang, G. Tian, H. Fu, *Small* **2018,** *14*, 1800763.

[S20]    B. Chang, J. Yang, Y. Shao, L. Zhang, W. Fan, B. Huang, Y. Wu, X. Hao, *ChemSusChem* **2018,** *11*, 3198.

# Chapter 5 Non-metal Single Iodine Atom Electrocatalysts for the Hydrogen Evolution Reaction

## 5.1 Introduction and Significance

Single-atom catalysts (SACs) are attractive for various reactions because of their unique properties. However, common metal-based SACs require the complex synthesis processes. While non-metal SACs have been rarely reported, their preparation via simple methods is highly desirable. Here, a single atom nickel iodide (SANi-I) with uniformly dispersed non-metal single atom iodines was prepared via a simple calcination process in a vacuum-sealed ampoule and subsequent cyclic voltammetry (CV) activation in alkaline solution. Aberration-corrected high-angle annular dark-field scanning transmission electron microscopy (HAADF-STEM) and synchrotron-based X-ray absorption spectroscopy (XAS) were applied to confirm the atomic-level dispersion of iodine atoms and detailed structure of the SACs. *In-situ* Raman spectroscopy was used to explore the HER mechnism via characterizing the formation of single iodine atom - adsorbed hydrogen atom (I-$H_{ads}$) intermediates. The highlights of this work include:

- A simple one-step calcination process in a vacuum-sealed ampoule was applied to synthesize the nickel iodide (Ni-I) precursor, which was subsequently activated via CV scanning in alkaline solution to obtain SANi-I.

- Aberration-corrected HAADF-STEM confirmed the atomic-level dispersion of iodine atoms. Synchrotron-based XAS revealed that iodine atoms were bonded to oxygen and nickel atoms, indicating that SANi-I was formed after the majority of the iodine atoms in the Ni-I precursor were replaced by oxygen atoms and hydroxide ions.

- *In-situ* Raman spectroscopy was implemented on highly active SANi-I to study the HER mechanism. Clear I-$H_{ads}$ signals were observed, indicating that efficient dissociative adsorption of water molecules occurs at single iodine atoms.

- A 100 mA cm$^{-2}$ current density is achieved for SANi-I at an overpotential of 60 mV, which is lower than that for benchmark Pt/C (61 mV) in 1.0 M KOH. A two-

electrode electrolyzer in 1.0 M KOH was established by integration of Ir/C loaded on Ni foam as the anode and SANi-I or Pt/C loaded Ni foam as the cathode (Ir-C//SANi-I and Ir-C//Pt-C, respectively), in which the current density achieved at a potential of 1.8 V for Ir-C//SANi-I is 408 mA cm$^{-2}$, higher than that for Ir-C//Pt-C (154 mA cm$^{-2}$).

## 5.2 Non-metal Single Iodine Atom Electrocatalysts for the Hydrogen Evolution Reaction

This chapter is included as it appears as a journal paper by Yongqiang Zhao, Tao Ling, Shuangming Chen, Bo Jin, Anthony Vasileff, Yan Jiao, Li Song, Jun Luo and Shi-Zhang Qiao, *Angewandte Chemie International Edition* 2019, DOI: 10.1002/anie.201905554.

# Statement of Authorship

| Title of Paper | Non-metal Single Iodine Atom Electrocatalysts for the Hydrogen Evolution Reaction |
|---|---|
| Publication Status | ☑ Published      ☐ Accepted for Publication<br><br>☐ Submitted for Publication      ☐ Unpublished and Unsubmitted work written in manuscript style |
| Publication Details | Yongqiang Zhao, Tao Ling, Shuangming Chen, Bo Jin, Anthony Vasileff, Yan Jiao, Li Song, Jun Luo and Shi-Zhang Qiao, Angewandte Chemie International Edition 2019, 58, 2-8. |

## Principal Author

| Name of Principal Author (Candidate) | Yongqiang Zhao | | |
|---|---|---|---|
| Contribution to the Paper | Research plan, material synthesis, most of the characterizations and data analysis, electrochemical measurements and manuscript drafting. | | |
| Overall percentage (%) | 70 | | |
| Certification: | This paper reports on original research I conducted during the period of my Higher Degree by Research candidature and is not subject to any obligations or contractual agreements with a third party that would constrain its inclusion in this thesis. I am the primary author of this paper. | | |
| Signature | | Date | 21/05/2019 |

## Co-Author Contributions

By signing the Statement of Authorship, each author certifies that:

    i.      the candidate's stated contribution to the publication is accurate (as detailed above);

    ii.      permission is granted for the candidate in include the publication in the thesis; and

    iii.      the sum of all co-author contributions is equal to 100% less the candidate's stated contribution.

| Name of Co-Author | Tao Ling | | |
|---|---|---|---|
| Contribution to the Paper | 6%. Assistance with TEM characterization, data analysis and manuscript revision. | | |
| Signature | | Date | 21/05/2019 |

| Name of Co-Author | Shuangming Chen | | |
|---|---|---|---|
| Contribution to the Paper | 6%. Assistance with Synchrotron-based XAS characterization, data analysis and manuscript revision. | | |
| Signature | | Date | 21st May. 2019 |

| Name of Co-Author | Bo Jin | | |
|---|---|---|---|
| Contribution to the Paper | 2%. Discussion of research plan, data analysis and manuscript revision. | | |
| Signature | | Date | 1.05.2019 |

| Name of Co-Author | Anthony Vasileff | | |
|---|---|---|---|
| Contribution to the Paper | 3%. Assistance with *in-situ* Raman test, data analysis and manuscript revision. | | |
| Signature | | Date | 21. 05. 2019. |

| Name of Co-Author | Yan Jiao | | |
|---|---|---|---|
| Contribution to the Paper | 1%. Data analysis. | | |
| Signature | | Date | 21 May 2019 |

| Name of Co-Author | Li Song | | |
|---|---|---|---|
| Contribution to the Paper | 1%. Data analysis. | | |
| Signature | | Date | 21-May-2019 |

| Name of Co-Author | Jun Luo | | |
|---|---|---|---|
| Contribution to the Paper | 1%. Data analysis. | | |
| Signature | | Date | 21.05.2019 |

| Name of Co-Author | Shi-Zhang Qiao | | |
|---|---|---|---|
| Contribution to the Paper | 10%. Supervision of the work, data interpretation and manuscript evaluation. | | |
| Signature | | Date | 21.05.2019 |

*Hydrogen Evolution Reaction*

# Non-metal Single-Iodine-Atom Electrocatalysts for the Hydrogen Evolution Reaction

*Yongqiang Zhao+, Tao Ling+, Shuangming Chen+, Bo Jin, Anthony Vasileff, Yan Jiao, Li Song, Jun Luo, and Shi-Zhang Qiao\**

*Abstract: Common-metal-based single-atom catalysts (SACs) are quite difficult to design due to the complex synthesis processes required. Herein, we report a single-atom nickel iodide (SANi-I) electrocatalyst with atomically dispersed non-metal iodine atoms. The SANi-I is prepared via a simple calcination step in a vacuum-sealed ampoule and subsequent cyclic voltammetry activation. Aberration-corrected high-angle annular dark-field scanning transmission electron microscopy and synchrotron-based X-ray absorption spectroscopy are applied to confirm the atomic-level dispersion of iodine atoms and detailed structure of SANi-I. Single iodine atoms are found to be isolated by oxygen atoms. The SANi-I is structural stable and shows exceptional electrocatalytic activity for the hydrogen evolution reaction (HER). In situ Raman spectroscopy reveals that the hydrogen adatom ($H_{ads}$) is adsorbed by a single iodine atom, forming the $I$-$H_{ads}$ intermediate, which promotes the HER process.*

## Introduction

Single-atom catalysts (SACs) have drawn significant attention owing to their maximum atom utilization efficiency, remarkable catalytic activity, and superior reaction selectiv-

ity.[1–4] They exhibit great potential in electrocatalytic energy conversion processes including the oxygen reduction reaction (ORR),[5,6] hydrogen evolution reaction (HER),[7,8] $CO_2$ reduction reaction ($CO_2RR$)[9,10] and nitrogen reduction reaction (NRR).[11,12] Various synthetic strategies have been developed to obtain SACs, including atomic layer deposition,[13] coordination development,[14] defect engineering[15] and spatial confinement.[16] However, they generally require costly and tedious synthesis processes which is unfavorable for practical application. Furthermore, the majority of SACs are metal-based, such as Pt SACs,[17,18] Ru SACs,[19,20] Cu SACs,[21,22] and Co SACs.[23,24] To our knowledge, non-metal-based SACs have never been reported. Therefore, the development of non-metal SACs using simple techniques and their application in electrocatalysis is particularly desirable for the field.

Typically, the HER process in alkaline media undergoes Volmer ($H_2O + e^- \rightarrow H_{ads} + OH^-$)—Tafel ($2\,H_{ads} \rightarrow H_2$) or Heyrovsky ($H_2O + e^- + H_{ads} \rightarrow H_2 + OH^-$) steps,[25] where $H_{ads}$ refers to an adsorbed hydrogen atom. The initial Volmer step is crucial for the entire process as the dissociative adsorption of $H_2O$ and subsequent cleavage of O−H bonds to form $H_{ads}$ on the active sites takes place. Therefore, it is desirable to characterize the in situ formation of E-$H_{ads}$ (E refers to the active site) intermediate to explore the HER mechanism in alkaline media. The S-$H_{ads}$ (where S is sulfur) intermediate was observed via in situ Raman spectroscopy on $Ni_3S_2$ based electrocatalysts at −0.477 V (vs. the reversible hydrogen electrode (RHE)).[26] An ideal electrocatalyst for the in situ characterization of the E-$H_{ads}$ intermediate should exhibit response to the formation of the intermediate at relatively low overpotential, which requires high electrocatalytic activity. Consequently, in situ characterization of the E-$H_{ads}$ intermediate on electrocatalysts with remarkable activity is significant for the study of the HER mechanism.

Herein, we report the preparation of a single atom nickel iodide (SANi-I) electrocatalyst with atomically dispersed iodine atoms and explore its HER mechanism. Nickel iodide (Ni-I) precursor was synthesized by a simple calcination step in a vacuum-sealed ampoule. SANi-I was formed after the excess iodine atoms in Ni-I were replaced by oxygen atoms and hydroxide ions during cyclic voltammetry scanning in alkaline solution. Aberration-corrected high-angle annular dark-field scanning transmission electron microscopy (HAADF-STEM) study reveals the atomic-level dispersion of iodine. Synchrotron-based X-ray absorption spectroscopy (XAS) reveals that iodine atoms were isolated by oxygen, forming I−O bonds. In situ Raman spectra of SANi-I under

[*] Y. Q. Zhao,[+] Prof. B. Jin, A. Vasileff, Dr. Y. Jiao, Prof. S. Z. Qiao
Center for Materials in Energy and Catalysis, School of Chemical Engineering and Advanced Materials
The University of Adelaide
Adelaide, SA 5005 (Australia)
E-mail: s.qiao@adelaide.edu.au

Prof. T. Ling,[+] Prof. S. Z. Qiao
Key Laboratory for Advanced Ceramics and Machining Technology of Ministry of Education, Tianjin Key Laboratory of Composite and Functional Materials, School of Materials Science and Engineering, Tianjin University
Tianjin 300072 (China)

Prof. S. Chen,[+] Prof. L. Song
Hefei National Laboratory of Physical Sciences at the Microscale, National Synchrotron Radiation Laboratory, CAS Center for Excellence in Nanoscience, University of Science and Technology of China
Hefei 230029 (China)

Prof. J. Luo
Tianjin Key Laboratory of Advanced Functional Porous Materials and Center for Electron Microscopy, School of Materials Science and Engineering, Tianjin University of Technology
Tianjin 300384 (China)

[+] These authors contributed equally to this work.

📄 Supporting information and the ORCID identification number(s) for
🔾 the author(s) of this article can be found under:
https://doi.org/10.1002/anie.201905554.

▮▮▮▮ **Wiley Online Library**
◤◤

These are not the final page numbers!

© 2019 Wiley-VCH Verlag GmbH & Co. KGaA, Weinheim

*Angew. Chem. Int. Ed.* **2019**, *58*, 2–8

75

HER conditions shows the presence of $H_{ads}$ on iodine atoms with the observation of I-$H_{ads}$ vibrational bands. This suggests that the iodine atoms expedite the dissociative adsorption of water. Experimental results show that SANi-I exhibits good electrocatalytic activity and stability in alkaline media for the HER. The novel design and fabrication of SANi-I provide a promising pathway for electrolytic $H_2$ production.

## Results and Discussion

The Ni-I was prepared by the one-step calcination of nickel foam with ground iodine powder in a vacuum sealed ampoule (see Experimental Section in the Supporting Information). During the calcination, the vaporized iodine, which was encapsulated by the ampoule, reacted with the nickel foam to form nickel iodide. Scanning electron microscopy (SEM) and energy dispersive spectra (EDS) revealed that the Ni-I precursor consisted of bulk nickel iodide with uniformly distributed nickel (20.1 wt%) and iodine (79.9 wt%) (Figure S1, Supporting Information). The transmission electron microscopy (TEM), high resolution TEM (HRTEM) and selective area electron diffraction (SAED) images show that Ni-I possessed high crystallinity (Figure S2, Supporting Information). The Ni-I precursor was subsequently activated in KOH solution via cyclic voltammetry, obtaining SANi-I. During the activation process, the majority of the iodine atoms in Ni-I were replaced by oxygen atoms and hydroxide ions. The aberration-corrected HAADF-STEM image of SANi-I confirms that iodine atoms were atomically dispersed (Figure 1a) and the ring-like SAED pattern depicts its low crystallinity (inset of Figure 1a). The SANi-I consisted of bulk nickel hydroxide clusters (Figure 2a) with 1.2 wt% iodine (Figure S3, Supporting Information). HAADF-STEM-EDS line scan and mapping analysis reveal homogenous spatial distribution of Ni, I, and O over the marked detection range of SANi-I (Figure 1b). Homogeneously dispersed single iodine atoms can be clearly observed from the different intensity profiles (Figure S4, Supporting Information). SANi-I after 96 h stability test (SANi-I96) was also studied and details can be found in Experimental Procedures in the Supporting Information. The morphology and elemental composition of SANi-I96 remained unchanged (Figure S5, Supporting Information). The iodine atoms in SANi-I96 were also homogenously dispersed (Figure 1c) and SANi-I96 maintained low crystallinity (inset of Figure 1c) and elemental distribution (Figure 1d). The above results strongly support the successful activation of Ni-I, forming highly stable SANi-I.

Commercial nickel iodide (C-NiI$_2$) was loaded on nickel foam and activated to obtain activated nickel hydroxide (A-Ni-OH) for comparison. C-NiI$_2$ possessed similar morphology and elemental composition to Ni-I (Figure S6, Supporting Information). A-Ni-OH consisted of bulk nickel hydroxide clusters with no iodine detected (Figure S7, Supporting Information).

X-ray diffraction (XRD) was performed to study the crystal structure. The XRD pattern of Ni-I corresponds well with the standard powder diffraction file (Figure S8a, Sup-
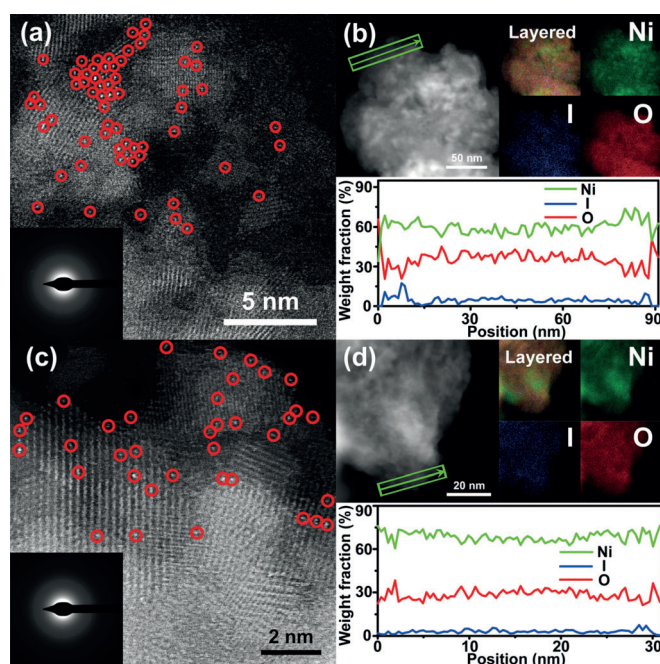


**Figure 1.** Magnified HAADF-STEM image and (inset) corresponding SAED pattern of a) SANi-I and c) SANi-I96. Red circles are used to highlight single iodine atoms. HAADF-STEM image and corresponding mapping images and line-scanning profile (along the highlighted green line) of Ni, I, and O for b) SANi-I and d) SANi-I96.
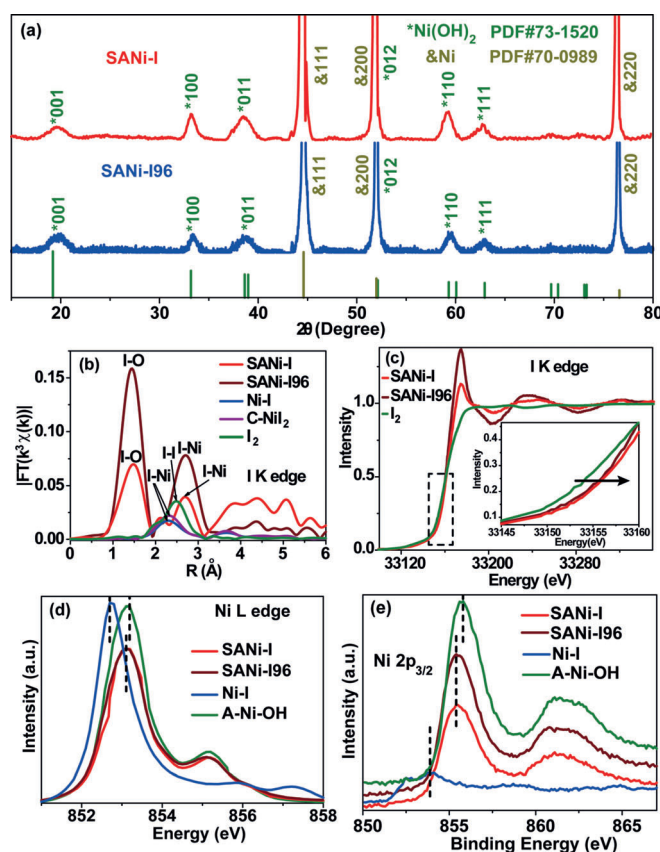


**Figure 2.** a) XRD patterns of SANi-I and SANi-I96. b) K$^3$-weighted χ (k) function of EXAFS spectra. c) Iodine K edge XANES spectra and (insert) enlarged absorption-edge. d) Nickel L edge XANES spectra. e) XPS spectra of Ni 2p$_{3/2}$.

porting Information). No peaks related to nickel iodide were observed for SANi-I (Figure 2 a), which is consistent with the EDS spectra and HAADF-STEM-EDX line scan and mapping analysis. This indicates that SANi-I did not possess an ordered nickel-iodine structure. The HAADF-STEM image and XRD pattern of SANi-I reveal that after activation, the bulk of Ni-I was converted to nickel hydroxide and single iodine atoms were uniformly dispersed on the nickel hydroxide support. It is interesting to note that SANi-I96 retained its crystal structure. Peaks of nickel iodide hexahydrate are observed for C-NiI$_2$ (Figure S8 b, Supporting Information) while, after activation, C-NiI$_2$ was converted to A-Ni-OH with predominantly nickel hydroxide and partially nickel oxide (Figure S8 c, Supporting Information).

Synchrotron-based extended X-ray absorption fine structure spectroscopy (EXAFS) was employed to elucidate detailed structural information for SANi-I. The EXAFS spectra of R space exhibit I−O coordination at 1.47 Å for SANi-I and 1.45 Å for SANi-I96,[27] and I−Ni coordination at 2.70 Å for SANi-I and SANi-I96 (Figure 2 b), indicating the robust structural stability of SANi-I. No I−I coordination (2.50 Å) was observed for SANi-I or SANi-I96, suggesting the absence of elemental iodine in SANi-I and SANi-I96. For SANi-I96, the I-O and I-Ni peaks have higher intensity, indicating a different I-O and I-Ni coordination environment (Table S1, Supporting Information). For Ni-I and C-NiI$_2$, no I-O characteristic peak was detected. The EXAFS fitting results are illustrated in Figure S9, Supporting Information. Figure 2 c shows synchrotron-based X-ray absorption near-edge structure (XANES) spectra of SANi-I, SANi-I96 and elemental iodine. The absorption-edge of SANi-I and SANi-I96 shifts toward higher energy compared with elemental iodine (inset of Figure 2 c), revealing that the charge state of iodine for SANi-I and SANi-I96 was higher than that for elemental iodine. This can be attributed to electron transfer from the iodine atoms to adjacent oxygen atoms. The XANES spectra of Ni-I and C-NiI$_2$ are shown in Figure S10, Supporting Information. From the above results, it is clear that during activation, oxygen atoms were inserted between the nickel and iodine atoms, forming I−O bonds. Therefore, the iodine atoms were isolated by oxygen and formed single iodine sites. Additionally, nickel L-edge XANES spectra show that the peak for SANi-I or SANi-I96 locates between that for Ni-I and A-Ni-OH (Figure 2 d), revealing that the nickel charge state for SANi-I and SANi-I96 was situated between that for Ni-I and A-Ni-OH.[28] X-ray photoelectron spectroscopy (XPS) was used to study the chemical valence states of the samples. For SANi-I96, the iodine 3d$_{5/2}$ peak is at 624.0 eV (Figure S11, Supporting Information), which is higher than that for Ni-I (619.0 eV) and C-NiI$_2$ (619.2 eV), suggesting a higher charge state of iodine.[29] This observation agrees with the XANES spectra. Ni 2p$_{3/2}$ XPS spectra show that the peak for SANi-I and SANi-I96 locates between that for Ni-I and A-Ni-OH (Figure 2 e), which agrees with the XANES spectra. These results indicate that electron transfer occurs in Ni-I-O for SANi-I, leading to a high

charge state on the iodine (compared with Ni-I) and a moderate charge state on the nickel (compared with Ni-I and A-Ni-OH).

From the aforementioned discussion, it is clear that SANi-I with atomically dispersed iodine atoms predominantly consists of nickel hydroxide. Unlike non-metal doping in which a small amount of non-metal dopants are intentionally introduced into host materials, SANi-I was formed after predominant iodine atoms were replaced by oxygen atoms and hydroxide ions. We propose that 1) iodine single atoms are located at the interface between the nickel support and the in situ grown Ni-I precursor, where nickel atoms and iodine atoms are chemically bonded; 2) the nickel hydroxide support was formed by the reaction between nickel and hydroxide ions. Different from Ni-I (Figure S12 a, Supporting Information), no ordered nickel-iodine structure is observed in SANi-I. Single iodine atoms are bonded to nickel and oxygen atoms and uniformly dispersed on the nickel hydroxide support (Figure S12 b, Supporting Information).

SANi-I was then applied as an electrocatalyst for the HER to evaluate its performance as a non-metal single atom catalyst. The HER activity of SANi-I was assessed by directly using SANi-I as the working electrode in Ar-saturated 1.0 M KOH solution in a three-electrode cell. A-Ni-OH, Pt-C loaded on Ni foam (Pt-C/Ni) and bare Ni foam were also prepared to evaluate their HER electrocatalytic performance for comparison. The linear sweep voltammetry (LSV) curve demonstrates that SANi-I exhibited substantially high electrocatalytic activity (Figure 3 a). A 100 mA cm$^{-2}$ current density was achieved at an overpotential of 60 mV, which was lower than those for Pt-C (61 mV) and A-Ni-OH (285 mV). Since the nickel hydroxide in our study exhibits inferior electrocatalytic performance, the superior HER performance of SANi-I is attributed to atomically dispersed iodine atoms. A comparative summary of the electrocatalytic
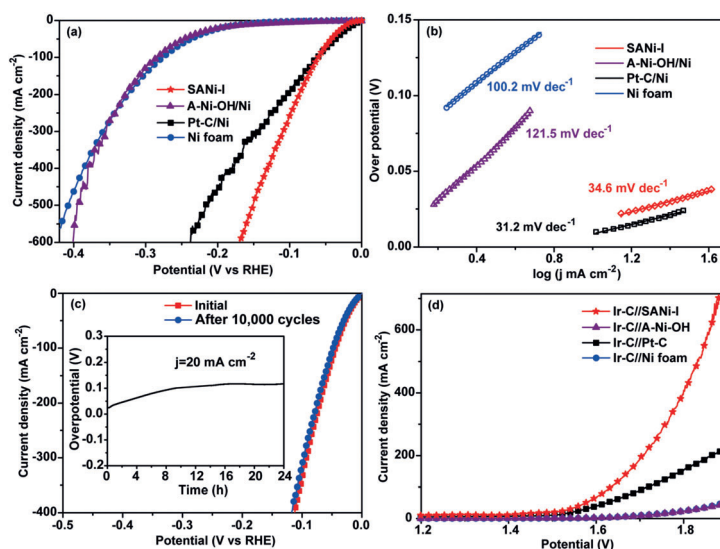


***Figure 3.*** a) HER performance of SANi-I, A-Ni-OH, Pt-C/Ni and Ni foam. b) Corresponding Tafel plots with associated linear fittings. c) Cycle stability of SANi-I and (inset) time-dependent overpotential of SANi-I under constant current density without iR correction. d) Overall water splitting electrocatalytic activity of Ir-C//SANi-I, Ir-C//A-Ni-OH, Ir-C//Pt-C and Ir-C//Ni foam.

performance of state-of-the-art HER electrocatalysts in recent reports is presented in Table S2, Supporting Information. SANi-I demonstrated favorable electrocatalytic activity among most active non-noble metal based electrocatalysts, such as nickel phosphide nanoparticles in N-doped porous carbon nanofibers (205 mV),[30] NiFe layered double hydroxide nanosheet shells on Cu nanowire cores (192 mV),[31] $SrCo_{0.85}Fe_{0.1}P_{0.05}O_{3-\delta}$ nanofilm deposited onto nickel foam (260 mV),[32] indicating the potential practical value of this catalyst.

The HER kinetics for these electrodes was assessed by Tafel plots (Figure 3b). The Tafel slope for SANi-I was $34.6 \, mV \, dec^{-1}$, which is comparable to that of Pt-C/Ni and is smaller than that of A-Ni-OH ($121.5 \, mV \, dec^{-1}$), indicating faster HER kinetics for SANi-I and a different rate limiting step. A Tafel slope close to $30 \, mV \, dec^{-1}$ suggests that the HER on SANi-I might have proceeded via a Volmer—Tafel mechanism with the Tafel step being rate limiting. Electrochemical impedance spectroscopy (EIS) was applied to further analyze the HER kinetics (Figure S13, Supporting information). The calculated resistance of SANi-I ($5.9 \, \Omega$) is significantly lower than that of A-Ni-OH ($25.5 \, \Omega$), indicating more rapid charge transfer within SANi-I.

The electrochemical active surface areas (ECSA) of SANi-I and A-Ni-OH were measured by calculating the electrochemical double-layer capacitance ($C_{dl}$) to obtain insight into electrocatalytic sites. SANi-I possessed a $C_{dl}$ of $607.13 \, mF \, cm^{-2}$ (Figure S14, Supporting information), which was much higher than that of A-Ni-OH ($5.53 \, mF \, cm^{-2}$). This indicates that SANi-I had abundant electrocatalytic active sites, which we attribute to the atomic-level dispersion of iodine atoms and adjacent nickel atoms with moderate charge state.

SANi-I showed remarkable stability during HER testing. The LSV curve of SANi-I for the HER after 10000 potential cycles was similar to the initial one (Figure 3c), with negligible loss of cathodic current. SANi-I also exhibited good long-term operating stability at $20 \, mA \, cm^{-2}$ (inset of Figure 3c) during chronopotentiometry. The overpotential exhibits an initial increase without significant variation from the 8th h to the 24th h, suggesting good durability under the testing conditions. Chronoamperometry at a constant potential of $-0.06 \, V$ (vs. RHE) was also applied to measure the stability of SANi-I. In each chronoamperometric test, the current density exhibits an initial decrease without significant variation from the 4th h to the 24th h (Figure S15a, Supporting Information). However, the LSV curves of SANi-I for the HER after four 24 h chronoamperometric tests are similar to the initial one (Figure S15b, Supporting Information), indicating its excellent stability.

Based on current studies, it can be reasonably anticipated that SANi-I acts as a highly efficient electrocatalyst for practical $H_2$ production. Therefore, a two-electrode electrolyzer in 1.0 M KOH was established overall water electrolysis by integrating Ir-C loaded on Ni foam and SANi-I as the anode and cathode, respectively (denoted as Ir-C//SANi-I). Ir-C/A-Ni-OH, Ir-C//Pt-C and Ir-C//Ni foam were also

prepared for comparison. The LSV curves of Ir-C//SANi-I, Ir-C// A-Ni-OH, Ir-C//Pt-C and Ir-C//Ni foam for overall water splitting demonstrate that Ir-C//SANi-I exhibited the highest electrocatalytic activity (Figure 3d). The current density achieved at a potential of 1.8 V for Ir-C//SANi-I is $408 \, mA \, cm^{-2}$, higher than that for Ir-C//A-Ni-OH ($23 \, mA \, cm^{-2}$), Ir-C//Pt-C ($154 \, mA \, cm^{-2}$) and Ir-C//Ni foam ($24 \, mA \, cm^{-2}$).

To obtain a profound insight into the HER mechanism, in situ Raman spectroscopy was employed to study the reaction intermediates and possible role of single atom iodine in SANi-I (Figure 4). No peaks were detected on either SANi-
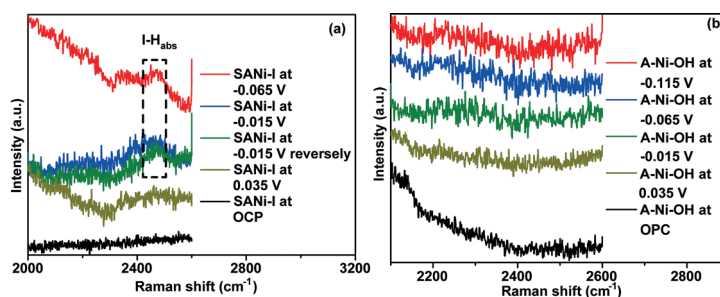


**Figure 4.** In situ Raman spectra of a) SANi-I and b) A-Ni-OH at OCP and constant potentials (vs. RHE).

I and A-Ni-OH when the samples were at open circuit potential (OCP). For SANi-I, no peak was detected at a potential of 0.035 V (vs. RHE), which is more positive than HER thermodynamic potential. A broad peak at approximately $2460 \, cm^{-1}$ was observed at a potential of $-0.015$ and $-0.065 \, V$ (vs. RHE) (Figure 4a), which is attributed to an I-H vibrational band.[33] The peak intensity increases when more negative potentials were applied (from $-0.015 \, V$ to $-0.065 \, V$ vs. RHE). When $-0.015 \, V$ (vs. RHE) was reversely applied to SANi-I, the I-H characteristic peak overlaps with the previous one. Therefore, the results suggest that an $I-H_{ads}$ intermediate was formed on the catalyst during the HER and is a pathway relevant intermediate.[34] For A-Ni-OH, no such peak was observed when potential was applied (Figure 4b). Therefore, the above experimental results demonstrate that the single iodine atoms can expedite water dissociation and H adsorption through $I-H_{ads}$ bond formation and enhance the HER kinetics.

From what has been discussed above, we propose that efficient dissociative adsorption of water molecules occurs at single iodine atom and adjacent nickel atom sites, where one hydrogen in the water molecule is adsorbed by a single iodine atom and the oxygen/hydroxide is cleaved onto the nickel atom (Figure S16, Supporting Information). Experimental evidence supports the existence of an $I-H_{ads}$ intermediate during the HER process. Therefore, it is reasonable to propose that efficient dissociative adsorption of water occurs in the Volmer step, leading to $I-H_{ads}$ intermediates and $OH^-$ adsorbed on the nickel.[35] Subsequently, two $H_{ads}$ atoms combine to form molecular hydrogen during a rate limiting Tafel step. It is possible that the moderate electronegativity of iodine (2.66 on the Pauling scale) grants a balanced hydrogen

adsorption and desorption. Additionally, since the electronegativity of iodine is smaller than that of oxygen (3.44 on the Pauling scale), the nickel atom in SANi-I possesses a moderate positive charge state, which is supported by the nickel XANES (Figure 2d) and XPS (Figure 2e) spectra. In addition, in situ Raman spectroscopy verified the formation of the I-H$_{ads}$ intermediate. Furthermore, previous studies confirmed that OH$^-$ can be adsorbed on nickel species through the strong interaction of the two parts.[35] Consequently, based on these experimental observations, it can be concluded that efficient dissociative water adsorption can occur on the synthesized electrocatalyst: hydrogen is adsorbed on single iodine atoms and OH$^-$ is adsorbed on the adjacent nickel species.[36]

## Conclusion

In summary, we developed a simple synthesis route to non-metal SAC catalyst (SANi-I) and explored its use as a highly efficient electrocatalyst for the HER. Atomically dispersed iodine and the structure of SANi-I were confirmed by HAADF-STEM and synchrotron-based XAS. The resultant SANi-I possessed superior structural stability and exhibited extraordinary electrocatalytic HER activity. The electrocatalytic mechanism was explored by in situ Raman spectroscopy which suggested that the single iodine atoms and adjacent nickel can accelerate the dissociative adsorption of water via the formation of the I-H$_{ads}$ intermediate. This work provides new opportunities for the development of SACs for advanced energy conversion.

## Acknowledgements

## Conflict of interest

The authors declare no conflict of interest.

[1] X.-F. Yang, A. Wang, B. Qiao, J. Li, J. Liu, T. Zhang, *Acc. Chem. Res.* **2013**, *46*, 1740–1748.

[2] C. Zhu, S. Fu, Q. Shi, D. Du, Y. Lin, *Angew. Chem. Int. Ed.* **2017**, *56*, 13944–13960; *Angew. Chem.* **2017**, *129*, 14132–14148.

[3] L. Liu, A. Corma, *Chem. Rev.* **2018**, *118*, 4981–5079.

[4] A. Wang, J. Li, T. Zhang, *Nat. Rev. Chem.* **2018**, *2*, 65–81.

[5] S. Yang, J. Kim, Y. J. Tak, A. Soon, H. Lee, *Angew. Chem. Int. Ed.* **2016**, *55*, 2058–2062; *Angew. Chem.* **2016**, *128*, 2098–2102.

[6] Q. Cheng, L. Yang, L. Zou, Z. Zou, C. Chen, Z. Hu, H. Yang, *ACS Catal.* **2017**, *7*, 6864–6871.

[7] N. Cheng, S. Stambula, D. Wang, M. N. Banis, J. Liu, A. Riese, B. Xiao, R. Li, T.-K. Sham, L.-M. Liu, G. A. Botton, X. Sun, *Nat. Commun.* **2016**, *7*, 13638.

[8] L. Zhang, L. Han, H. Liu, X. Liu, J. Luo, *Angew. Chem. Int. Ed.* **2017**, *56*, 13694–13698; *Angew. Chem.* **2017**, *129*, 13882–13886.

[9] C. Zhao, X. Dai, T. Yao, W. Chen, X. Wang, J. Wang, J. Yang, S. Wei, Y. Wu, Y. Li, *J. Am. Chem. Soc.* **2017**, *139*, 8078–8081.

[10] K. Jiang, S. Siahrostami, T. Zheng, Y. Hu, S. Hwang, E. Stavitski, Y. Peng, J. Dynes, M. Gangisetty, D. Su, K. Attenkofer, H. Wang, *Energy Environ. Sci.* **2018**, *11*, 893–903.

[11] H. Tao, C. Choi, L.-X. Ding, Z. Jiang, Z. Han, M. Jia, Q. Fan, Y. Gao, H. Wang, A. W. Robertson, S. Hong, Y. Jung, S. Liu, Z. Sun, *Chem* **2019**, *5*, 204–214.

[12] Z. Geng, Y. Liu, X. Kong, P. Li, K. Li, Z. Liu, J. Du, M. Shu, R. Si, J. Zeng, *Adv. Mater.* **2018**, *30*, 1803498.

[13] H. Yan, H. Cheng, H. Yi, Y. Lin, T. Yao, C. Wang, J. Li, S. Wei, J. Lu, *J. Am. Chem. Soc.* **2015**, *137*, 10484–10487.

[14] P. Chen, T. Zhou, L. Xing, K. Xu, Y. Tong, H. Xie, L. Zhang, W. Yan, W. Chu, C. Wu, Y. Xie, *Angew. Chem. Int. Ed.* **2017**, *56*, 610–614; *Angew. Chem.* **2017**, *129*, 625–629.

[15] J. Zhang, X. Wu, W.-C. Cheong, W. Chen, R. Lin, J. Li, L. Zheng, W. Yan, L. Gu, C. Chen, Q. Peng, D. Wang, Y. Li, *Nat. Commun.* **2018**, *9*, 1002.

[16] J. D. Kistler, N. Chotigkrai, P. Xu, B. Enderle, P. Prasertdham, C.-Y. Chen, N. D. Browning, B. C. Gates, *Angew. Chem. Int. Ed.* **2014**, *53*, 8904–8907; *Angew. Chem.* **2014**, *126*, 9050–9053.

[17] T. He, S. Chen, B. Ni, Y. Gong, Z. Wu, L. Song, L. Gu, W. Hu, X. Wang, *Angew. Chem. Int. Ed.* **2018**, *57*, 3493–3498; *Angew. Chem.* **2018**, *130*, 3551–3556.

[18] B. Zhang, H. Asakura, J. Zhang, J. Zhang, S. De, N. Yan, *Angew. Chem. Int. Ed.* **2016**, *55*, 8319–8323; *Angew. Chem.* **2016**, *128*, 8459–8463.

[19] C. Zhang, J. Sha, H. Fei, M. Liu, S. Yazdi, J. Zhang, Q. Zhong, X. Zou, N. Zhao, H. Yu, Z. Jiang, E. Ringe, B. I. Yakobson, J. Dong, D. Chen, J. M. Tour, *ACS Nano* **2017**, *11*, 6930–6941.

[20] Y. Guo, Y. Mei, K. Yuan, D.-J. Wang, H.-C. Liu, C.-H. Yan, Y.-W. Zhang, *ACS Catal.* **2018**, *8*, 6203–6215.

[21] Y. Qu, Z. Li, W. Chen, Y. Lin, T. Yuan, Z. Yang, C. Zhao, J. Wang, C. Zhao, X. Wang, F. Zhou, Z. Zhuang, Y. Wu, Y. Li, *Nat. Catal.* **2018**, *1*, 781–786.

[22] M. D. Marcinkowski, M. T. Darby, J. Liu, J. M. Wimble, F. R. Lucci, S. Lee, A. Michaelides, M. Flytzani-Stephanopoulos, M. Stamatakis, E. C. H. Sykes, *Nat. Chem.* **2018**, *10*, 325.

[23] H. Zhang, J. Wei, J. Dong, G. Liu, L. Shi, P. An, G. Zhao, J. Kong, X. Wang, X. Meng, J. Zhang, J. Ye, *Angew. Chem. Int. Ed.* **2016**, *55*, 14310–14314; *Angew. Chem.* **2016**, *128*, 14522–14526.

[24] X. Cui, J. Xiao, Y. Wu, P. Du, R. Si, H. Yang, H. Tian, J. Li, W.-H. Zhang, D. Deng, X. Bao, *Angew. Chem. Int. Ed.* **2016**, *55*, 6708–6712; *Angew. Chem.* **2016**, *128*, 6820–6824.

[25] Y. Jiao, Y. Zheng, M. Jaroniec, S. Z. Qiao, *Chem. Soc. Rev.* **2015**, *44*, 2060–2086.

[26] Y. Liu, S. Jiang, S. Li, L. Zhou, Z. Li, J. Li, M. Shao, *Appl. Catal. B* **2019**, *247*, 107–114.

[27] D. Laurencin, D. Vantelon, V. Briois, C. Gervais, A. Coulon, A. Grandjean, L. Campayo, *RSC Adv.* **2014**, *4*, 14700–14707.

[28] H. Wang, C. Y. Ralston, D. S. Patil, R. M. Jones, W. Gu, M. Verhagen, M. Adams, P. Ge, C. Riordan, C. A. Marganian, P. Mascharak, J. Kovacs, C. G. Miller, T. J. Collins, S. Brooker, P. D. Croucher, K. Wang, E. I. Stiefel, S. P. Cramer, *J. Am. Chem. Soc.* **2000**, *122*, 10544–10552.

[29] L. Li, C. Tang, B. Xia, H. Jin, Y. Zheng, S.-Z. Qiao, *ACS Catal.* **2019**, *9*, 2902–2908.

[30] M.-Q. Wang, C. Ye, H. Liu, M. Xu, S.-J. Bao, *Angew. Chem. Int. Ed.* **2018**, *57*, 1963–1967; *Angew. Chem.* **2018**, *130*, 1981–1985.

[31] L. Yu, H. Zhou, J. Sun, F. Qin, F. Yu, J. Bao, Y. Yu, S. Chen, Z. Ren, *Energy Environ. Sci.* **2017**, *10*, 1820–1827.

[32] G. Chen, Z. Hu, Y. Zhu, B. Gu, Y. Zhong, H.-J. Lin, C.-T. Chen, W. Zhou, Z. Shao, *Adv. Mater.* **2018**, *30*, 1804333.

[33] M. Grayson, *Internet Electron. J. Mol. Des.* **2005**, *4*, 786–792.

[34] Y. Deng, L. R. L. Ting, P. H. L. Neo, Y.-J. Zhang, A. A. Peterson, B. S. Yeo, *ACS Catal.* **2016**, *6*, 7790–7798.

[35] R. Subbaraman, D. Tripkovic, D. Strmcnik, K.-C. Chang, M. Uchimura, A. P. Paulikas, V. Stamenkovic, N. M. Markovic, *Science* **2011**, *334*, 1256–1260.

[36] X. Liu, Y. Jiao, Y. Zheng, K. Davey, S.-Z. Qiao, *J. Mater. Chem. A* **2019**, *7*, 3648–3654.

## Research Articles

Y. Q. Zhao, T. Ling, S. Chen, B. Jin,
A. Vasileff, Y. Jiao, L. Song, J. Luo,
S. Z. Qiao* ⎯⎯⎯⎯⎯⎯ ▮▮▮▮–▮▮▮▮

Non-metal Single-Iodine-Atom
Electrocatalysts for the Hydrogen
Evolution Reaction

● I ● Ni
● O ● H
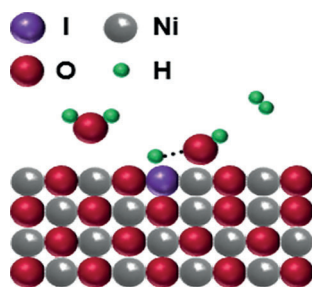
**Singled out**: A single-atom nickel iodide electrocatalyst is prepared. Aberration-corrected high-angle annular dark-field scanning transmission electron microscopy and synchrotron-based X-ray absorption spectroscopy are applied to study its structure. 100 mA cm$^{-2}$ is achieved at 60 mV for the HER and 408 mA cm$^{-2}$ at 1.8 V for overall water electrolysis.

▮▮▮▮
↖↖ **These are not the final page numbers!**

www.angewandte.org

© 2019 Wiley-VCH Verlag GmbH & Co. KGaA, Weinheim

*Angew. Chem. Int. Ed.* **2019**, *58*, 2 – 8

81

# Non-metal Single-Iodine-Atom Electrocatalysts for the Hydrogen Evolution Reaction

*Yongqiang Zhao[+], Tao Ling[+], Shuangming Chen[+], Bo Jin, Anthony Vasileff, Yan Jiao, Li Song, Jun Luo, and Shi-Zhang Qiao\**

## Experimental Procedures

***Chemicals:*** Nickel foam (thickness 1.6 mm, 95%), iodine (≥99.8%), nickel iodide powder (98%), nickel hydroxide (99%), potassium hydroxide (90%), and ethyl alcohol (anhydrous, ≥99.5%) were purchased from Sigma-Aldrich and used without further purification except for the nickel foam. Milli-Q water (18.2 M $\Omega$cm, PURELAB Option-Q) was used in all experiments. The nickel foams were washed with dilute HCl, acetone, ethanol and ultrapure water, and dried in vacuum at 298 K before use. The commercial Pt/C catalyst contains 20 wt% ~3 nm platinum nanoparticles.

***Synthesis of Nickel Iodide (Ni-I) precursor:*** The Ni-I electrode was fabricated by a facile one-step calcination of nickel foam with ground iodine powder in a vacuum sealed ampoule. In a typical synthesis, a pre-cleaned piece of Ni foam (20.65 mg, 1.5 cm × 0.3 cm × 1.6 cm, length × width × height) and I powder (51.63 mg) were sealed in ampoule under vacuum and then calcined at 500 °C for 5 h. Heating rate was 5 °C min$^{-1}$ and the cooling process took place naturally. The mass ratio of Ni foam and I powder was 1:2.5. The as-synthesized nickel iodide electrode was denoted as Ni-I. The Ni-I was washed by ethyl alcohol (anhydrous) before use. The loading of nickel iodide in Ni-I was calculated to be 63.57 mg.

***Synthesis of Single Atom Ni-I (SANi-I) electrode:*** The as-prepared Ni-I electrode was immersed in 1.0 M KOH and 80 segments of cyclic voltammetry (CV) were applied to the Ni-I electrode to yield SANi-I. The scan range was -0.6 to 0 V versus RHE at a scan rate of 100 mV s$^{-1}$. The as-prepared SANi-I was washed carefully several times by Milli-Q water and anhydrous alcohol and dried under vacuum at 25 °C. The calculated iodine loading is 0.48 mg cm$^{-2}$.

***Fabrication of Commercial Nickel Iodide Loaded Electrode (C-NiI$_2$):*** 200 mg of commercial nickel iodide was dispersed in 1 mL 2% Nafion aqueous solution, followed by sonication for 30 min to obtain a homogeneous catalyst solution. 160 μL of the catalyst ink was loaded on the surface of pre-cleaned Ni foam (surface area: 0.5 cm$^2$). The as-prepared C-NiI$_2$ electrode was dried at 40 °C under vacuum. The overall loading amount was 64 mg cm$^{-2}$.

***Synthesis of Activated nickel hydroxide (A-Ni-OH) Electrode:*** The as-prepared C-NiI$_2$ electrode was immersed in 1.0 M KOH and 80 segments of CV were applied to the C-NiI$_2$ electrode to yield A-Ni-OH. The scan range was -0.6 to 0 V versus RHE at a scan rate of 100 mV s$^{-1}$. The as-prepared A-Ni-OH was washed carefully several times with Milli-Q water and anhydrous alcohol and dried under vacuum at 25 °C.

***Fabrication of Pt-C and Ir-C Loaded Electrodes:*** 10 mg Pt/C or 8 mg Ir/C were dispersed in 1 mL 2% Nafion aqueous solution, followed by sonication for 30 min to obtain a homogeneous catalyst ink. 125

µL catalyst ink was loaded on the surface of pre-cleaned Ni foam (surface area: 0.5 cm$^2$). The as-prepared electrodes were dried at 40 °C under vacuum. The overall loading amount was 2.5 mg cm$^{-2}$ for the Pt/C electrode and 2 mg cm$^{-2}$ for the Ir/C electrode.

***96 h stability test***: The 96 h stability test was realized via four individual chronoamperometric HER tests whereby an overpotential of 60 mV was applied for 24 h. After each chronoamperometric operation, a cyclic voltammetry (CV) cycle was applied to regenerate SANi-I. Afterwards, an LSV was run to record the electrocatalytic activity of SANi-I after the chronoamperometric test and regeneration. The whole process was repeated four times. The single atom nickel iodide (SANi-I) after the 96 h stability test is denoted SANi-I96.

***Electrochemical measurements***: HER measurements were performed on a 760 E potentiostat (CH Instruments, Inc., USA) using a conventional three-electrode system with a graphite rod as the counter electrode and Ag/AgCl in 4 M KCl solution as the reference electrode. The current density was normalized to the geometrical surface area and the measured potentials versus Ag/AgCl were converted to the reversible hydrogen electrode (RHE) scale according to the Nernst equation:

$$E_{RHE} = E_{Ag/AgCl} + 0.059 \times pH + 0.205 \tag{1}$$

A flow of Ar was maintained over the electrolyte during electrochemical measurements. 80 segments of CV were applied to the working electrodes to stabilize signals. Then the data for linear sweep voltammetry (LSV) curves were collected in the range of -0.6 to 0 V (versus RHE) for HER at a slow scan rate of 2 mV s$^{-1}$ to minimize the capacitive current and corrected for the ohmic potential drop (iR) contribution within the cell. The cycle stability test was carried out by continuously cycling the potential in the potential window of -0.6 to 0 V (versus RHE) at a scan rate of 100 mV s$^{-1}$. After potential cycling, the LSV curve was recorded at a scan rate of 2 mV s$^{-1}$ with iR correction. The time-dependent overpotential stability test was carried out by maintaining a constant current at 9 mA for 24 h. The time-dependent current density durability test was conducted by using controlled-potential electrolysis method without iR compensation. To evaluate the electrochemical active surface areas (ECSA), CV was conducted from 0.265 to 0.315 V (versus RHE) for SANi-I and 0.493 to 0.543 V (versus RHE) for A-Ni-OH in Ar-saturated 1.0 M KOH aqueous solution. Electrochemical impedance spectroscopy (EIS) was performed at -0.019 V (versus RHE) with a frequency from 0.01 to 100k Hz and amplitude of 5 mV. The Tafel slope was calculated according to Tafel equation as follows:

$$\eta = blog( j/j_0 ) \tag{2}$$

where η denotes the overpotential, b denotes the Tafel slope, j denotes the current density, and $j_0$ denotes the exchange current density. The onset potential was determined based on the starting point of the linear region in the Tafel plot. The overpotential was calculated as follows"

$$\eta = E \text{ (vs. RHE)} - E^0 \text{ (vs. RHE)} \qquad (3)$$

where E denotes the actual applied potential and $E^0$ denotes the reversible potential of the reaction. $E^0$ is 0 V versus RHE for the HER.

*In-situ Raman test*: A piece of SANi-I electrode was flattened until thin, cut into a 4 x 5 mm piece and attached to the screen-printed electrode by electrically conductive adhesive. The screen-printed electrode was connected to a 760E potentiostat and then laid flat and clipped to a microscope slide. 100 µl of Ar-saturated 1.0 M KOH was pipetted on the working end of the electrode and a No. 1 thickness cover glass was placed on top. A Nd:YAG laser (532 nm, Mpc 3000, Laser Quantum) and an 1800 g cm$^{-1}$ grating was used in all experiments. For a typical measurement, 40 CV cycles between -1.2 and -1.8 V vs. Ag/AgCl were first performed to obtain a stable current response. The electrolyte was then changed and Raman spectra were collected at open circuit potential (OCP) and during chronoamperometry at various potentials after 5 minutes. The potentials could not be extended to more negative range as the Raman signals were greatly interfered by the evolution of hydrogen gas bubbles. All potentials discussed in the results were given against the reversible hydrogen electrode (RHE). Conversion of the reference potential from the screen-printed electrode (Ag/AgCl) to RHE was calibrated against an external Ag/AgCl electrode and calculated using the following equation:

$$E_{RHE} = E_{Ag/AgCl} + 0.059 \times pH + 0.409 \qquad (4)$$

*Characterizations*: Atomic-resolution high-angle annular dark-field scanning transmission electron microscopy (HAADF-STEM) images and energy dispersive spectra (EDS) were taken using a FEI Titan Cubed Themis G2 300 S/TEM with a probe corrector and a monochromator at 200 kV. Scanning electron microscopy (SEM) images and EDS were collected on the FEI Quanta 450 at high vacuum with an accelerating voltage of 30 kV. Elemental composition was recorded on the FEI Quanta 450 using a silicon drift detector energy-dispersive X-ray spectroscopy (SDDEDS). X-ray diffraction (XRD) patterns were collected on a powder X-ray diffractometer at 40 kV and 15 mA using Co-Kα radiation (Miniflex, Rigaku). X-ray photoelectron spectra (XPS) were obtained using an Axis Ultra (Kratos Analytical, UK) XPS spectrometer equipped with an Al Kα source (1486.6 eV). The I K-edge XAFS measurements were conducted at the Shanghai Synchrotron Radiation Facility (SSRF). The X-ray was monochromatized by a double-crystal Si(311) monochromator. XAFS data was analyzed with the WinXAS3.1 program.[S1] Theoretical amplitudes and phase-shift functions were calculated with the FEFF8.2 code.[S2] The

synchrotron-based nickel L-edge XANES spectra were collected on the soft X-ray spectroscopy at the Australian Synchrotron, which is equipped with a hemispherical electron analyzer and a microchannel plate detector that enables simultaneous recording of the total electron yield and partial electron yield. The raw XANES data were normalized to the photoelectron current of the photon beam, measured on an Au grid. *In-situ* Raman spectroscopy was performed using a confocal Raman microscope (Horiba LabRAM HR Evolution) with a 50X (0.5 N.A) long working distance objective (Olympus). Screen-printed electrodes (Pine Research Instrumentation, RRPE1002C) were employed for in situ tests. These screen-printed electrodes use a 4 x 5 mm carbon working electrode, Ag/AgCl reference electrode, and carbon counter electrode.

# SUPPORTING INFORMATION

## Supplementary Results
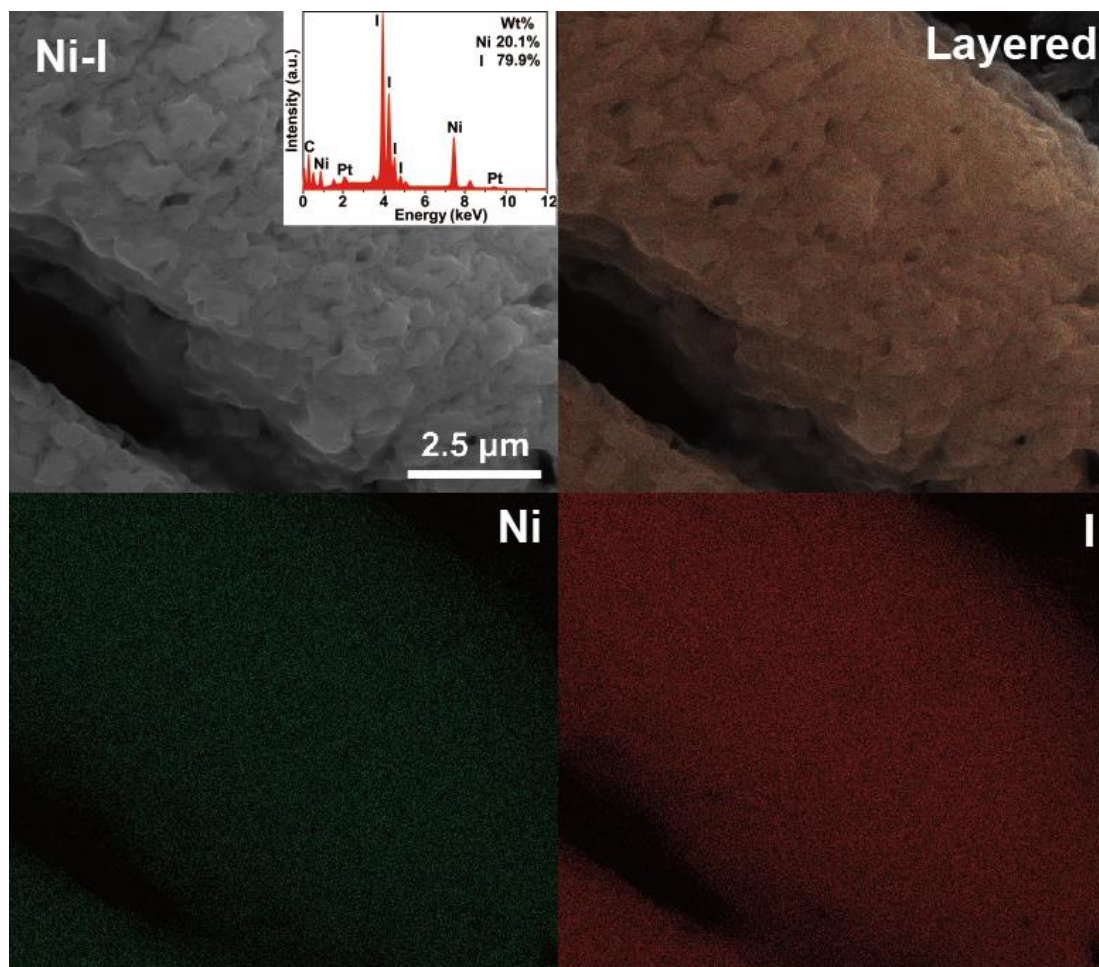


**Figure S1.** SEM image, (inset) corresponding EDS and elemental distribution mapping of Ni-I.
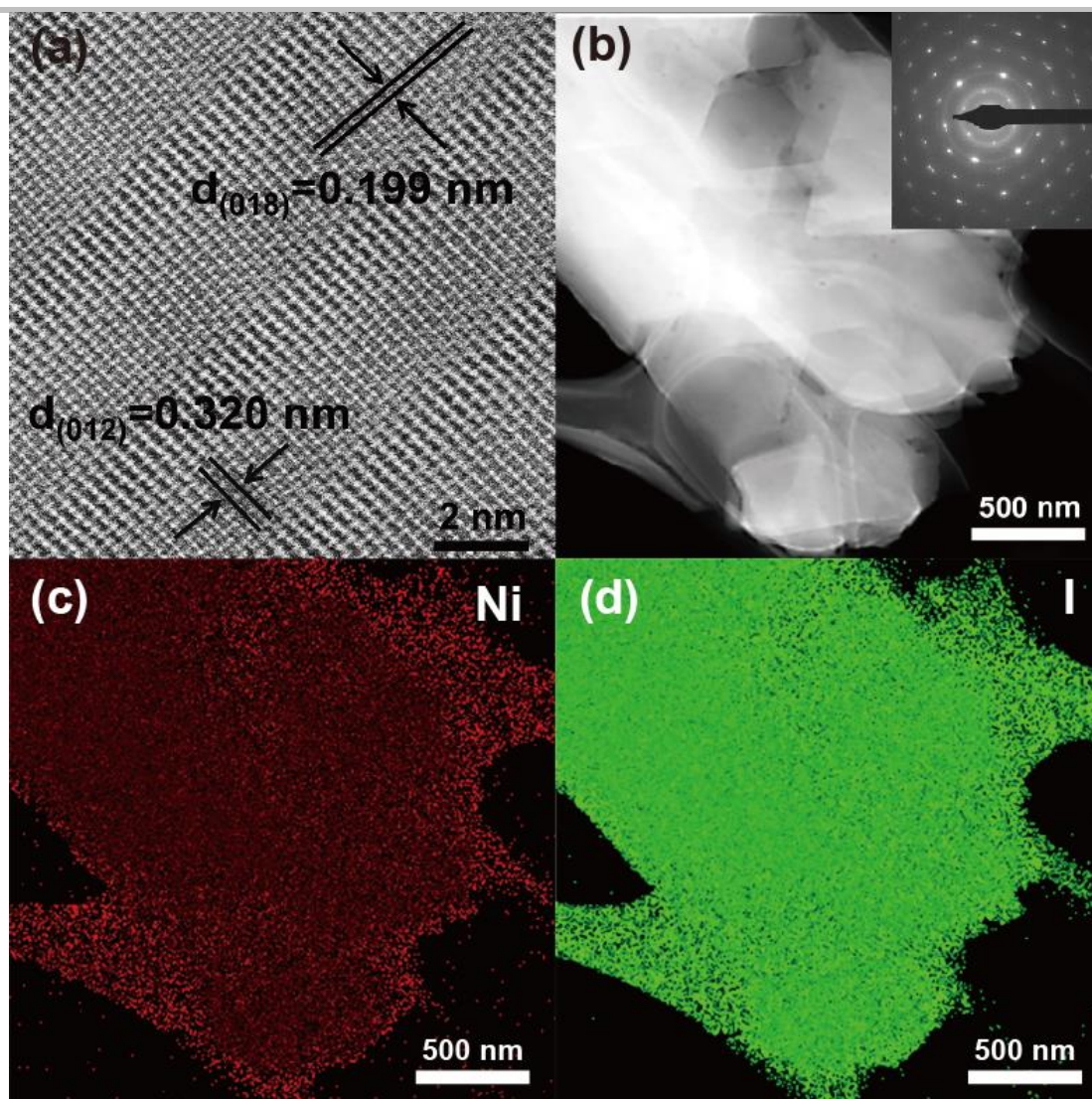
**Figure S2.** a) HRTEM image of Ni-I. b) TEM image of Ni-I and (inset) corresponding SAED pattern. c) Nickel and d) iodine elemental distribution mapping of Ni-I.
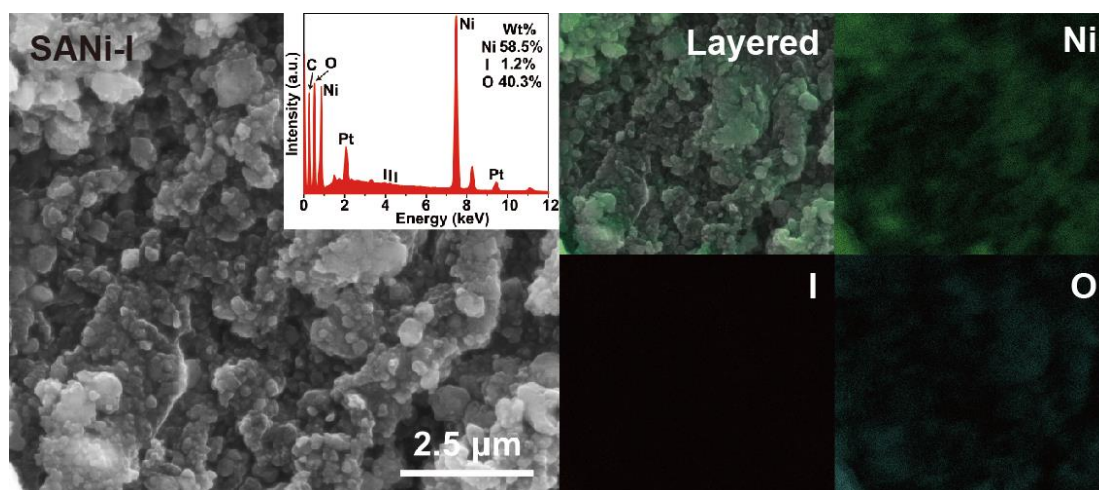


**Figure S3.** SEM image, (inset) corresponding EDS and elemental distribution mapping of SANi-I.
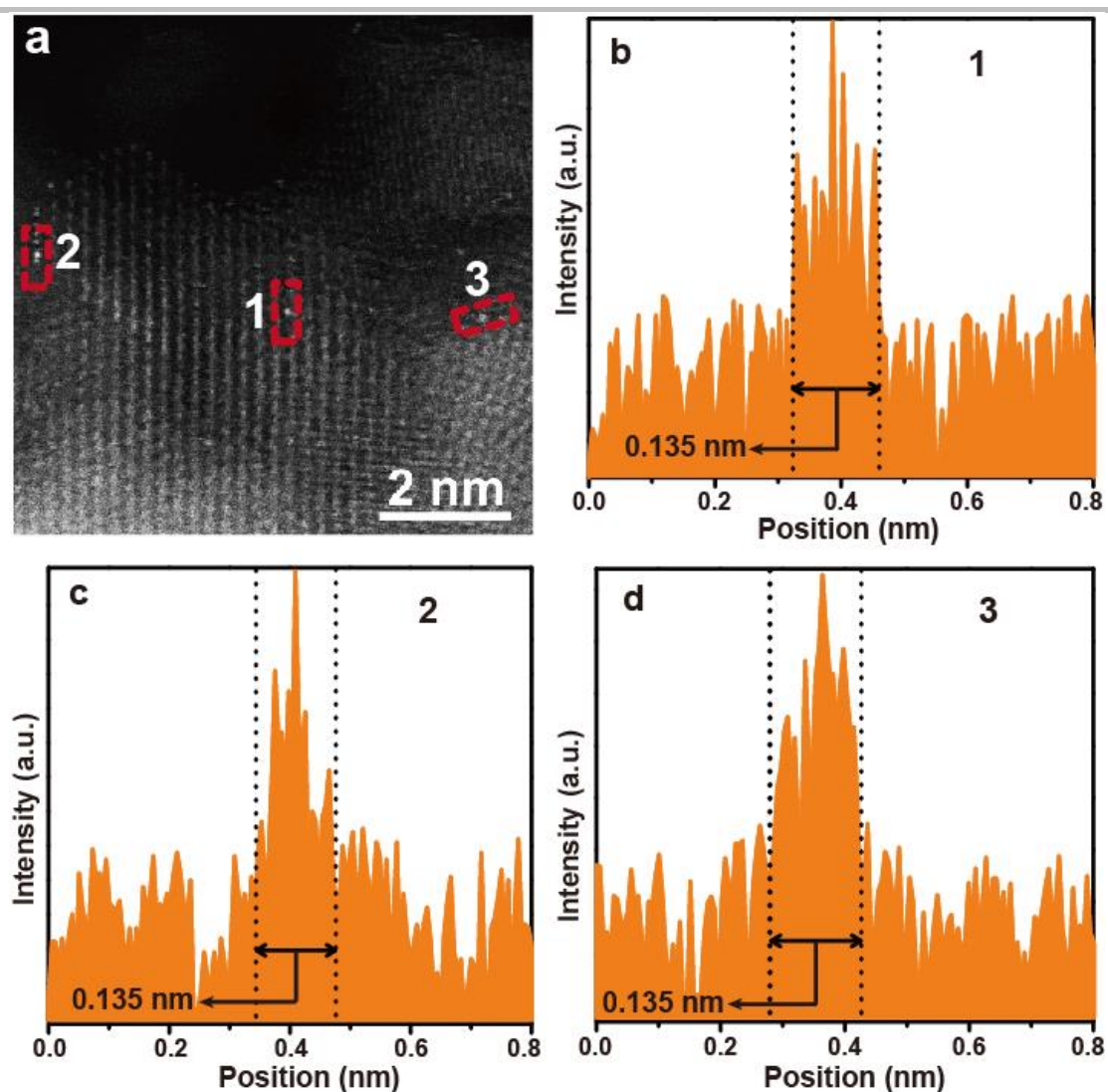
**Figure S4.** a) Highlighted single iodine atoms. b), c) and d) Corresponding intensity profiles.
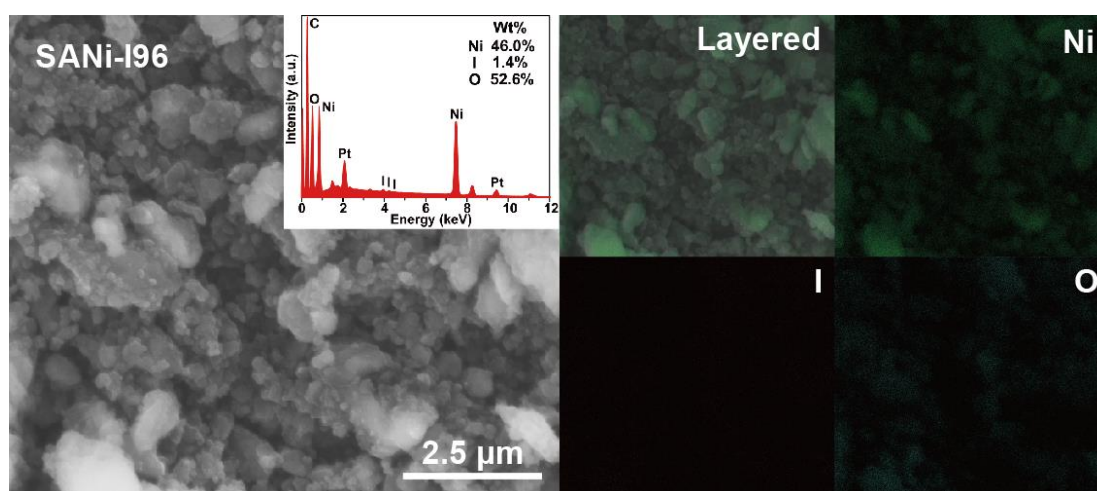


**Figure S5.** SEM image, (inset) corresponding EDS and elemental distribution mapping of SANi-I96.
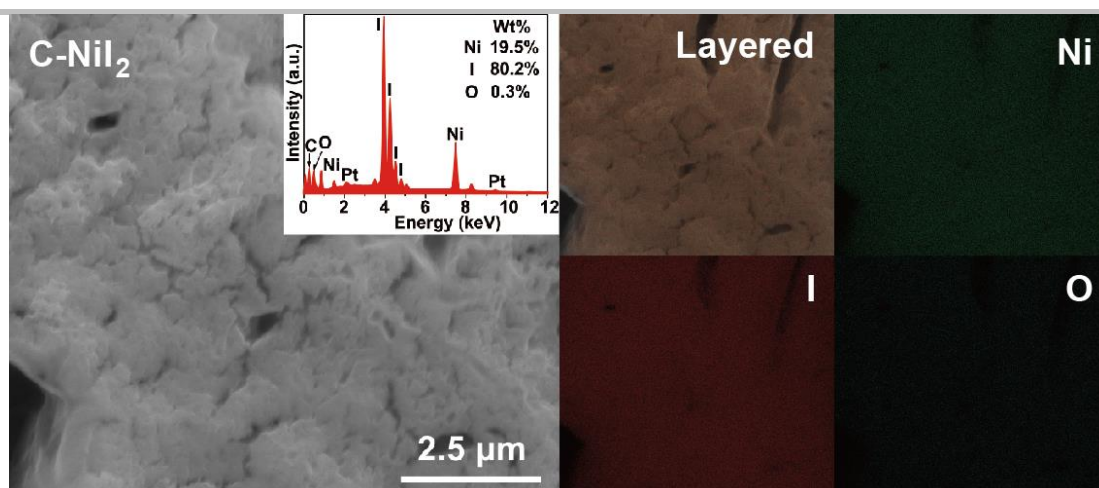
**Figure S6.** SEM image, (inset) corresponding EDS and elemental distribution mapping of C-NiI₂.
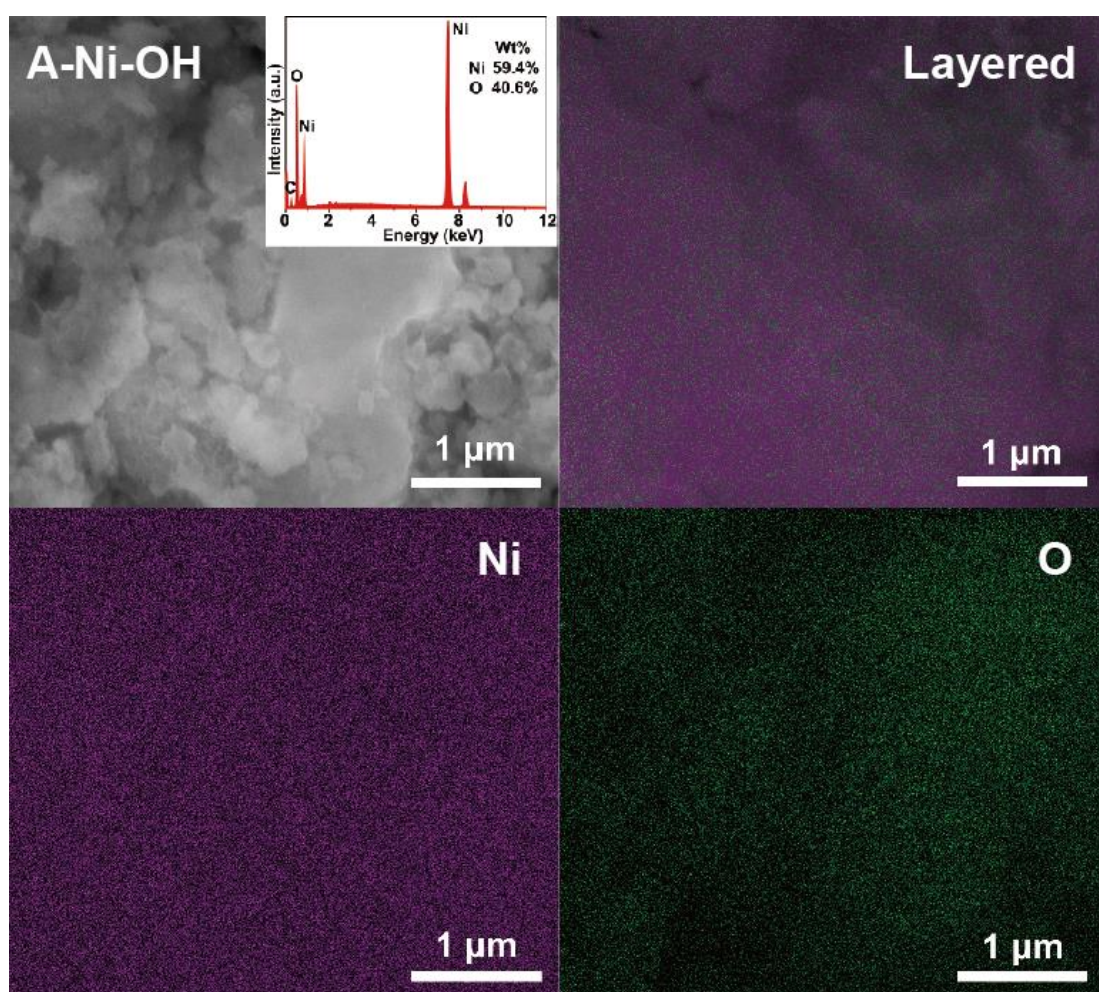


**Figure S7.** SEM image, (inset) corresponding EDS and elemental distribution mapping of A-Ni-OH.
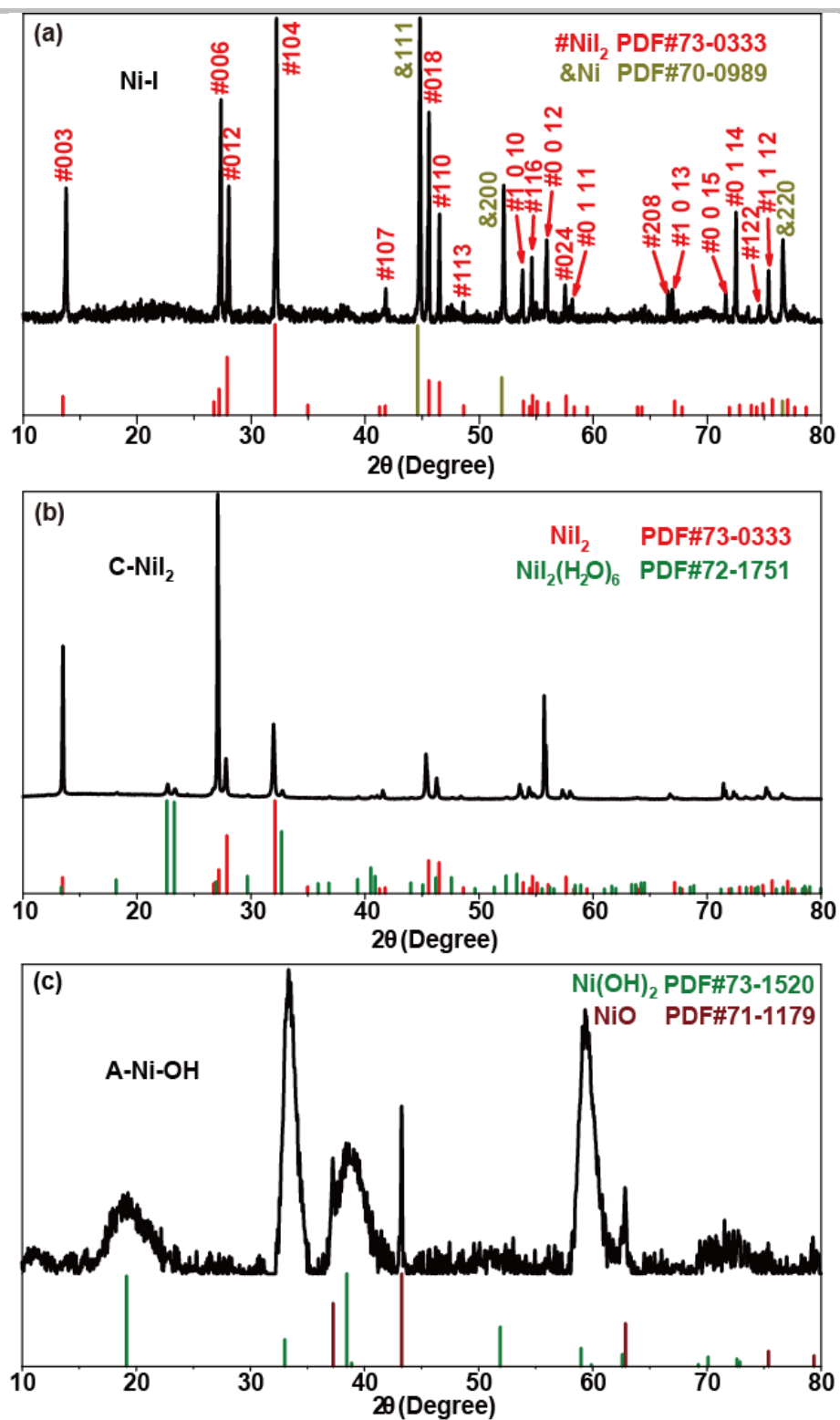
**Figure S8.** XRD patterns of a) Ni-I, b) C-NiI₂ and c) A-Ni-OH.
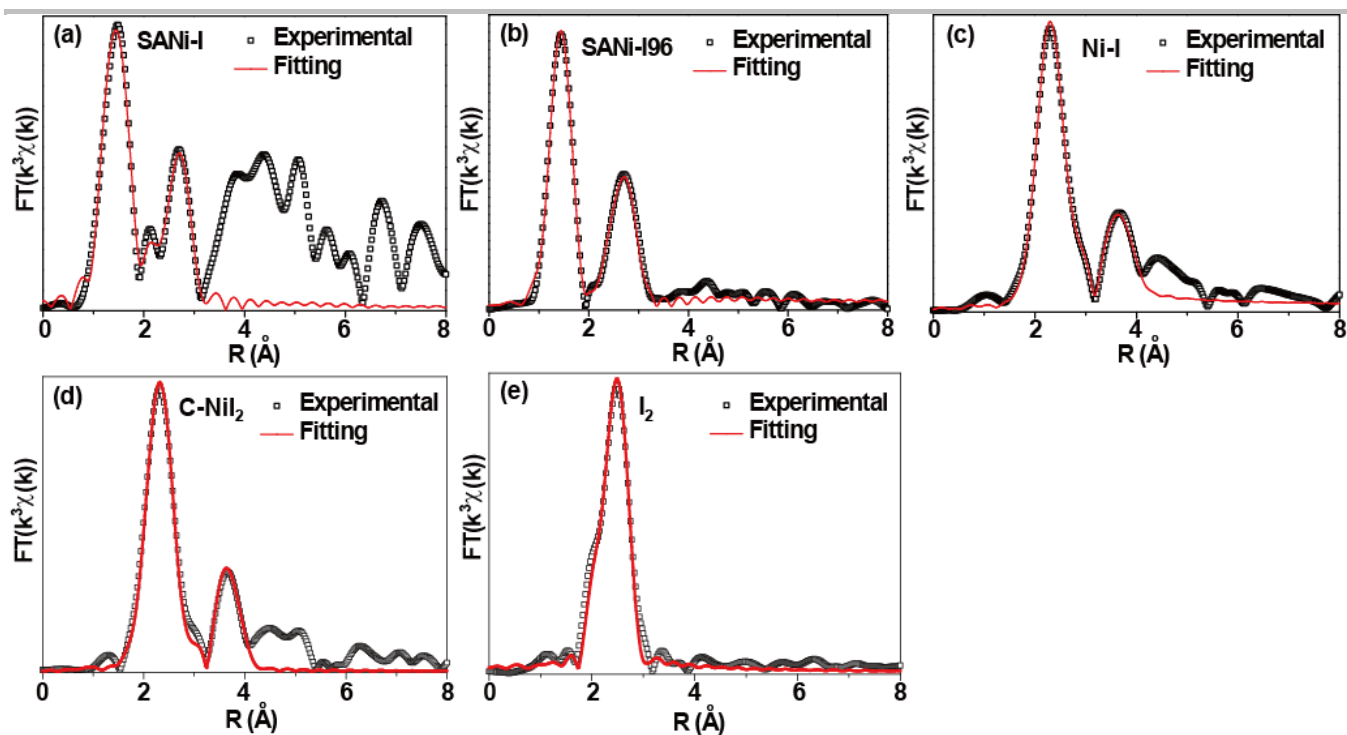
**Figure S9.** EXAFS fitting results of a) SANi-I, b) SANi-I96, c) Ni-I, d) C-NiI$_2$ and e) I$_2$.
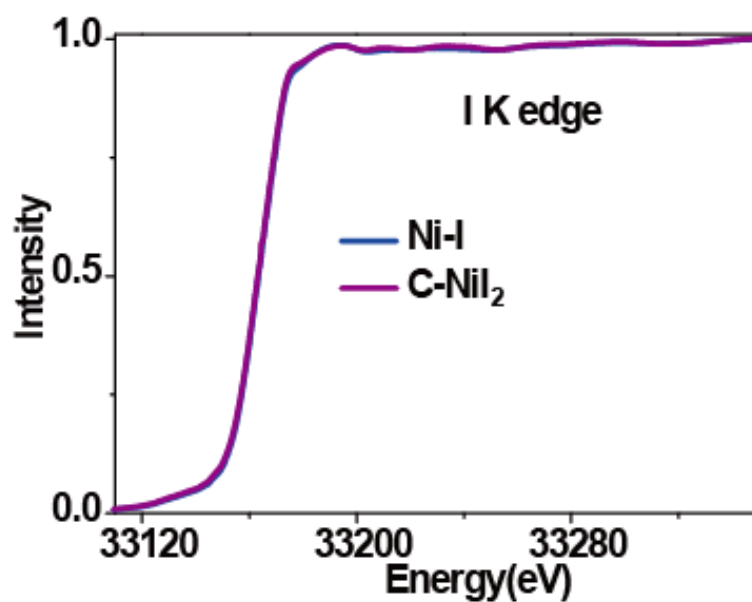


**Figure S10.** Iodine K-edge XANES spectra.
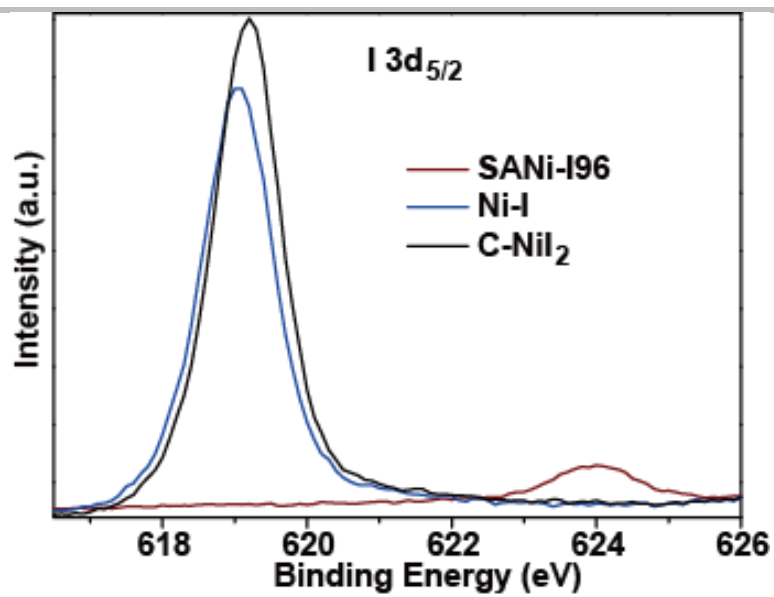
**Figure S11.** Iodine 3d XPS spectra of SANi-I96, Ni-I and C-NiI$_2$.
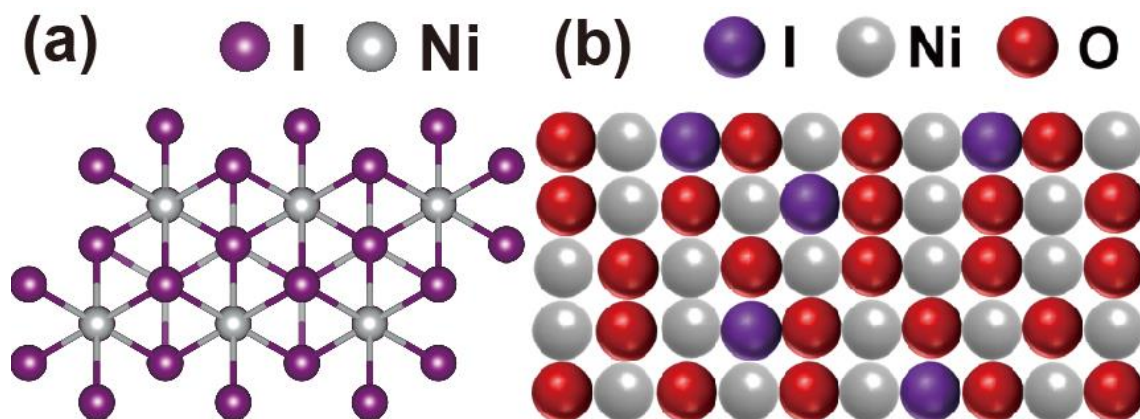


**Figure S12.** Schematic structure of a) nickel iodide with ordered nickel-iodine structure and b) SANi-I.
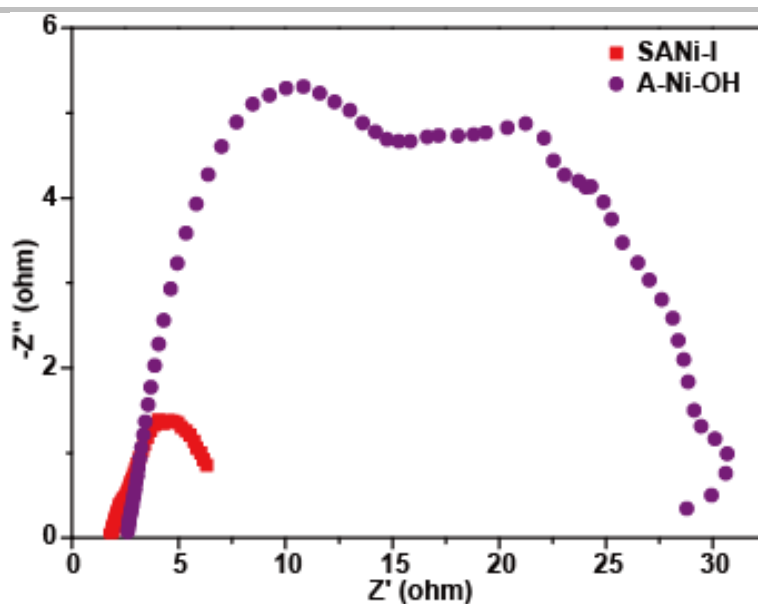
**Figure S13.** Nyquist plots of SANi-I and A-Ni-OH electrodes in 1.0 M KOH with an applied potential of -0.019 V (vs. RHE).
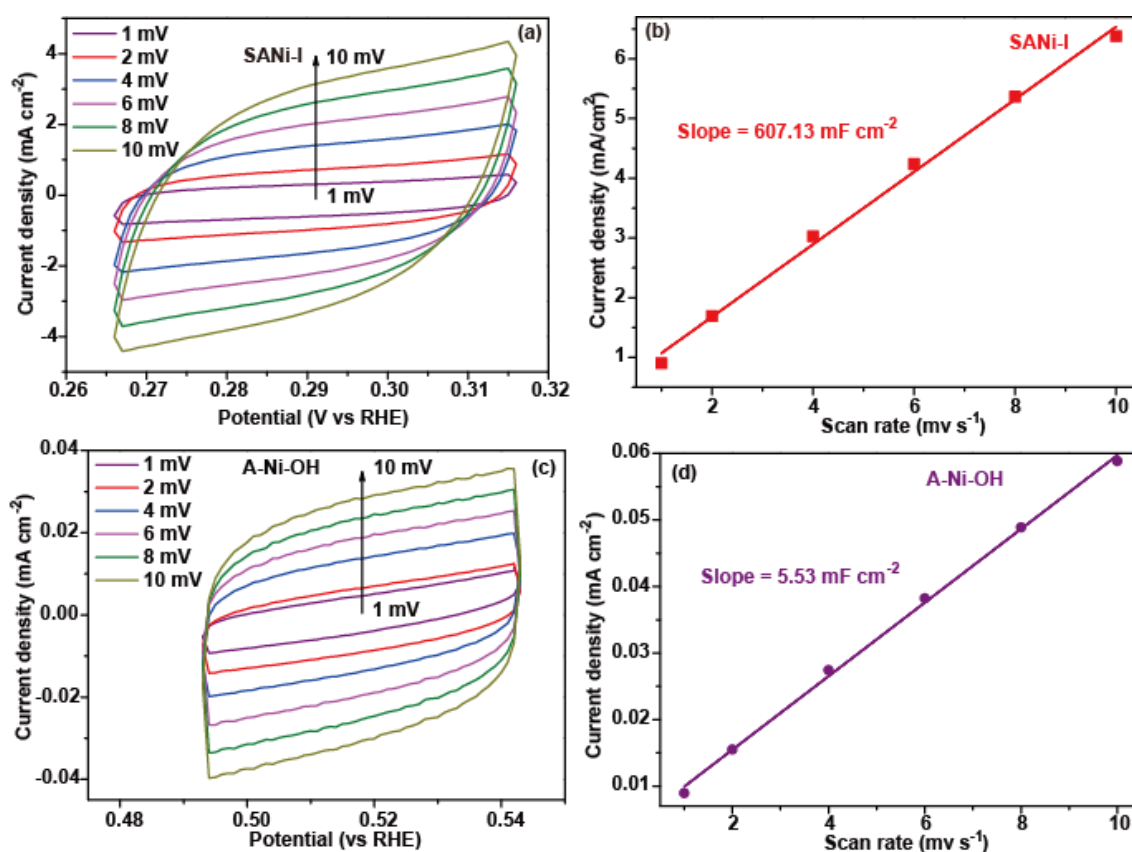


**Figure S14.** The double-layer region by CV measurement with scan rates ranging from 1 to 10 mV s$^{-1}$ in 1.0 M KOH for a) SANi-I and c) A-Ni-OH. Fitting of charging current density with different scan rates for b) SANi-I and d) A-Ni-OH.
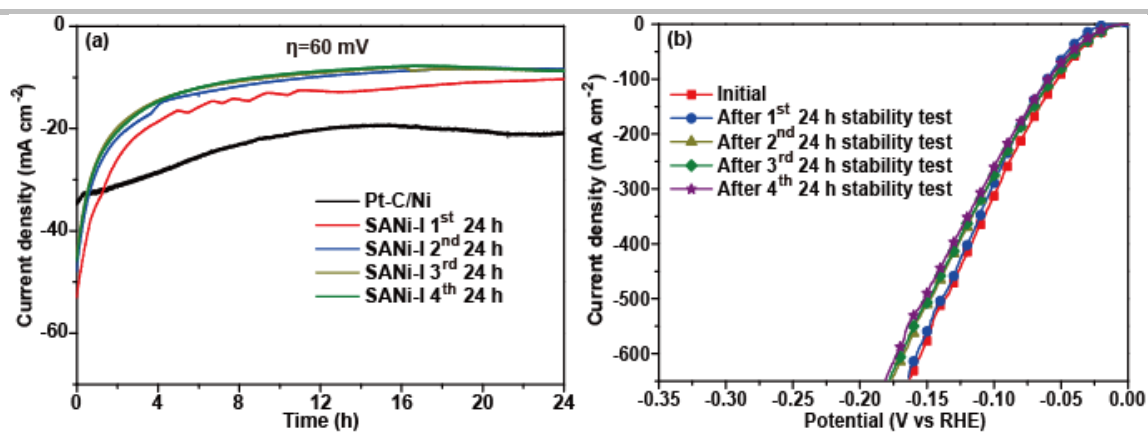
**Figure S15.** a) Chronoamperometric stability test for SANi-I at a constant overpotential of -0.06 V (vs RHE) in the 1st, 2nd, 3rd and 4th day. b) HER performance of SANi-I after each individual stability test.
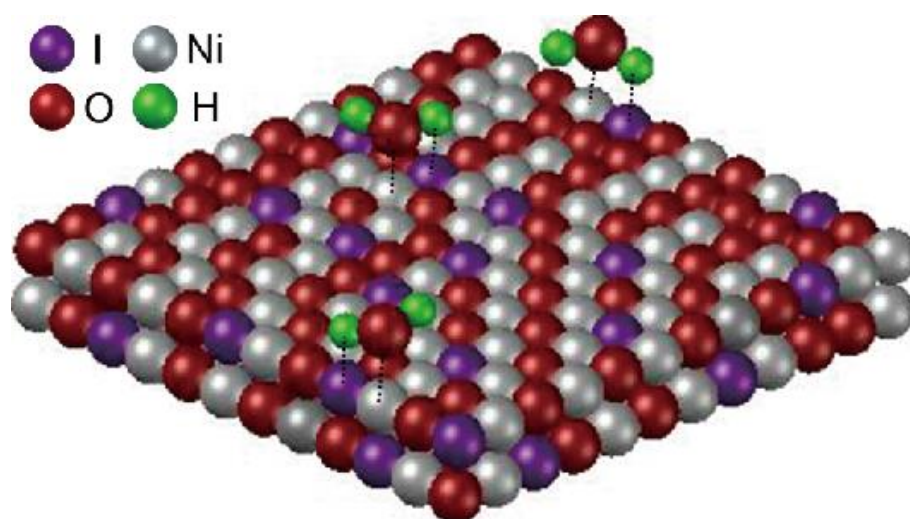


**Figure S16.** Schematic illustration of water adsorption and water activation on SANi-I.

13

**Table S1.** Structural parameters extracted from the I K-edge EXAFS fitting.

| Sample | Scattering pair | Coordination number | Bond length (Å) | $\sigma^2$ ($10^{-3}$ Å$^2$) |
|--------|-----------------|---------------------|-----------------|------------------------------|
| SANi-I | I-O | 2.5 | 1.90 | 7.6 |
| | I-Ni | 3.1 | 3.06 | 6.7 |
| SANi-I96 | I-O | 5.6 | 1.85 | 2.5 |
| | I-Ni | 4.7 | 3.04 | 4.1 |
| Ni-I | I-I | 10.1 | 3.86 | 18.4 |
| | I-Ni | 2.6 | 2.72 | 8.8 |
| C-NiI$_2$ | I-I | 12* | 3.88 | 17.8 |
| | I-Ni | 3* | 2.72 | 8.0 |
| I | I-I | 1* | 2.72 | 2.5 |

$\sigma^2$ is Debye-Waller factor (a measure of thermal and static disorder in absorber-scatterer distances). Error bounds (accuracies) were estimated as Coordination number, ±10%; Bond length, ±1%; $\sigma^2$, ±10%. * is fixed coordination number according to the standard crystal structure.

**Table S2.** HER performance comparison between SANi-I and recently reported electrocatalysts in alkaline media.

| Electrocatalysts | Electrolyte | j, mA cm$^{-2}$ | η required, mV | Tafel slop, mV dec$^{-1}$ | Reference |
|---|---|---|---|---|---|
| SANi-I | 1.0 M KOH | 100 | 60 | 34.6 | This work |
| Ni$_2$P@NPCNFs | 1.0 M KOH | 100 | 205 | 79.7 | S3 |
| Ni$_3$N/Ni/NF | 1.0 M KOH | 100 | 64 | 29.3 | S4 |
| SCFP-NF | 1.0 M KOH | 100 | 260 | 108 | S5 |
| Ni$_x$Co$_{3-x}$S$_4$/Ni$_3$S$_2$/NF | 1.0 M KOH | 100 | 258 | 95 | S6 |
| NS-MnO$_2$ | 1.0 M KOH | 100 | 350 | 62 | S7 |
| Cu@NiFe LDH | 1.0 M KOH | 100 | 192 | 58.9 | S8 |
| MoS$_2$-Ni$_3$S$_2$ HNRs/NF | 1.0 M KOH | 100 | 191 | 61 | S9 |
| Co$_1$Mn$_1$CH/NF | 1.0 M KOH | 100 | 328 | N/A | S10 |
| Ni$_{12}$P$_5$/NF | 1.0 M KOH | 100 | 290 | N/A | S11 |
| Ni$_2$P$_5$/NF | 1.0 M KOH | 100 | 215 | N/A | S11 |
| Ni$_{0.89}$Co$_{0.11}$Se$_2$ MNSN/NF | 1.0 M KOH | 100 | 160 | 52 | S12 |
| N-Ni$_3$S$_2$/NF | 1.0 M KOH | 100 | 230 | N/A | S13 |
| Ni-C-N nanosheets | 1.0 M KOH | 100 | 110 | 40 | S14 |
| MoO$_x$/Ni$_3$S$_2$/NF | 1.0 M KOH | 100 | 224 | 90 | S15 |
| Hierarchical NiCo$_2$O$_4$ Hollow Microcuboids | 1.0 M KOH | 100 | 245 | 49.7 | S16 |

### References

[S1] T. Ressler, *J. Synchrotron Radiat.* **1998**, *5*, 118.

[S2] A. L. Ankudinov, B. Ravel, J. J. Rehr, S. D. Conradson, *Phys. Rev. B* **1998**, *58*, 7565.

[S3] M.-Q. Wang, C. Ye, H. Liu, M. Xu, S.-J. Bao, *Angew. Chem., Int. Ed.* **2018**, 57, 1963-1967.

[S4] F. Song, W. Li, J. Yang, G. Han, P. Liao, Y. Sun, *Nat. Commun.* **2018**, 9, 4531.

[S5] G. Chen, Z. Hu, Y. Zhu, B. Gu, Y. Zhong, H.-J. Lin, C.-T. Chen, W. Zhou, Z. Shao, *Adv. Mater.* **2018**, 30, 1804333.

[S6] Y. Wu, Y. Liu, G.-D. Li, X. Zou, X. Lian, D. Wang, L. Sun, T. Asefa, X. Zou, *Nano Energy* **2017**, 35, 161-170.

[S7] Y. Zhao, C. Chang, F. Teng, Y. Zhao, G. Chen, R. Shi, G. I. N. Waterhouse, W. Huang, T. Zhang, *Adv. Energy Mater.* **2017**, 7, 1700005.

[S8] L. Yu, H. Zhou, J. Sun, F. Qin, F. Yu, J. Bao, Y. Yu, S. Chen, Z. Ren, *Energy. Environ. Sci.* **2017**, 10, 1820-1827.

[S9] Y. Yang, K. Zhang, H. Lin, X. Li, H. C. Chan, L. Yang, Q. Gao, *ACS Catal.* **2017**, 7, 2357-2366.

[S10] T. Tang, W.-J. Jiang, S. Niu, N. Liu, H. Luo, Y.-Y. Chen, S.-F. Jin, F. Gao, L.-J. Wan, J.-S. Hu, *J. Am. Chem. Soc.* **2017**, 139, 8320-8328.

[S11] P. W. Menezes, A. Indra, C. Das, C. Walter, C. Göbel, V. Gutkin, D. Schmeiβer, M. Driess, *ACS Catal.* **2017**, 7, 103-109.

[S12] B. Liu, Y.-F. Zhao, H.-Q. Peng, Z.-Y. Zhang, C.-K. Sit, M.-F. Yuen, T.-R. Zhang, C.-S. Lee, W.-J. Zhang, *Adv. Mater.* **2017**, 29, 1606521.

[S13] P. Chen, T. Zhou, M. Zhang, Y. Tong, C. Zhong, N. Zhang, L. Zhang, C. Wu, Y. Xie, *Adv. Mater.* **2017**, 29, 1701584.

[S14] J. Yin, Q. Fan, Y. Li, F. Cheng, P. Zhou, P. Xi, S. Sun, *J. Am. Chem. Soc.* **2016**, 138, 14546-14549.

[S15] Y. Wu, G.-D. Li, Y. Liu, L. Yang, X. Lian, T. Asefa, X. Zou, *Adv. Funct. Mater.* **2016**, 26, 4839-4847.

[S16] X. Gao, H. Zhang, Q. Li, X. Yu, Z. Hong, X. Zhang, C. Liang, Z. Lin, *Angew. Chem., Int. Ed.* **2016**, 55, 6290-6294.

# Chapter 6 Contemporaneous Oxidation State Manipulation to Accelerate Intermediates Desorption for Overall Water Electrolysis

## 6.1 Introduction and Significance

The development of bifunctional cobalt nitride and sulfide (CoNS) electrocatalysts for overall water electrolysis with high activity and stability is preferable for commercialized hydrogen production and yet remains challenging. The oxidation state of cobalt, nitrogen and sulfur in the CoNS electrocatalysts plays a significant role in accelerating desorption of intermediates for the oxygen evolution reaction (OER) and hydrogen evolution reaction (HER), which further improves the sluggish kinetics for electrochemical water electrolysis. However, conventional preparations did not provide a simple pathway to contemporaneously manipulate the oxidation state of Co, N and S. Consequently, it is imperative to develop a simple method to simultaneously tailor Co, N and S oxidation state and to accelerate the kinetics for overall water electrolysis. Here, contemporaneous manipulation of Co, N and S oxidation state and accelerated desorption of intermediates were realized by one-step calcination in vacuum-sealed ampoule, electrocatalytic mechanism was proposed, and the as-prepared CoNS electrodes exhibited excellent electrocatalytic performance for overall water electrolysis under neutral condition. The highlights of this work include:

- The contemporaneous manipulation of Co, N and S oxidation state was realized via simple synthesis of CoNS, in which cobalt foil was activated by hydrochloric acid to prepare activated cobalt (ACo) and afterwards ACo was sealed with thiourea in an evacuated ampoule to synthesize CoNS.

- The oxidation state analyses via X-ray photoelectron spectroscopy reveal that low Co oxidation state favors the OER while high N and S oxidation state promotes the HER, indicating that the water splitting process for this electrocatalyst is kinetically governed by the desorption of intermediates.

- A 100 mA cm$^{-2}$ OER current density is achieved for CoNS at an overpotential of

275 mV, which is lower than that for benchmark Ir/C (374 mV) in 1.0 M KOH. A 4.5 mA cm$^{-2}$ current density at a voltage of 1.8 V is achieved for CoNS based overall electrolysis in neutral buffer solution (pH = 7.4), which is higher than that for novel-metal based system at the same voltage (3.4 mA cm$^{-2}$).

## 6.2 Contemporaneous Oxidation State Manipulation to Accelerate Intermediates Desorption for Overall Water Electrolysis

# Statement of Authorship

| Title of Paper | Contemporaneous Oxidation State Manipulation to Accelerate Intermediates Desorption for Overall Water Electrolysis |
|---|---|
| Publication Status | ☑ Published ☐ Accepted for Publication <br> ☐ Submitted for Publication ☐ Unpublished and Unsubmitted work written in manuscript style |
| Publication Details | Yongqiang Zhao, Bo Jin, Anthony Vasileff, Yan Jiao and Shi-Zhang Qiao, Chemical Communications 2019, 55, 8313-8316. |

## Principal Author

| Name of Principal Author (Candidate) | Yongqiang Zhao |
|---|---|
| Contribution to the Paper | Research plan, material synthesis, most of the characterizations and data analysis, electrochemical measurements and manuscript drafting. |
| Overall percentage (%) | 70 |
| Certification: | This paper reports on original research I conducted during the period of my Higher Degree by Research candidature and is not subject to any obligations or contractual agreements with a third party that would constrain its inclusion in this thesis. I am the primary author of this paper. |
| Signature | Date 21/05/2019 |

## Co-Author Contributions

By signing the Statement of Authorship, each author certifies that:

   i.     the candidate's stated contribution to the publication is accurate (as detailed above);

   ii.    permission is granted for the candidate in include the publication in the thesis; and

   iii.   the sum of all co-author contributions is equal to 100% less the candidate's stated contribution.

| Name of Co-Author | Bo Jin |
|---|---|
| Contribution to the Paper | 8%. Discussion of research plan, data analysis and manuscript revision. |
| Signature | Date 21.05.2019 |

| Name of Co-Author | Anthony Vasileff |
|---|---|
| Contribution to the Paper | 6%. Assistance with manuscript edit and polish. |
| Signature | Date 21. 05. 2019. |

| Name of Co-Author | Yan Jiao |
|---|---|
| Contribution to the Paper | 6%. Discussion of research plan and data analysis. |
| Signature | | Date | 21 May 2019 |

| Name of Co-Author | Shi-Zhang Qiao |
|---|---|
| Contribution to the Paper | 10%. Supervision of the work, data interpretation and manuscript evaluation. |
| Signature | | Date | 21.05.2019 |

# ChemComm

## COMMUNICATION

Check for updates

# Contemporaneous oxidation state manipulation to accelerate intermediate desorption for overall water electrolysis†

Yongqiang Zhao, Bo Jin, Anthony Vasileff, [ID] Yan Jiao and Shi-Zhang Qiao [ID] *

**Contemporaneous oxidation state engineering of Co, N and S for cobalt nitride and sulfide electrocatalysts is demonstrated to facilitate intermediate desorption for both the oxygen evolution reaction and the hydrogen evolution reaction, leading to efficient overall water electrolysis in a neutral buffer electrolyte.**

Oxygen and hydrogen production *via* water electrolysis has long been regarded as one of the most attractive sustainable technologies, in which oxygen is produced through the oxygen evolution reaction (OER) at the anode and hydrogen is produced *via* the hydrogen evolution reaction (HER) at the cathode.[1–5] However, both the OER and HER are kinetically sluggish.[6] Efficient electrocatalysts, predominantly extortionate noble-metal based materials such as Ru/Ir-based materials for the OER[7] and Pt-based electrocatalysts for the HER,[8] are required to accelerate these two reactions. This limits the large-scale application of water electrolysis.

Recently, non-precious metal and non-metal electrocatalysts have been considered to be promising candidates for water electrolysis.[9–13] These materials include transition metal borides/carbides/nitrides/phosphides/oxides/chalcogenides[14–22] and carbon-based electrocatalysts.[23] Particularly, highly efficient bifunctional electrocatalysts that simultaneously facilitate the OER and the HER in the same electrolyte need to be developed for improving the overall water electrolysis efficiency. It has been discovered that the electrocatalytic performance can be modulated by manipulating the oxidation state of metal and non-metal components in bifunctional electrocatalysts.[24,25] However, common synthesis methods fail to simultaneously manipulate the oxidation state of metal and non-metal components in bifunctional electrocatalysts. Therefore, contemporaneous manipulation of the oxidation state of metal and non-metal components in bifunctional electrocatalysts is of great significance for accelerating the performance of overall water electrolysis.

*School of Chemical Engineering, The University of Adelaide, Adelaide, SA 5005, Australia. E-mail: s.qiao@adelaide.edu.au*

Herein, we demonstrate a simple strategy to simultaneously tailor the oxidation state of metal (cobalt) and non-metal components (nitrogen and sulfur) in cobalt nitride and sulfide electrocatalysts. Cobalt foil was first activated using hydrochloric acid, leading to activated cobalt oxide hydroxide (ACo). The ACo was then sealed with thiourea in an evacuated ampoule to prepare cobalt nitride and sulfide (CoNS). The oxidation states of Co, N and S in the CoNS electrocatalysts were contemporaneously manipulated by controlling the mass ratio of Co foil to thiourea. It was discovered that the low Co oxidation state favors the OER performance while the high N and S oxidation states promote the HER activity, indicating that the water splitting process for this electrocatalyst is kinetically governed by the desorption of intermediates.[26,27] Inspired by the significant electrocatalytic capability, the as-synthesized CoNS electrodes were used as both anodes and cathodes for overall water electrolysis. The results show that CoNS electrodes exhibit greater electrocatalytic activity at low overpotentials in a neutral electrolyte than the novel metal system. It is concluded that the simple manipulation of the oxidation state and the novel design of CoNS can provide a promising pathway for promoting the neutral water electrolysis performance and reducing the cost of hydrogen production.

The contemporaneous manipulation of Co, N and S oxidation states was realized *via* simple synthesis of CoNS, in which cobalt foil was activated using hydrochloric acid to prepare ACo and afterwards ACo was sealed with thiourea in an evacuated ampoule to synthesize CoNS (see Experimental details, ESI†). During the activation, the inert cobalt oxide layer and cobalt on the surface were dissolved and the highly active cobalt atoms beneath were exposed. These active cobalt atoms were subsequently oxidized by the dissolved oxygen in water, forming ACo. Volatile nitrogen- and sulfur-containing species were formed when thiourea was thermally decomposed and reacted with ACo to form CoNS. The high gaseous pressure of nitrogen and sulfur-containing species in the ampoule can benefit the nitridation and sulfurization of CoNS. The X-ray diffraction (XRD) pattern (Fig. S1, ESI†) indicates that ACo consists of cobalt oxide
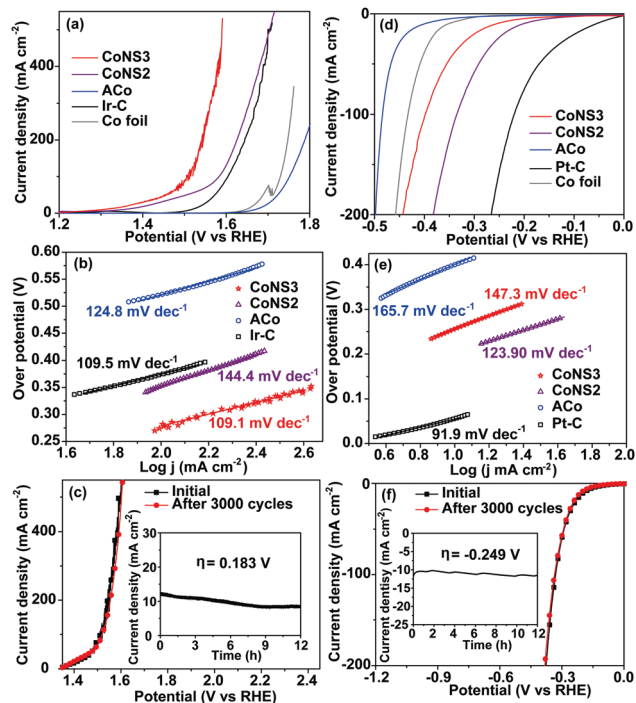
Fig. 3 (a) OER performance of CoNS3, CoNS2, ACo, and Ir–C in 1.0 M KOH. (b) Corresponding Tafel plots with associated linear fittings. (c) The cycle stability of CoNS3 and (inset) the time-dependent current density of CoNS3 at a constant overpotential of 0.183 V (vs. RHE) in 1.0 M KOH. (d) HER performance of CoNS3, CoNS2, ACo, and Pt–C in 1.0 M KOH. (e) Corresponding Tafel plots with associated linear fittings. (f) The cycle stability of CoNS2 and (inset) the time-dependent current density of CoNS2 at a constant overpotential of −0.249 V (vs. RHE) in 1.0 M KOH.

was obtained at an overpotential of 335 mV for CoNS2, which was lower than those for CoNS3 (399 mV), ACo (484 mV) and cobalt foil (434 mV). A comparative summary of the HER electrocatalytic performance of state-of-the-art catalysts reported in recent studies is presented in Table S2 in the ESI.† The electrocatalytic activity of CoNS2 is comparable to those of the most active non-noble metal based electrocatalysts, such as $Ni_{0.75}Co_{0.25}P$ supported on N-doped carbon (360 mV),[31] $Ni_3(S_{0.25}Se_{0.75})_2$@NiOOH (400 mV)[32] and $Ni_1Co_1P$ nanowires (397 mV).[33] The Tafel slope for CoNS2 was 141.1 mV dec$^{-1}$ (Fig. 3e), which is lower than those for CoNS3 (147.3 mV dec$^{-1}$) and ACo (165.7 mV dec$^{-1}$), indicating more favorable HER kinetics. CoNS2 exhibited stable electrocatalytic performance for 3000 HER cycles (Fig. 3f) and negligible degradation of the current density during 12 h of operation (inset of Fig. 3f). The XRD pattern of CoNS2 after the cycle stability test (Fig. S7b, ESI†) indicates that CoNS2 is structurally stable, demonstrating its potential value as an electrocatalyst.

The OER and HER kinetics were further analyzed through electrochemical impedance spectroscopy. For the OER, the Nyquist plots of CoNS3 display a semicircle in the low-frequency range (an indicator of the charge transfer resistance of the catalysts). The calculated resistance of CoNS3 (12.32 Ω) (Fig. S8a, ESI†) is smaller than that of ACo (195.8 Ω) (Fig. S8b, ESI†), indicating favorable charge transfer for CoNS3 in the OER. For

the HER, The calculated resistance of CoNS2 (11.62 Ω) (Fig. S8c, ESI†) is smaller than that of ACo (34.5 Ω) (Fig. S8d, ESI†), indicating favorable charge transfer for CoNS2 in the HER.

The electrochemical active surface areas of CoNS3, CoNS2 and ACo were measured by calculating the electrochemical double-layer capacitance ($C_{dl}$) to obtain profound insight into electrocatalytic sites. CoNS3 exhibits a $C_{dl}$ of 24.87 mF cm$^{-2}$ (Fig. S9a and b, ESI†), which is much higher than that of ACo (0.79 mF cm$^{-2}$) in the same potential range (Fig. S9c and d, ESI†). Similarly, CoNS2 exhibits a $C_{dl}$ of 32.63 mF cm$^{-2}$ (Fig. S9e and f, ESI†), which is much higher than that of ACo (4.41 mF cm$^{-2}$) in the same potential range (Fig. S9g and h, ESI†). This indicates that CoNS3 and CoNS2 possess abundant electrocatalytic sites.

Based on the aforementioned results and discussion, we present our understanding of the mechanism for the OER and HER. The OER mechanism can be clarified by the widely accepted five-step mechanism for transition metal electrocatalysts [(1) $* + OH^- \rightarrow *OH + e^-$; (2) $*OH + OH^- \rightarrow H_2O + *O + e^-$; (3) $*O + OH^- \rightarrow *OOH + e^-$; (4) $*OOH + OH^- \rightarrow *O_2 + e^-$; and (5) $*O_2 \rightarrow * + O_2$] and the HER process is carried out through a Volmer $(H_2O + e^- \rightarrow H* + OH^-)$ − Tafel $(2H* \rightarrow H_2)$ or Heyrovsky $(H_2O + e^- + H* \rightarrow H_2 + OH^-)$ pathway in alkaline media.[34] Efficient dissociative adsorption of water molecules occurs at electrocatalytically active $Co^{\delta+}$ and $E^{\delta-}$ (E = N or S) sites, followed by $OH^-$ adsorption on $Co^{\delta+}$ (OER mechanism step 1) and hydrogen adsorption on $E^{\delta-}$ (HER mechanism step 1). The adsorbed intermediates will then react and form oxygen and hydrogen. According to the Sabatier principle, the ideal OER and HER processes require a moderate bond strength between the electrocatalytically active sites and the adsorbed intermediates.[35] If the bond is too weak, the activation of the intermediates on the active sites will be decelerated. Nevertheless, if the intermediates strongly bind with the active sites, the available active sites will be fully occupied, leading to electrocatalyst poisoning. In addition, it has been reported that the discharge of the HER and OER intermediates can greatly promote the overall water electrolysis process.[26,27] In our study, CoNS3 with a relatively low cobalt oxidation state exhibits a superior OER electrocatalytic activity and CoNS2 with a comparatively high nitrogen and sulfur oxidation state exhibits improved HER performance. Consequently, it is reasonable to propose that a relatively low oxidation state for $Co^{\delta+}$ leads to a moderate bond strength and can facilitate OER intermediate desorption; at the same time, electrochemically active sites $E^{\delta-}$ with a comparatively high oxidation state can moderately bond with the HER intermediates and accelerate their desorption. As a result, the overall water electrolysis process is promoted.

Two-electrode electrolyzers in 1.0 M KOH and neutral buffer solution were established with the integration of CoNS3 and CoNS2 as the anode and the cathode for overall water electrolysis (denoted as CoNS3//CoNS2). Ir–C//Pt–C was also prepared for comparison. Although the electrocatalytic performance of Ir–C//Pt–C in 1.0 M KOH electrolyte exceeds that of CoNS3//CoNS2, the CoNS3//CoNS2 system exhibits better electrocatalytic activity in neutral buffer solution (Fig. 4a). The current density obtained at a potential of 1.8 V for CoNS3//CoNS2 is 4.5 mA cm$^{-2}$,
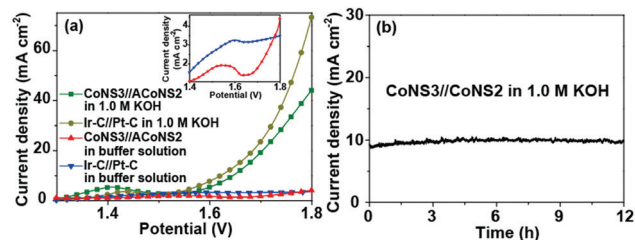
Fig. 4 (a) Polarization curves of CoNS3//CoNS2 and Ir–C//Pt–C overall water splitting systems in 1.0 M KOH and neutral buffer solution (pH = 7.4) and (inset) enlarged polarization curves in buffer solution. (b) The time-dependent current density of CoNS3//CoNS2 at 1.64 V for an overall water splitting system.

higher than that for Ir–C//Pt–C (3.4 mA cm$^{-2}$). CoNS3//CoNS2 exhibits stable current density during 12 h of continuous operation (Fig. 4b).

In summary, we manipulated the electrocatalytic performance of CoNS by contemporaneously tailoring the oxidation states of Co, N and S in the electrocatalysts. A current density of 100 mA cm$^{-2}$ was obtained at an overpotential of 275 mV for CoNS3 in the OER operation and 335 mV for CoNS2 in the HER operation, respectively. The overall water splitting electrolyzer using CoNS3//CoNS2 exhibited a decent cell voltage of 1.8 V to an output of 4.5 mA cm$^{-2}$ in neutral buffer solution. Our results provide a promising strategy for manipulating the oxidation state and the electrocatalytic performance of electrocatalysts in energy conversion devices.

## Conflicts of interest

There are no conflicts to declare.

## Notes and references

1 I. Roger, M. A. Shipman and M. D. Symes, *Nat. Rev. Chem.*, 2017, **1**, 0003.
2 J. Bao, X. Zhang, B. Fan, J. Zhang, M. Zhou, W. Yang, X. Hu, H. Wang, B. Pan and Y. Xie, *Angew. Chem., Int. Ed.*, 2015, **54**, 7399–7404.
3 M.-R. Gao, J.-X. Liang, Y.-R. Zheng, Y.-F. Xu, J. Jiang, Q. Gao, J. Li and S.-H. Yu, *Nat. Commun.*, 2015, **6**, 5982.
4 N. Jiang, B. You, M. Sheng and Y. Sun, *Angew. Chem., Int. Ed.*, 2015, **54**, 6251–6254.
5 H. Jin, J. Wang, D. Su, Z. Wei, Z. Pang and Y. Wang, *J. Am. Chem. Soc.*, 2015, **137**, 2688–2694.
6 J. Wang, Z. Wei, S. Mao, H. Li and Y. Wang, *Energy Environ. Sci.*, 2018, **11**, 800–806.
7 T. Reier, H. N. Nong, D. Teschner, R. Schlögl and P. Strasser, *Adv. Energy Mater.*, 2017, 7, 1601275.
8 L. Zhang, L. Han, H. Liu, X. Liu and J. Luo, *Angew. Chem., Int. Ed.*, 2017, **56**, 13694–13698.
9 X. Li, X. Hao, A. Abudula and G. Guan, *J. Mater. Chem. A*, 2016, **4**, 11973–12000.
10 B. Xiong, L. Chen and J. Shi, *ACS Catal.*, 2018, **8**, 3688–3707.
11 H. Wang, H.-W. Lee, Y. Deng, Z. Lu, P.-C. Hsu, Y. Liu, D. Lin and Y. Cui, *Nat. Commun.*, 2015, **6**, 7261.
12 L. Han, S. Dong and E. Wang, *Adv. Mater.*, 2016, **28**, 9266–9291.
13 J. Wang, W. Cui, Q. Liu, Z. Xing, A. M. Asiri and X. Sun, *Adv. Mater.*, 2016, **28**, 215–230.
14 N. Xu, G. Cao, Z. Chen, Q. Kang, H. Dai and P. Wang, *J. Mater. Chem. A*, 2017, **5**, 12379–12384.
15 C. Lu, D. Tranca, J. Zhang, F. N. Rodríguez Hernández, Y. Su, X. Zhuang, F. Zhang, G. Seifert and X. Feng, *ACS Nano*, 2017, **11**, 3933–3942.
16 Z. Yin, Y. Sun, C. Zhu, C. Li, X. Zhang and Y. Chen, *J. Mater. Chem. A*, 2017, **5**, 13648–13658.
17 Z.-H. Xue, H. Su, Q.-Y. Yu, B. Zhang, H.-H. Wang, X.-H. Li and J.-S. Chen, *Adv. Energy Mater.*, 2017, 7, 1602355.
18 B. Weng, F. Xu, C. Wang, W. Meng, C. R. Grice and Y. Yan, *Energy Environ. Sci.*, 2017, **10**, 121–128.
19 W. Xin, W.-J. Jiang, Y. Lian, H. Li, S. Hong, S. Xu, H. Yan and J.-S. Hu, *Chem. Commun.*, 2019, **55**, 3781–3784.
20 A. Aijaz, J. Masa, C. Rösler, W. Xia, P. Weide, A. J. R. Botz, R. A. Fischer, W. Schuhmann and M. Muhler, *Angew. Chem., Int. Ed.*, 2016, **55**, 4087–4091.
21 Y. Hou, M. R. Lohe, J. Zhang, S. Liu, X. Zhuang and X. Feng, *Energy Environ. Sci.*, 2016, **9**, 478–483.
22 Y. Zhang, B. Ouyang, J. Xu, G. Jia, S. Chen, R. S. Rawat and H. J. Fan, *Angew. Chem., Int. Ed.*, 2016, **55**, 8670–8674.
23 J. Zhang, L. Qu, G. Shi, J. Liu, J. Chen and L. Dai, *Angew. Chem., Int. Ed.*, 2016, **55**, 2230–2234.
24 B. S. Yeo and A. T. Bell, *J. Am. Chem. Soc.*, 2011, **133**, 5587–5593.
25 S. Anantharaj, S. R. Ede, K. Sakthikumar, K. Karthick, S. Mishra and S. Kundu, *ACS Catal.*, 2016, **6**, 8069–8097.
26 R. Zhang, X. Wang, S. Yu, T. Wen, X. Zhu, F. Yang, X. Sun, X. Wang and W. Hu, *Adv. Mater.*, 2017, **29**, 1605502.
27 G.-L. Chai, K. Qiu, M. Qiao, M.-M. Titirici, C. Shang and Z. Guo, *Energy Environ. Sci.*, 2017, **10**, 1186–1195.
28 Z. Zhai, C. Li, L. Zhang, H.-C. Wu, L. Zhang, N. Tang, W. Wang and J. Gong, *J. Mater. Chem. A*, 2018, **6**, 9833–9838.
29 J. Tian, J. Chen, J. Liu, Q. Tian and P. Chen, *Nano Energy*, 2018, **48**, 284–291.
30 H. Sun, Y. Lian, C. Yang, L. Xiong, P. Qi, Q. Mu, X. Zhao, J. Guo, Z. Deng and Y. Peng, *Energy Environ. Sci.*, 2018, **11**, 2363–2371.
31 R. Boppella, J. Tan, W. Yang and J. Moon, *Adv. Funct. Mater.*, 2019, **29**, 1807976.
32 X. Zheng, Y. Zhang, H. Liu, D. Fu, J. Chen, J. Wang, C. Zhong, Y. Deng, X. Han and W. Hu, *Small*, 2018, **14**, 1803666.
33 H. Xu, J. Wei, M. Zhang, J. Wang, Y. Shiraishi, L. Tian and Y. Du, *Nanoscale*, 2018, **10**, 18767–18773.
34 Y. Jiao, Y. Zheng, M. Jaroniec and S. Z. Qiao, *Chem. Soc. Rev.*, 2015, **44**, 2060–2086.
35 A. J. Medford, A. Vojvodic, J. S. Hummelshøj, J. Voss, F. Abild-Pedersen, F. Studt, T. Bligaard, A. Nilsson and J. K. Nørskov, *J. Catal.*, 2015, **328**, 36–42.

# Supporting Information

**Contemporaneous Oxidation State Manipulation to Accelerate Intermediates Desorption for Overall Water Electrolysis**

Yongqiang Zhao[a], Bo Jin[a], Anthony Vasileff[a], Yan Jiao[a], Shi-Zhang Qiao*[a]

[a] School of Chemical Engineering, The University of Adelaide, Adelaide, SA 5005, Australia
E-mail: s.qiao@adelaide.edu.au

**Experimental**

**Chemicals:** Hydrochloric acid (ACS reagent, 37%) and thiourea (≥99.0%) were purchased from Sigma-Aldrich and used without further purification. Milli-Q water (18.2 M Ωcm, PURELAB Option-Q) was used in all experiments. The cobalt foil (99.95% trace metals basis, thickness 0.01 cm) was washed with dilute HCl, ultrapure water, acetone, and ethanol, and then dried under vacuum at 25 °C before use.

**Fabrication of activated cobalt oxide hydroxide (ACo):** A pre-cleaned piece of cobalt foil (1.5 cm × 0.3 cm × 0.01 cm, length × width × height) and 10 mL of 3 M HCl were sealed in a reagent bottle and then heated at 140 °C for 1 h. The cobalt foil was then taken out and washed with water to obtain ACo.

**Fabrication of cobalt nitride and sulfide (CoNS):** The CoNS electrode was fabricated by a one-step calcination of ACo with thiourea in a vacuum sealed ampoule. In a typical synthesis, a piece of ACo and thiourea were sealed in an ampoule under vacuum and then calcinated at 550 °C for 5 h. The heating rate was 5 °C min$^{-1}$ and the cooling process took place naturally. A variety of ACo to thiourea mass ratios, i.e., 1:0.05, 1:0.09, 1:0.14, 1:0.21, and 1:0.35, were employed. In the order of smallest to largest ACo : thiourea mass ratio, the as-prepared cobalt nitride and sulfide electrodes were denoted CoNS1, CoNS2, CoNS3, CoNS4, and CoNS5, respectively. In a typical synthesis, a piece of ACo (32.97 mg) is used to synthesize CoNS3. The calculated $Co_2N$ is 14.02 mg and $Co_9S_8$ is 3.71 mg. Similarly, a piece of ACo (38.32 mg) is used to synthesize CoNS2. The calculated $Co_2N$ is 5.80 mg and $Co_9S_8$ is 5.88 mg. The CoNS electrodes were washed with ethanol and water and dried under vacuum at 25 °C before use.

**Fabrication of Pt-C and Ir-C Loaded Electrodes:** 4 mg of Pt-C or Ir-C were dispersed in 1 mL of water followed by sonication for 30 min to obtain a homogeneous catalyst ink. 150 μL of the catalyst ink and 40 μL 2% Nafion solution were loaded in succession on the surface of Ni foam (surface area: 0.6 cm$^2$). The overall loading amount was 1 mg cm$^{-2}$.

**Electrochemical Characterization:** OER and HER measurements were performed on a CHI 760D Bipotentiostat (CH Instruments, Inc., USA) in $O_2$ or Ar saturated 1.0 M KOH aqueous solution using a conventional three-electrode system with a graphite rod as the counter electrode and Ag/AgCl (4 M KCl) as the reference electrode. Overall water splitting measurements were performed in a three-electrode glass cell. The current density was normalized to the geometric surface area and the measured potentials versus Ag/AgCl were converted to the reversible hydrogen electrode (RHE) scale according to the Nernst equation:

$$E_{RHE} = E_{Ag/AgCl} + 0.059 \times pH + 0.205 \qquad (1)$$

The polarization curves were recorded in the range of 1.0-1.8 V vs. RHE for the OER and -0.6 to 0 V vs. RHE for the HER at a slow scan rate of 5 mV s$^{-1}$ to minimize the capacitive current. The working electrodes were scanned several times until the signals stabilized, and then the data for polarization curves were collected and corrected for the iR contribution within the cell. The stability test was conducted using a controlled-potential electrolysis method without iR compensation. The EIS was obtained by AC impedance spectroscopy within the frequency range from 0.01 to 100 kHz in 1.0 M KOH. The equivalent circuit for fitting of the EIS data was achieved with ZView software. The Tafel slope was calculated according to Tafel equation as follows:

$$\eta = b\log( j/j_0 ) \tag{2}$$

where $\eta$ denotes the overpotential, b denotes the Tafel slope, j denotes the current density, and $j_0$ denotes the exchange current density. The onset potentials were determined based on the beginning of the linear region in the Tafel plots. The overpotential was calculated as follows:

$$\eta = E \text{ (vs RHE)} – E_r \text{ (vs RHE)} \tag{3}$$

where E denotes the actual applied potential and $E_r$ denotes the reversible potential of the reaction. $E$r is 1.23 V versus RHE for the OER and 0 V vs. RHE for the HER. HER $\eta$ is always negative. The electrochemical surface area of the electrodes was related to double layer charging curves using cyclic voltammetry in the potential range 0.606 - 0.656 V (vs. RHE) for CoNS3 and ACo, 0.611 - 0.561 V (vs. RHE) for CoNS2 and ACo. The double-layer capacitance values were determined from the slope of the capacitive current versus the scan rate.

**Physicochemical Characterization:** The scanning transmission electron microscopy (STEM) images and corresponding mapping images were obtained on a FEI Titan Themis 80-200 system. Transmission electron microscopy (TEM) images and the selected area electron diffraction (SAED) patterns were obtained on a JEOL 2100F microscope at an acceleration voltage of 200 kV. Scanning electron microscopy (SEM) images and energy dispersive spectra (EDS) were collected on a FEI Quanta 450 at high vacuum with an accelerating voltage of 20 kV. X-ray diffraction (XRD) patterns were collected on a powder X-ray diffractometer at 40 kV and 15 mA using Co-K$\alpha$ radiation (Miniflex, Rigaku). X-ray photoelectron spectra (XPS) were obtained using an Axis Ultra (Kratos Analytical, UK) XPS spectrometer equipped with an Al K$\alpha$ source (1486.6 eV).
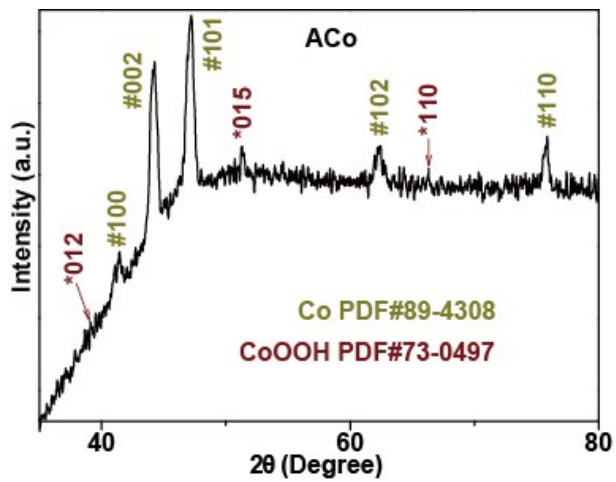
## Supplementary Results
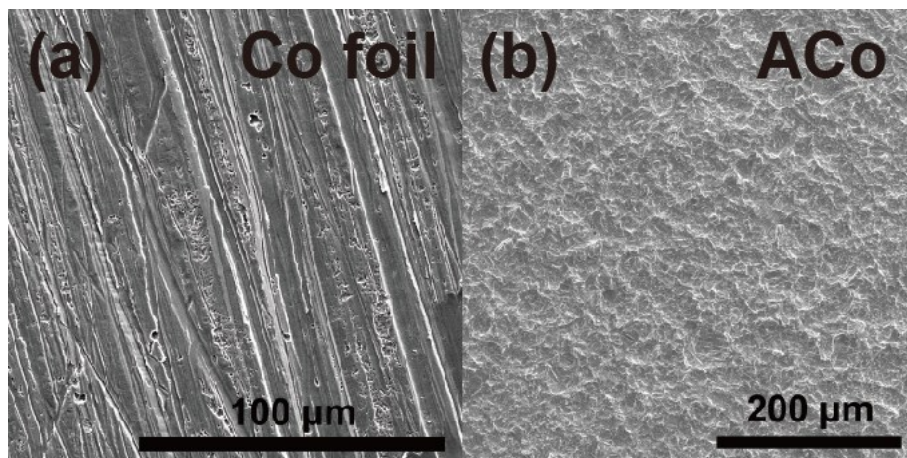


**Fig. S1** XRD pattern of ACo.



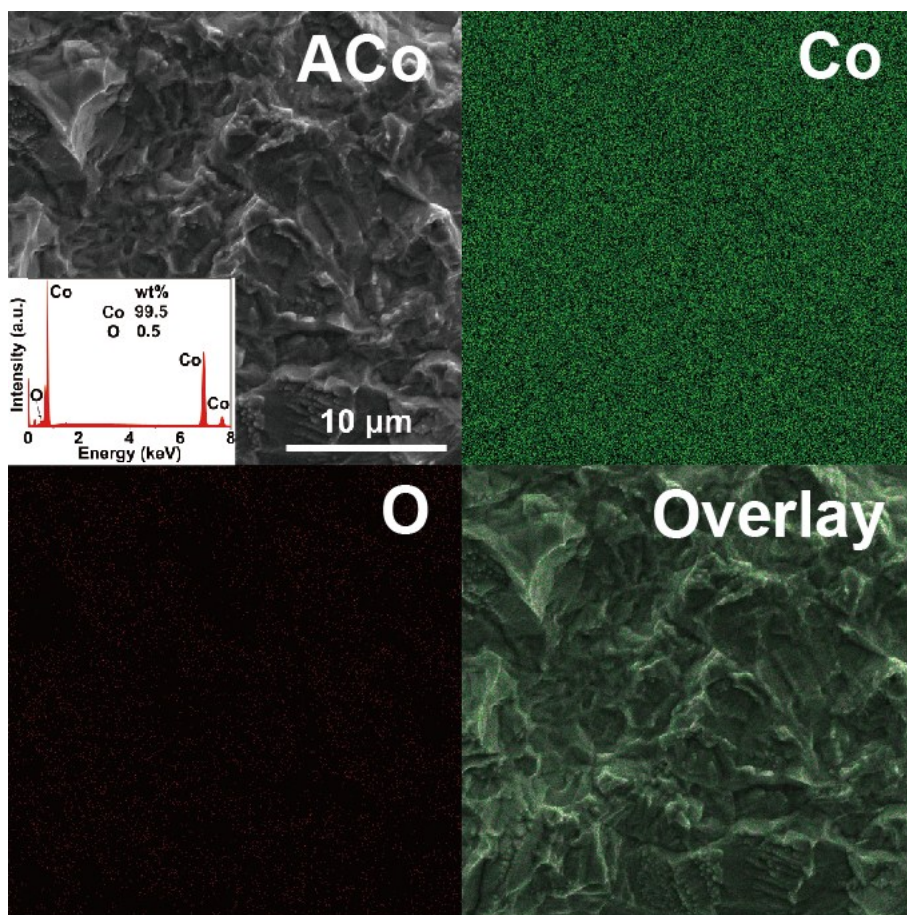**Fig. S2** SEM image of (a) cobalt foil and (b) ACo.

**Fig. S3** SEM image and (inset) EDS spectra of ACo and corresponding mapping of cobalt, oxygen and overlay.
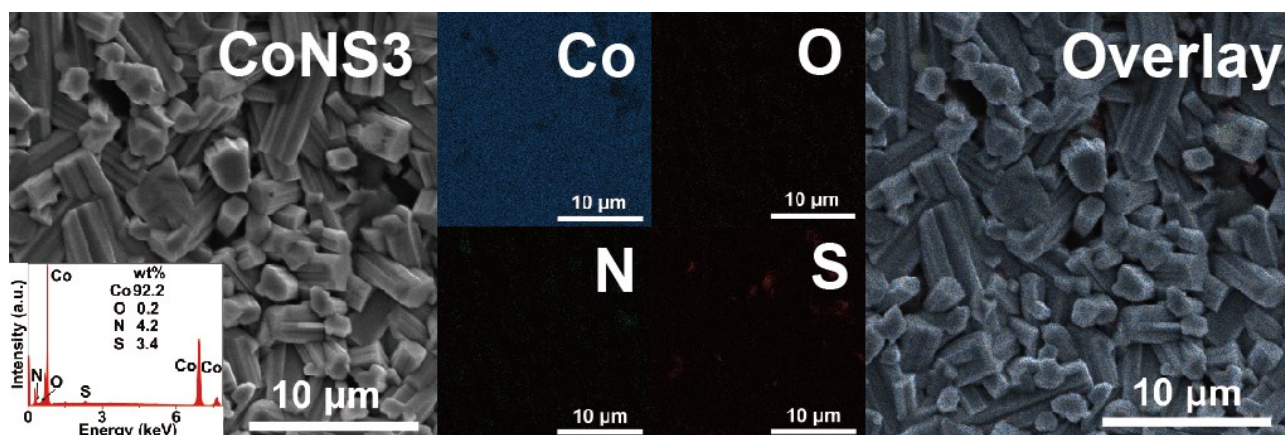


**Fig. S4** SEM image and (inset) EDS spectra of CoNS3 and corresponding mapping of cobalt, oxygen, nitrogen, sulfur, and overlay.
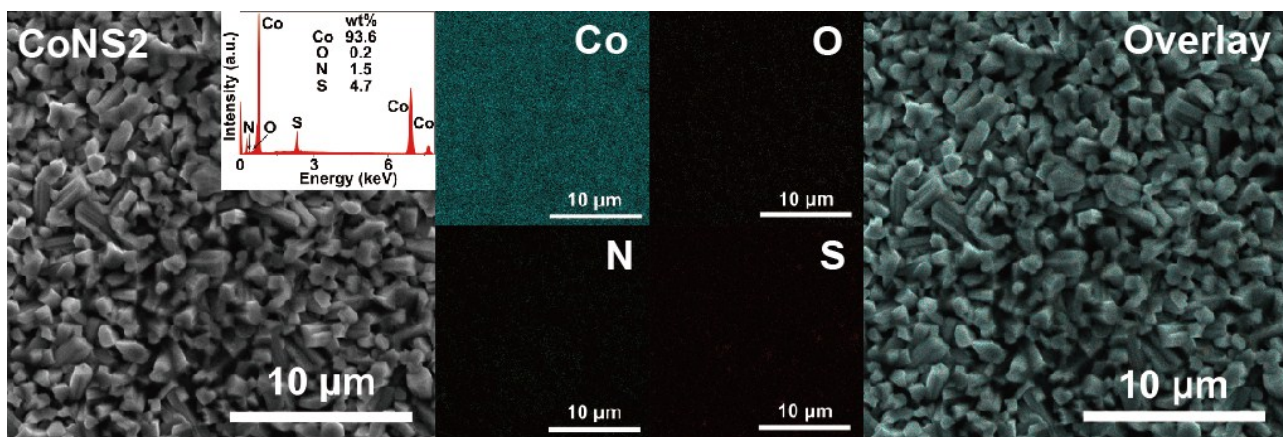
**Fig. S5** SEM image and (inset) EDS spectra of CoNS2 and corresponding mapping of cobalt, oxygen, nitrogen, sulfur, and overlay.
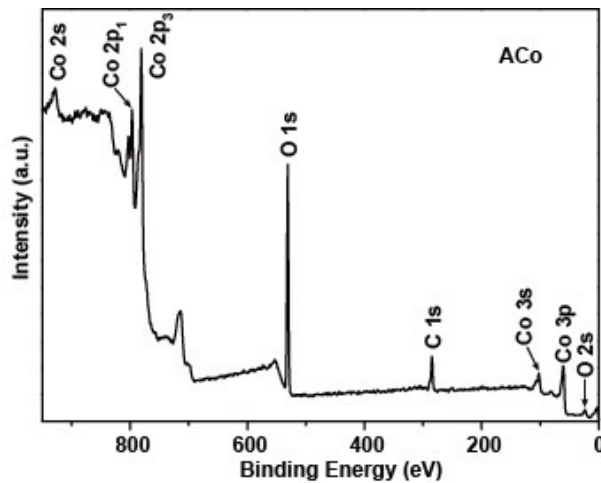


**Fig. S6** XPS survey spectrum of ACo.
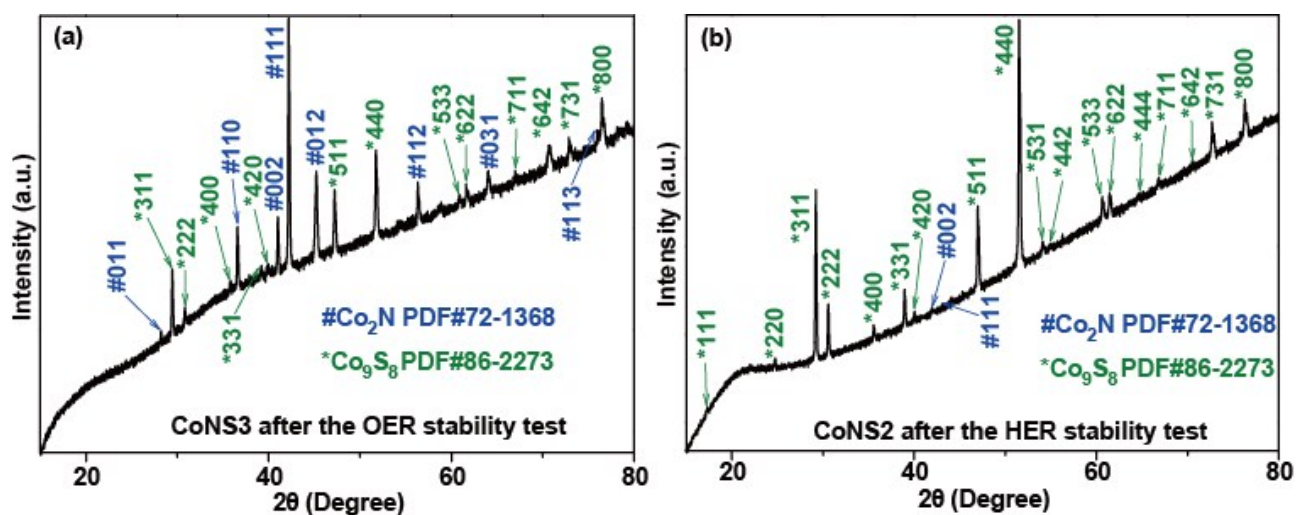
**Fig. S7** XRD patterns of (a) CoNS3 and (b) CoNS2 after cycle stability tests.
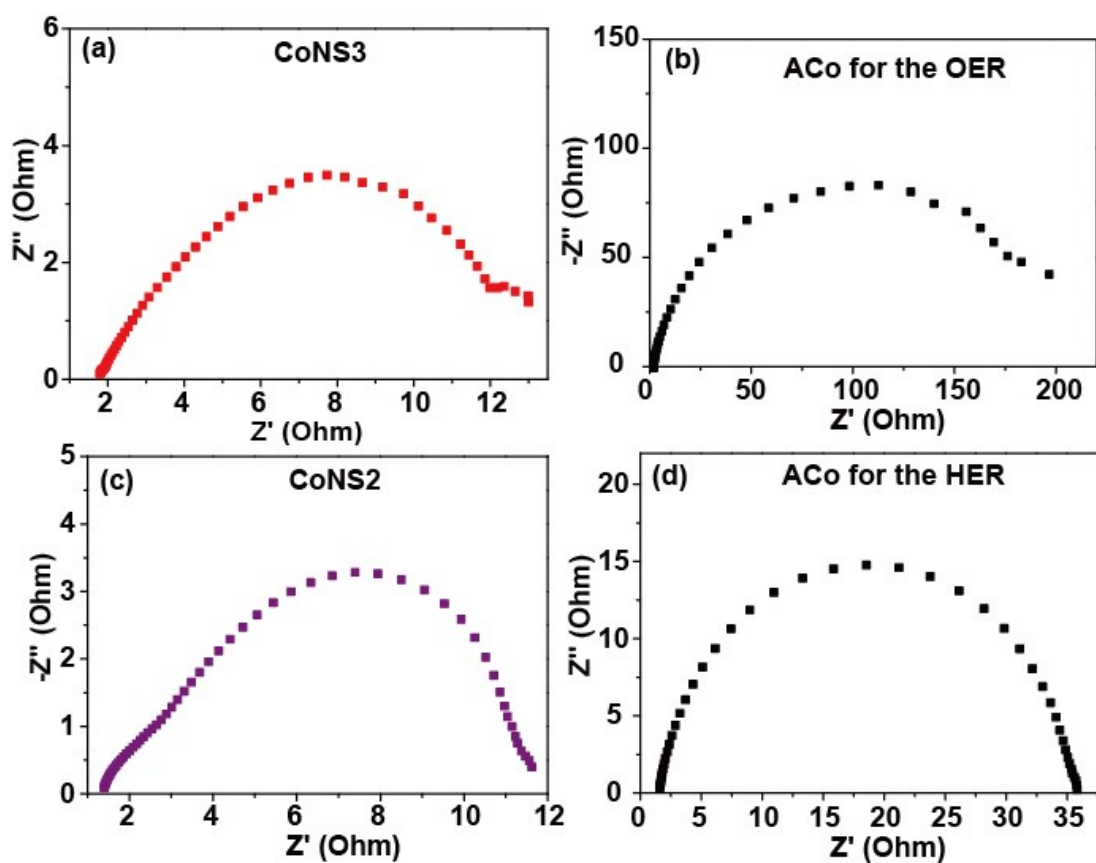


**Fig. S8** Nyquist plots of (a) CoNS3, (b) ACo for the OER process in 1.0 M KOH at a potential of 1.42 V (vs. RHE) and (c) CoNS2, (d) ACo for the HER process in 1.0 M KOH at a potential of -0.319 V (vs. RHE).

**Fig. S9** The double-layer region with scan rates ranging from 1 to 10 mV s$^{-1}$ in 1.0 M KOH for (a) CoNS3 and (c) ACo in 0.606 - 0.656 V (vs. RHE), (e) CoNS2 and (g) ACo in 0.611 - 0.561 V (vs. RHE). Charging current density with different scan rates for (b) CoNS3 and (d) ACo in 0.606 - 0.656 V (vs. RHE), (f) CoNS2 and (h) ACo in 0.611 - 0.561 V (vs. RHE).

**Table S1** OER performance comparison between CoNS3 and recently reported electrocatalysts in alkaline media

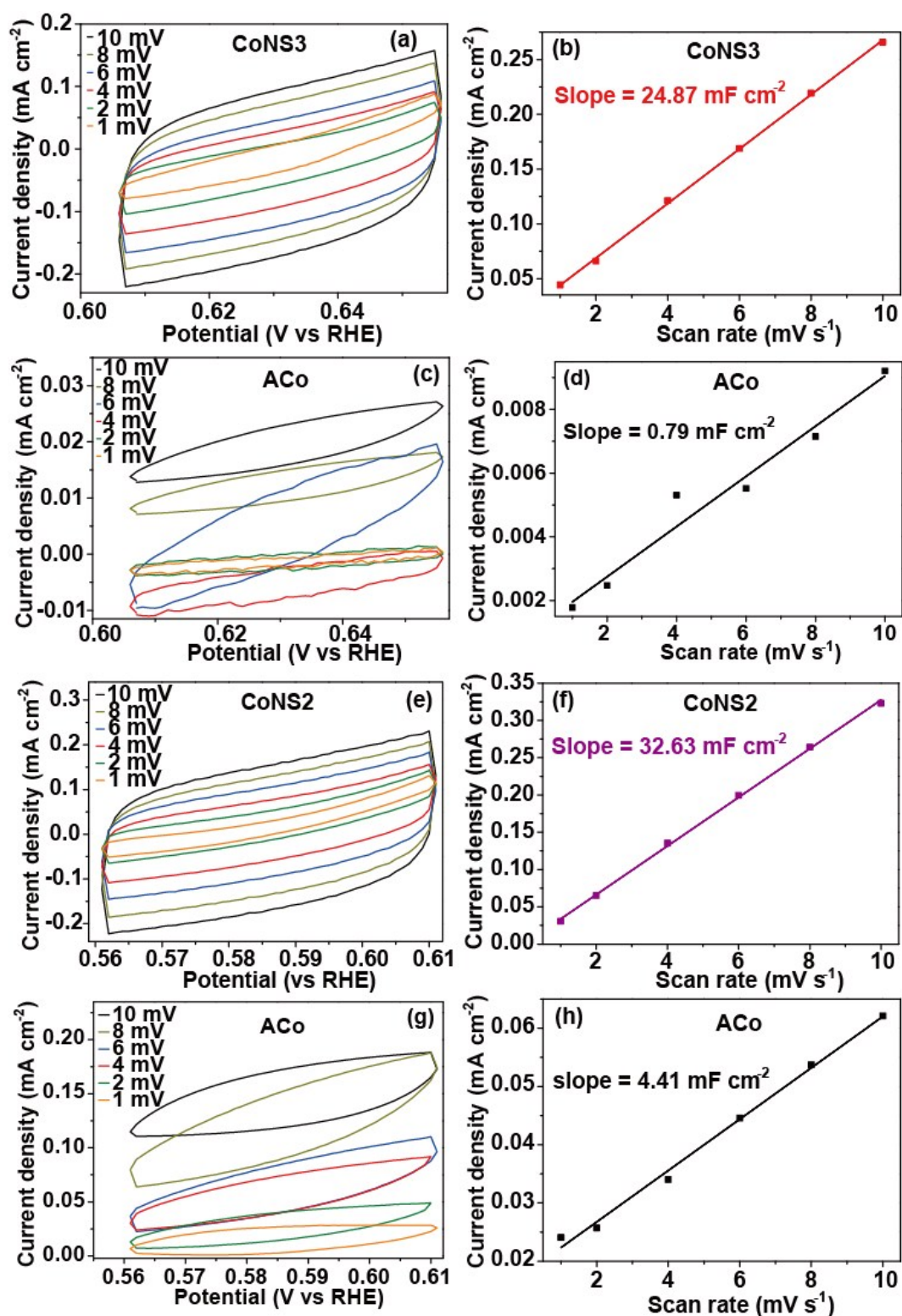| Electrocatalysts | Electrolyte | j, mA cm$^{-2}$ | η required, mV | Tafel slop, mV dec$^{-1}$ | Reference |
|---|---|---|---|---|---|
| CoNS3 | 1.0 M KOH | 100 | 275 | 109.1 | This work |
| MoS$_2$/NiS NCs | 1.0 M KOH | 100 | ~475 | 53 | S1 |
| NCP/G NSs | 1.0 M KOH | 100 | 400 | 65.9 | S2 |
| NF@Ni/C-600 | 1.0 M KOH | 100 | ~460 | 54 | S3 |
| Ni$_3$S$_2$/NF-2 | 1.0 M KOH | 100 | 425 | N/A | S4 |
| Fe$_1$-(Co$_3$O$_4$)$_{10}$ holy nanosheets | 1.0 M KOH | 100 | ~410 | 55 | S5 |
| NiCo$_2$O$_4$@CoMoO$_4$/NF-7 | 1.0 M KOH | 100 | ~510 | 102 | S6 |
| Ni-Mo$_x$C/NC-100 | 1.0 M KOH | 100 | 470 | 74 | S7 |
| NiSe-Ni$_{0.85}$Se/CP | 1.0 M KOH | 100 | 420 | 75 | S8 |
| NiMoN-NF700 | 1.0 M KOH | 100 | ~405 | 54 | S9 |
| NiCo$_2$O$_4$ nanowire arrays | 1.0 M KOH | 100 | 470 | 66.9 | S10 |

**Table S2** HER performance comparison between CoNS2 and recently reported electrocatalysts in alkaline media

| Electrocatalysts | Electrolyte | j, mA cm$^{-2}$ | η required, mV | Tafel slop, mV dec$^{-1}$ | Reference |
|---|---|---|---|---|---|
| CoNS2 | 1.0 M KOH | 100 | 335 | 141.1 | This work |
| Ni:Co$_3$S$_4$ | 1.0 M KOH | 100 | 330 | 91 | S11 |
| np-Co$_9$S$_{7.1}$P$_{0.9}$ | 1.0 M KOH | 100 | 320 | 102 | S12 |
| NFNS@NiP@Truss | 1.0 M KOH | 100 | 380 | 141 | S13 |
| Ni$_{0.75}$Co$_{0.25}$P/NC | 1.0 M KOH | 100 | 360 | 122 | S14 |
| Ni$_3$(S$_{0.25}$Se$_{0.75}$)$_2$@NiOOH | 1.0 M KOH | 100 | 400 | 87 | S15 |
| Ni$_1$Co$_1$P NWs | 1.0 M KOH | 100 | 397 | 102.1 | S16 |
| Ni$_{1-x}$Fe$_x$-LDH | 1.0 M KOH | 100 | 380 | 110 | S17 |
| NC@CoN$_x$/CF | 1.0 M KOH | 100 | 380 | 128 | S18 |
| Zn-Co-S/TM | 1.0 M KOH | 100 | 382 | 164 | S19 |
| Ni$_3$N nanosheets on carbon cloth | 1.0 M KOH | 100 | 470 | N/A | S20 |

# Reference

1.	Z. Zhai, C. Li, L. Zhang, H.-C. Wu, L. Zhang, N. Tang, W. Wang and J. Gong, *J. Mater. Chem. A*, 2018, **6**, 9833-9838.

2.	J. Tian, J. Chen, J. Liu, Q. Tian and P. Chen, *Nano Energy*, 2018, **48**, 284-291.

3.	H. Sun, Y. Lian, C. Yang, L. Xiong, P. Qi, Q. Mu, X. Zhao, J. Guo, Z. Deng and Y. Peng, *Energy. Environ. Sci.*, 2018, **11**, 2363-2371.

4.	G. Liu, Z. Sun, X. Zhang, H. Wang, G. Wang, X. Wu, H. Zhang and H. Zhao, *J. Mater. Chem. A*, 2018, **6**, 19201-19209.

5.	Y. Li, F.-M. Li, X.-Y. Meng, X.-R. Wu, S.-N. Li and Y. Chen, *Nano Energy*, 2018, **54**, 238-250.

6.	Y. Gong, Z. Yang, Y. Lin, J. Wang, H. Pan and Z. Xu, *J. Mater. Chem. A*, 2018, **6**, 16950-16958.

7.	D. Das, S. Santra and K. K. Nanda, *ACS Appl. Mater. Interfaces*, 2018, **10**, 35025-35038.

8.	Y. Chen, Z. Ren, H. Fu, X. Zhang, G. Tian and H. Fu, *Small*, 2018, **14**, 1800763.

9.	B. Chang, J. Yang, Y. Shao, L. Zhang, W. Fan, B. Huang, Y. Wu and X. Hao, *ChemSusChem*, 2018, **11**, 3198-3207.

10.	A. Sivanantham, P. Ganesan and S. Shanmugam, *Adv. Funct. Mater.*, 2016, **26**, 4661-4672.

11.	S. Tang, X. Wang, Y. Zhang, M. Courté, H. J. Fan and D. Fichou, *Nanoscale*, 2019, **11**, 2202-2210.

12.	Y. Tan, M. Luo, P. Liu, C. Cheng, J. Han, K. Watanabe and M. Chen, *ACS Appl. Mater. Interfaces*, 2019, **11**, 3880-3888.

13.	X. Su, X. Li, C. Y. A. Ong, T. S. Herng, Y. Wang, E. Peng and J. Ding, *Advanced Science*, 2019, **6**, 1801670.

14.	R. Boppella, J. Tan, W. Yang and J. Moon, *Adv. Funct. Mater.*, 2019, **29**, 1807976.

15.	X. Zheng, Y. Zhang, H. Liu, D. Fu, J. Chen, J. Wang, C. Zhong, Y. Deng, X. Han and W. Hu, *Small*, 2018, **14**, 1803666.

16.	H. Xu, J. Wei, M. Zhang, J. Wang, Y. Shiraishi, L. Tian and Y. Du, *Nanoscale*, 2018, **10**, 18767-18773.

17.	G. Rajeshkhanna, T. I. Singh, N. H. Kim and J. H. Lee, *ACS Appl. Mater. Interfaces*, 2018, **10**, 42453-42468.

18.     J. Zheng, X. Chen, X. Zhong, S. Li, T. Liu, G. Zhuang, X. Li, S. Deng, D. Mei and J.-G. Wang, *Adv. Funct. Mater.*, 2017, **27**, 1704169.

19.     Y. Liang, Q. Liu, Y. Luo, X. Sun, Y. He and A. M. Asiri, *Electrochim. Acta*, 2016, **190**, 360-364.

20.     D. Gao, J. Zhang, T. Wang, W. Xiao, K. Tao, D. Xue and J. Ding, *J. Mater. Chem. A*, 2016, **4**, 17363-17369.

# Chapter 7 Conclusions and Perspectives

## 7.1 Conclusions

This thesis aims to develop a simple strategy, i.e. the ampoule method, for the controllable synthesis of highly-efficient and low-cost bifunctional electrocatalysts and investigate the electrocatalytic mechanism. Based on the research in this thesis, the following conclusions can be drawn:

- A simple and scalable method for fabricating new three dimensional (3D) cobalt selenide electrodes with novel $CoSe$ and $Co_9Se_8$ phases has been developed. The charge state of Co species and electrocatalytic performance of the prepared cobalt selenide catalysts are manipulated by controlling the mass ratio of raw materials and calcining in a vacuum-sealed ampoule at high temperature. The resultant 3D network, exposed electrocatalytic centers, and rapid charge transfer capability of these novel electrodes are responsible for their high activity and stability towards the oxygen evolution reaction (OER) and hydrogen evolution reaction (HER). These merits result in excellent overall seawater splitting performance.

- A simple method has been developed to fabricate bifunctional interfacial nickel nitride/sulfide electrodes with abundant interfacial contact between $Ni_3N$ and $Ni_3S_2$ species. The obvious interface between various planes of $Ni_3N$ and $Ni_3S_2$ species is confirmed by high resolution transmission electron microscopy. Acting as the electrocatalytic active sites, these ubiquitous interfaces are beneficial for dissociative adsorption of water molecules and consequent water electrolysis. This structural feature results in excellent overall water splitting performance under neutral pH conditions and in seawater. The electrocatalytic mechanism is explored through the study of electrochemical active sites, which suggests that the abundant interfacial regions are predominantly responsible for the excellent catalytic performance.

- The ampoule method has been applied to develop non-metal single-atom catalysts, i.e. single atom nickel iodide (SANi-I), which is utilized as a highly efficient electrocatalyst for the HER. Atomically dispersed iodine and the structure of

SANi-I are confirmed by aberration-corrected high-angle annular dark-field scanning transmission electron microscopy and synchrotron-based X-ray absorption spectroscopy. The resultant SANi-I possesses superior structural stability and exhibits extraordinary electrocatalytic HER activity. The electrocatalytic mechanism is explored by *in-situ* Raman spectroscopy which suggests that the single iodine atoms and adjacent nickel can accelerate the dissociative adsorption of water via the formation of the I-H$_{ads}$ (adsorbed hydrogen) intermediate. This work provides new opportunities for the development of single-atom catalysts for advanced energy conversion.

- The contemporaneous manipulation of the oxidation states of Co, N and S has been realized via the simple synthesis of cobalt nitride and sulfide (CoNS). Here, cobalt foil is activated by hydrochloric acid to prepare activated cobalt (ACo) and afterwards ACo is sealed with thiourea in an evacuated ampoule to synthesize CoNS. The oxidation state analysis via X-ray photoelectron spectroscopy reveals that low Co oxidation state favors the OER while high N and S oxidation states promote the HER, indicating that the water splitting process for this electrocatalyst is kinetically governed by intermediates desorption. A 100 mA cm$^{-2}$ OER current density is achieved for CoNS at an overpotential of 275 mV, lower than that for the Ir/C benchmark (374 mV) in 1.0 M KOH. A 4.5 mA cm$^{-2}$ current density at a voltage of 1.8 V is achieved for CoNS when utilized for overall electrolysis in neutral buffer solution. This performance is better than that for the noble-metal based system at the same voltage (3.4 mA cm$^{-2}$).

In summary, the ampoule method has been implemented to controllably synthesize highly-efficient and low-cost bifunctional electrocatalysts with abundant electrochemically active sites and improved electrocatalytic performance. The perceptive comprehension of the electrocatalytic mechanism can provide new insight for developing advanced bifunctional electrocatalysts for water electrolysis.

## 7.2 Perspectives

Although substantial achievement has been realized regarding the development of

bifunctional electrocatalysts and the understanding of their electrocatalytic mechanism, additional endeavors are still required to accelerate the ampoule method for energy conversion reactions.

- The ampoule method demonstrates great potential for fabricating miscellaneous materials that have been applied in a wide range of applications. In this aspect, electrocatalysts, including copper-based materials for the carbon dioxide reduction reaction, bismuth-based materials for the nitrogen reduction reaction, and transition metal-based materials for the oxygen reduction reaction and hydrogen oxidation reaction can be designed and developed via the ampoule method. Expanding the range of electrocatalyst choice for energy conversion reactions will improve device efficiency and decrease the operational costs.

- A clear understanding of the material growth mechanisms using *operando* techniques will enable conscious tailoring of the components, morphologies, and structures of targeted electrocatalysts, aiming to improve electrocatalytic performance. *In-situ* characterizations, such as *in-situ* X-ray absorption spectroscopy, X-ray diffraction, X-ray photoelectron spectroscopy, infrared spectroscopy, Raman spectroscopy, and transmission electron microscopy are anticipated to facilitate future studies into the growth mechanisms of electrocatalyst materials and guide electrocatalyst design.

- Comprehension of the electrocatalytic mechanism at the atomic and molecular level is a crucial factor. However, the ambiguous electrocatalytic mechanism severely limits the development and practical application of water electrolysis devices. *In-situ* characterizations, such as *in-situ* X-ray absorption spectroscopy, X-ray photoelectron spectroscopy, infrared spectroscopy and Raman spectroscopy will deliver new ways to ascertain proposed reaction mechanisms.

It is believed that increasing the number of breakthroughs in water electrolysis can be achieved through diversified electrocatalysts and *in-situ* characterization studies.

# Appendix Publications during PhD Candidature

[1] **Y. Zhao**, B. Jin, Y. Zheng, H.Y. Jin, Y. Jiao, **S.-Z. Qiao**,* Charge State Manipulation of Cobalt Selenide for Overall Seawater Electrolysis, *Advanced Energy Materials* 2018, 8, 1801926.

[2] **Y. Zhao**,[+] T. Ling,[+] S. Chen,[+] B. Jin, A. Vasileff, Y. Jiao, L. Song, J. Luo and **S.-Z. Qiao**,* Non-metal Single Iodine Atom Electrocatalysts for the Hydrogen Evolution Reaction, *Angewandte Chemie International Edition* 2019, 58, 2. (+**Equal contribution**)

[3] **Y. Zhao**, B. Jin, A. Vasileff, Y. Jiao, **S.-Z. Qiao,*** Interfacial Nickel Nitride/Sulfide as a Bifunctional Electrode for Highly Efficient Overall Water/Seawater Electrolysis, *Journal of Materials Chemistry A* 2019, 7, 8117.

[4] **Y. Zhao**, B. Jin, A. Vasileff, Y. Jiao and **S.-Z. Qiao,*** Contemporaneous Oxidation State Manipulation to Accelerate Intermediates Desorption for Overall Water Electrolysis, *Chemical Communications* 2019, 55, 8313.

[5] **Y. Zhao**, B. Jin, A. Vasileff, B. Shi, Y. Jiao and **S.-Z. Qiao,*** The Ampoule Method: A Pathway towards Controllable Synthesis of Electrocatalysts for Water Electrolysis, *Chemistry - A European Journal* 2019, submitted.

[6] H.Y. Jin, X. Liu, A. Vasileff, Y. Jiao, **Y. Zhao**, Y. Zheng and **S.-Z. Qiao,*** Single-crystal Nitrogen-rich 2D $Mo_5N_6$ Nanosheets for Efficient and Stable Seawater Splitting, *ACS Nano* 2018, 12, 12761.

[7] D.D. Zhu, J.L. Liu, **Y. Zhao**, Y. Zheng and **S.-Z. Qiao,*** Engineering 2D Metal-Organic Frameworks/$MoS_2$ Interface for Enhanced Alkaline Hydrogen Evolution, *Small* 2019, 15, 1805511.